A UNITED STATES DEPARTMENT OF COMMERCE PUBLICATION

NOAA Technical Memorandum ERL WMPO-8

U.S. DEPARTMENT OF COMMERCE
NATIONAL OCEANIC AND ATMOSPHERIC ADMINISTRATION
Environmental Research Laboratories

The Global Energy Budget and the Role of Cumulus Clouds

JOANNE SIMPSON

Weather Modification Program Office
BOULDER, COLORADO
November 1973

ENVIRONMENTAL RESEARCH LABORATORIES

WEATHER MODIFICATION PROGRAM OFFICE

NATIONAL OCEANIC AND ATMOSPHERIC ADMINISTRATION

U.S. DEPARTMENT OF COMMERCE
National Oceanic and Atmospheric Administration
Environmental Research Laboratories

NOAA Technical Memorandum ERL WMPO-8

THE GLOBAL ENERGY BUDGET AND THE ROLE OF CUMULUS CLOUDS

Joanne Simpson

Experimental Meteorology Laboratory

Based on a series of five lectures
given at a NATO Advanced Study Conference
on the Air-Sea Boundary Layer

Ramsey, Isle of Man

September 21 - October 2, 1970

Weather Modification Program Office
Boulder, Colorado
November 1973

TABLE OF CONTENTS

PREFACE

This material has been prepared in hopes that it may be used as a text and/or reference material by graduate students and researchers interested in acquiring a broad background in tropical boundary layers. Particular emphasis is placed upon tropical cumulus convection and the role it plays in boundary-layer processes and global energy budgets.

Since the work was originally in the form of a series of five lectures, the presentation is informal, incompletely documented and liberally illustrated by photographs and diagrams.

THE GLOBAL ENERGY BUDGET AND THE ROLE OF CUMULUS CLOUDS

Joanne Simpson

1. THE GLOBAL ENERGY BUDGETS

The choice of the word "budget" rather than "balance" is to imply a highly dynamic rather than static situation, and "budgets-plural", rather than "budget-singular" because we will deal with the heat and moisture budgets together. It is soon evident that the moisture or latent heat energy transactions are of dominant importance on this planet. We shall see almost at once that the condensation, evaporation and precipitation terms are among the largest terms in the energy budget equations. Kinetic energy transactions, on the other hand, are very much smaller in magnitude, at most only a few percent of the heat energy transactions, meaning that the atmospheric heat engine is very inefficient. The kinetic energy terms are within the margin of error with which we can determine the major terms in the heat energy budgets, so therefore we must consider the kinetic budget separately from the heat budget, which we will not have time to do in this report.

At the very outset, we must emphasize the close interconnection between circulations and energy budgets. Air and ocean circulations are constrained to operate in such a way as to achieve an energy balance in the long run. Conversely, energy releases and exchanges are affected,

often controlled, by the motions in sea and air. Even the receipt and absorption of incoming radiation from the sun is affected by circulations through the mechanisms of clouds, which are produced and arranged by the air motions themselves.

Therefore the first three figures review schematically the large-scale circulation systems we encounter in ocean and atmosphere.

Figure 1 shows schematic ocean surface circulation patterns and figure 2 illustrates meridional atmospheric circulation (after Palmén and Newton). Figure 3 is of the zonal atmospheric circulation (after Palmén and Newton).

The motions shown in these diagrams should be kept in mind as much as possible through the following development.

We are now going to approach the energy budgets in two parts, putting the parts together to examine the whole picture sometime in the next sections. We will first consider the heat energy balance at the sea surface and see what terms go into it, how we evaluate them and what we can learn from them. Secondly, we will do the same for the ocean-atmosphere system.

Let us consider the heat energy budget of a deep ocean column of unit area in order to discuss the transfers through its surface. Of the total impinging solar radiation, some is reflected by albedo α and some is reradiated back to space in long wave lengths. The net amount absorbed,

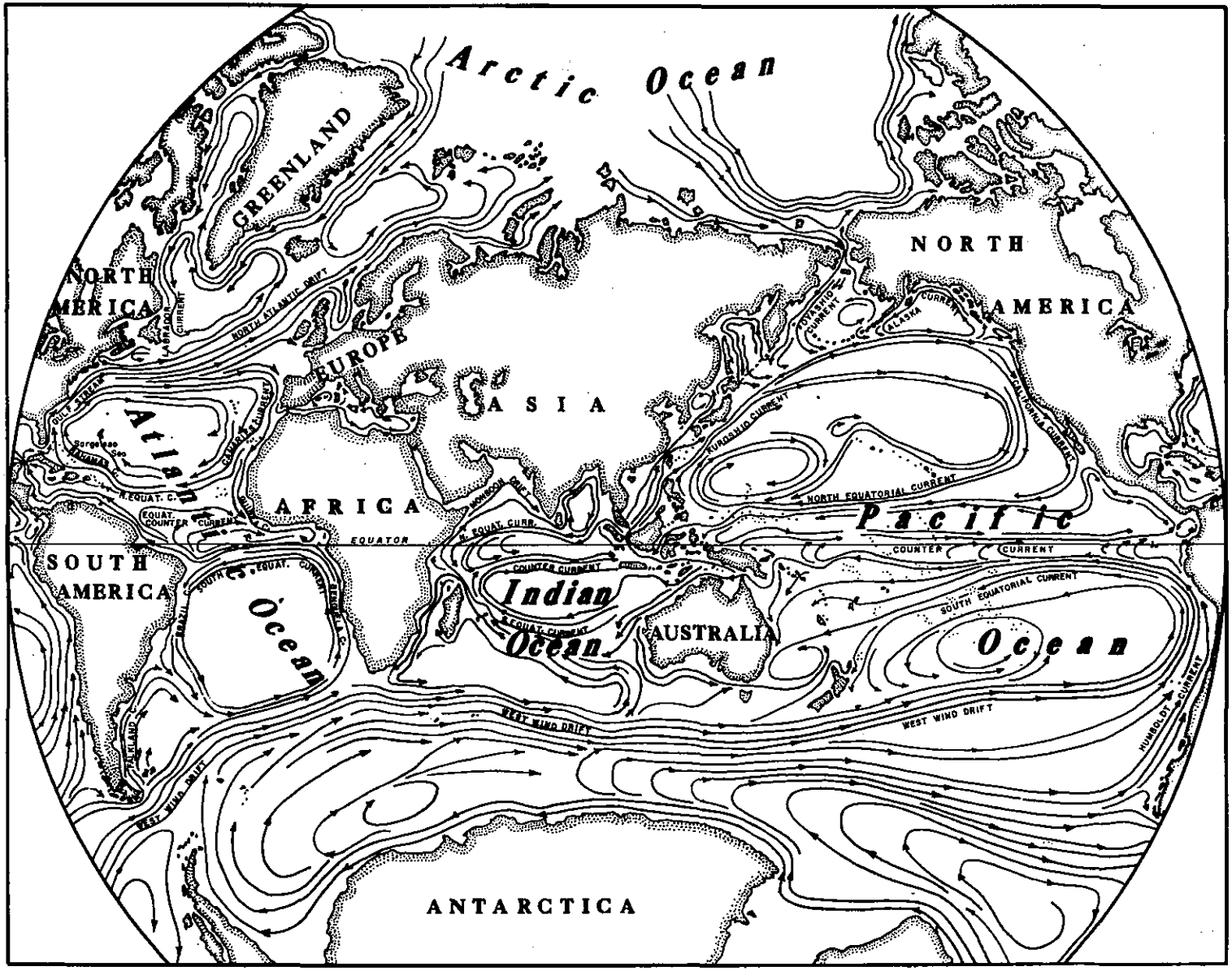

Figure 1. Schematic illustration of the surface patterns of the oceans.

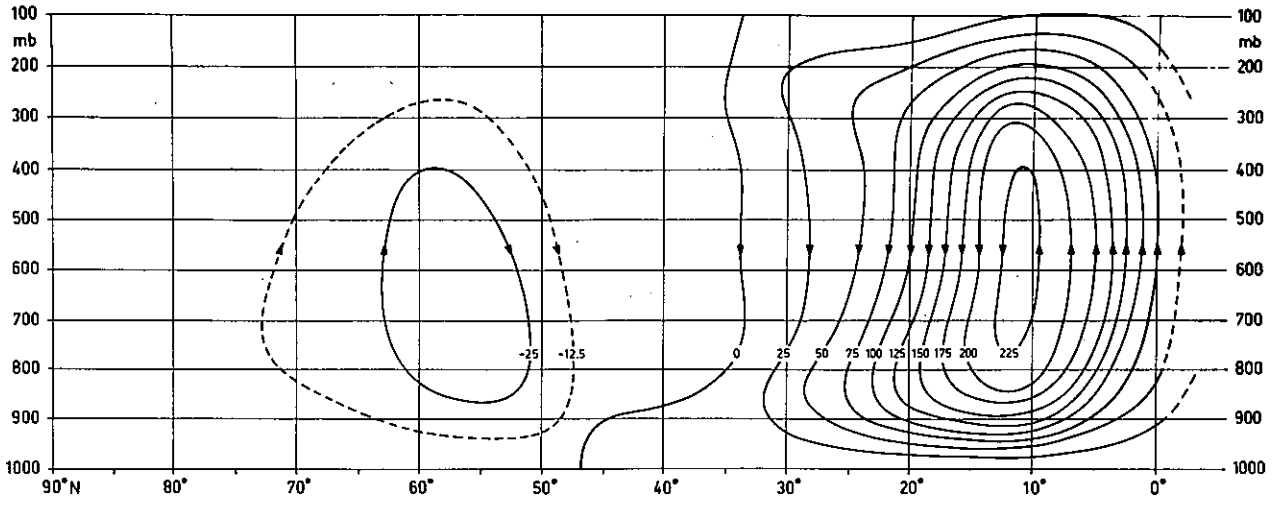

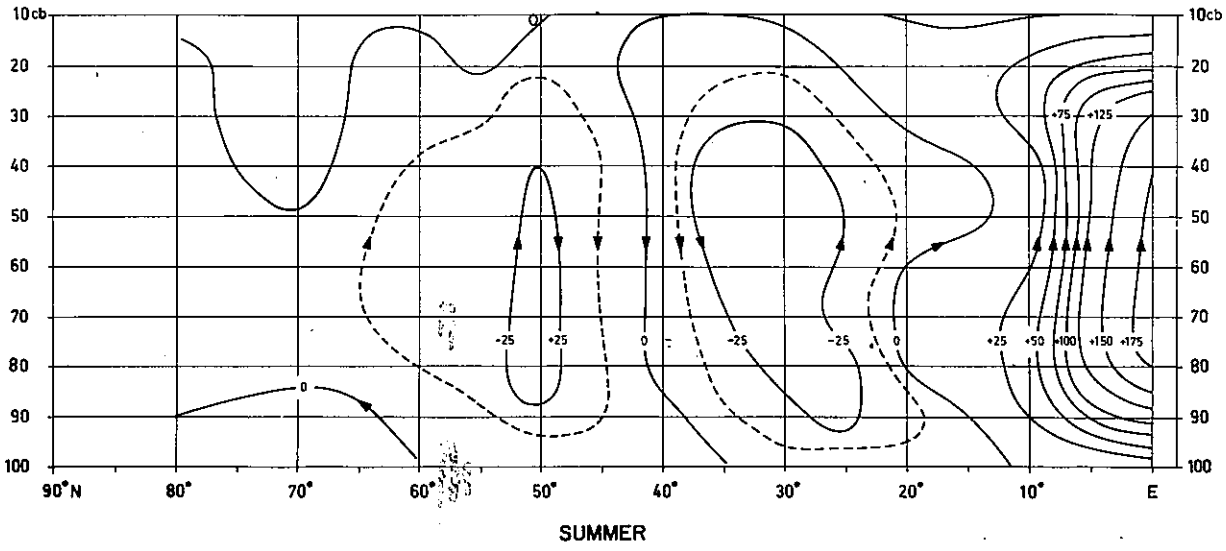

Figure 2. The total mean meridional circulation in the northern hemisphere during the winter and summer seasons. The transport capacity of each streamline channel is 25 x 10^6 ton/sec in the direction indicated by the arrows. (After Palmen and Newton).

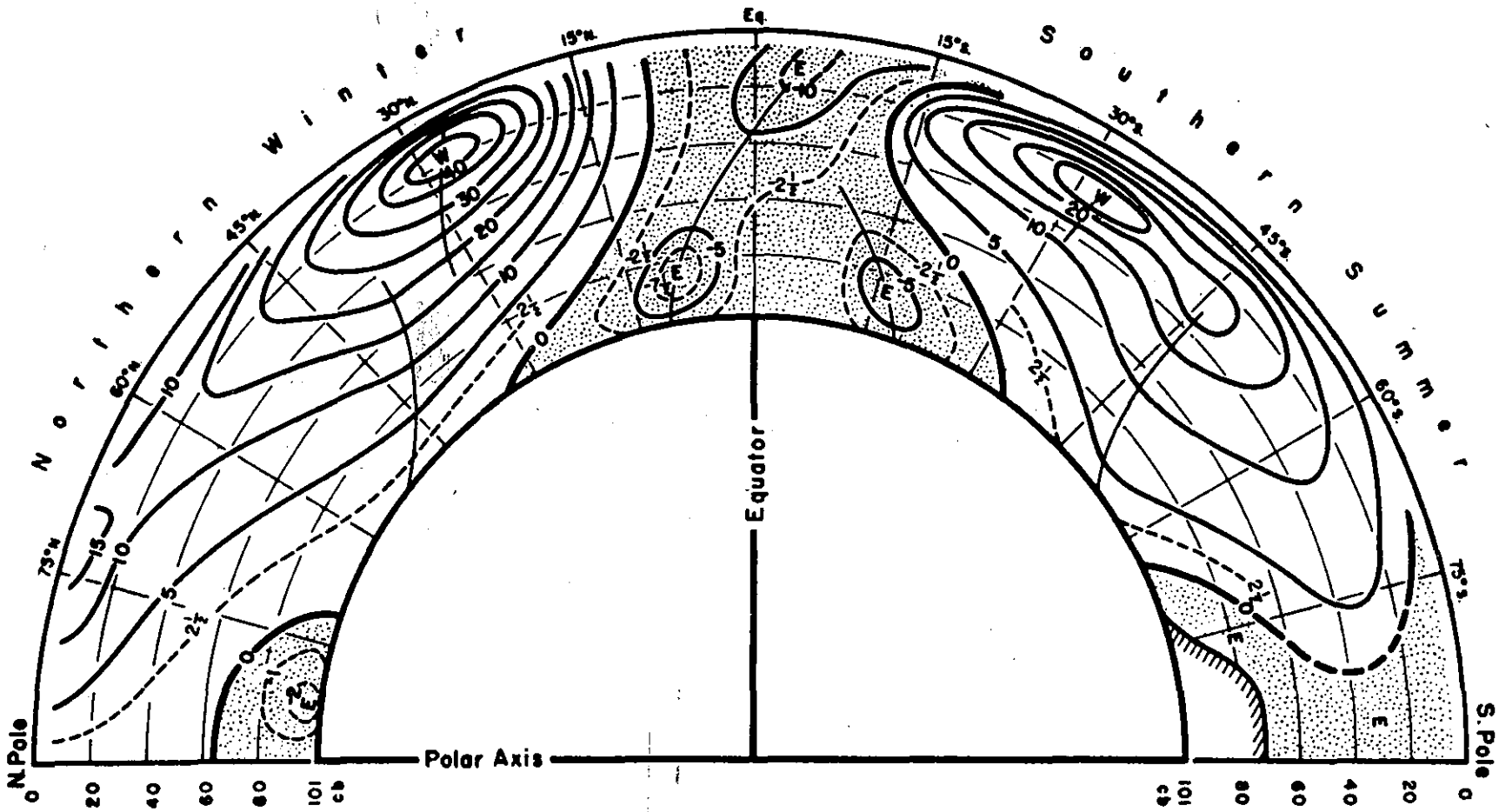

Figure 3. Mean zonal wind (m/sec) averaged over all longitudes in northern winter and southern summer. Negative values denote mean easterly wind. (After Palmen & Newton.)

called the "radiation balance" of the surface, is used in three ways: it may raise the temperature of the ocean column, be carried away by sea transports, or be supplied to the atmosphere in latent and/or sensible form. The law of energy conservation is used to express this heat balance quantitatively as follows:

$$R = Q_s + Q_e + S + Q_{vo} \qquad (1)$$

where the units of each term are heat energy per unit area per unit time, often calories per cm^2 per sec or langleys per sec. Q_s plus Q_e is the heat energy supplied by the sea to the atmosphere in sensible, Q_s, plus latent Q_e form. The latter may be written as LE, where L is the latent heat of vaporization in cal gm^{-1} and E is actual evaporation in gm/cm^2 or in cm of water per cm^2; the ocean recognizes the sum of Q_s and Q_e as a sensible heat loss. S is the storage of heat in the ocean, positive for increased heat content of the column. It is assumed zero in the climatological calculations of mean budgets. Values required in long term climatic trends are so small as to be in the margin of error of all terms. Calculation of oceanic heat storage from oceanographic measurements shows that it can exceed 1/3 Q_e at the times of maximum heating and cooling. Shorter term than seasonal storage fluctuations are generally unknown and pose great difficulty in smaller-scale budget analyses. Q_{vo} is the flux divergence of oceanic heat transports; these may be due to the major horizontal wind-driven currents, to thermohaline circulations in a vertical plane or even lateral eddy fluxes may

require inclusion. The oceanographic measurements for measuring lateral heat fluxes and flux divergences at regular intervals on a global scale are virtually non-existent and hence this term in the equation is often either ignored or computed as a residual after the other terms are evaluated. As for ignoring it, calculations suggest that in the Caribbean area it rarely exceeds ten percent of Q_e. We shall see shortly that most of what we know about heat transports by ocean currents comes from evaluating Q_{vo} as a residual in this equation and then integrating the result!

There are some small terms omitted from this equation: These are 1) heat sources due to dissipation of kinetic energy of air and ocean, which may amount to one percent of the dominant terms, of three langleys/day, and 2) that due to radioactive decay in the earth's interior, transmitted through the ocean bottom, which is estimated as not above 0.1 percent or 0.3 langleys per day. These numbers are well within the accuracy of presently possible evaluations of the larger terms and negligible for annual and seasonal budget studies. For long periods and for consideration of climatic change they may not be negligible.

We see that (1) can be solved for $Q_s + Q_e$, namely

$$Q_s + Q_e = R - S - Q_{vo}$$

and in fact this was one of the two approaches used by Woodrow Jacobs in his classical evaluations of sea-air transfer which began in the early 1940s and followed by numerous others, including the Russians under Budyko.

The other common method of evaluating Q_s and Q_e involves the use of the bulk aerodynamic equations, usually called the Jacobs transfer formulas, which are as follows:

$$Q_s = B_s C_p (T_o - T_a) u_a \tag{2}$$

$$Q_e = LE = B_e L (q_o - q_a) ua \tag{3}$$

These equations can be derived from turbulent boundary layer theory or they can be regarded as useful empirical relations. Their derivations and range of validity has been discussed elsewhere. The subscript o refers to the surface and a to "anemometer level" (usually about 6 m) where the wind-speed u is measured. T_o is the temperature of the sea surface and q_o is the saturation mixing ratio at the temperature of the sea surface.

The ratio r between Q_s and Q_e is

$$r = \frac{Q_s}{Q_e} = \frac{C_p}{L} \quad \frac{(T_o - T_a)}{(q_o - qa)} \tag{4}$$

$$Q_s = r\, Q_e$$

We assume $B_e \cong B_s$, which can be justified. The ratio r is called the "Bowen ratio" and is found to be 0.1 or less equatorward of the subtropical ridge lines.

In his classical work in calculating world-wide annual average values of Q_s and Q_e Jacobs[11, 12] picked parts of the oceans where Q_{vo} should be small and found Q_e and E:

$$Q_e = LE = \frac{R}{1 + r} \qquad \underline{\text{Energy budget method}} \qquad \underline{\text{Determination of fluxes}} \qquad (5)$$

Thus he checked or evaluated the coefficient B_e in the transfer formulas, which he then applied everywhere to construct maps of mean annual Q_e and Q_s (which we will look at later). The best acceptable values of these quantities today differ little from those he found 25 years ago. The crux of these evaluations lies in the determination of R, the sea surface radiation balance. A 20-30 percent error in R can cause one to get even the wrong sign for any one of the 3 smaller terms (Q_s, S, Q_{vo}) on the right, if it is being determined as a residual.

We may write:

$$R = (Q + q)\ (1 - \alpha) - Q_b \qquad (6)$$

This is a form of the energy conservation law. Q is the sum of direct short-wave radiation, q is the sum of diffuse short-wave radiation, α is the albedo of the sea surface and Q_b is the back or "effective outgoing" radiation, which is determined by the difference between "greenhouse" radiation of the atmosphere and outgoing radiation from the surface.

The critical variable entering R from the meteorological-oceanographic standpoint is atmospheric cloudiness which affects both $Q + q$ and Q_b. Here, in fact, is where the space and time-wise resolution of energy budget determinations breakdown. It is not much problem to compute the <u>cloudless</u> values of $Q + q + Q_b$. Methods for these have been evolved by London, Budyko and others. The important departure from these tabulations,

causing the actual surface radiation balance to be altered by the effects of circulations, lies first in the rather strong reduction of $Q + q$ by clouds and secondly in the much weaker reduction of Q_b thereby. In the old days it was asserted that, to first order, satisfactory corrections for cloudiness to cloudless tabulations could be obtained from knowledge of the average fractional cloudiness alone, ignoring types, heights and the exact nature and distribution of the clouds. These correction formulas are based on the assumption that cloud albedo and absorption, etc. is constant and independent of thickness. Formulas like the following were used in the classical heat budget studies:

$$(Q + q) = (Q + q)_o \quad [1 - an^b] \tag{7}$$

and

$$Q_b = Q_{bo} \quad [1 - cn^d] \tag{8}$$

where n is mean fractional cloudiness in tenths and a, b, c, d are empirical constants. Empirically $b \approx d \approx 1$, so there is hypothesized roughly a linear decrease of sea surface radiation balance R with mean cloudiness n, namely

$$R = A - Bn \tag{9}$$

for a given latitude and season. Such a relationship might provide a first start at modeling the interaction between energy input and circulation dynamics, particularly in the tropics where mean cloudiness appears to be roughly proportional to synoptic-scale convergence. So far as I know, none of the modelers have tried out such a feedback between heat source and

circulation in the models. The next two figures illustrate the effects of clouds on radiation.

Figure 4 is for latitude 20°, in February. The graph illustrates the approximately linear decrease of radiation balance R with mean fractional cloudiness, n. The constants in (7) and (8) were taken from Budyko's tables [3]. These empirical constants which vary with latitude and month, thus implicitly taking into account the differences in prevailing cloud types and thicknesses. We can see from the magnitudes on this diagram that a 20 percent error in Q + q (from a presumed error in how we take cloudiness into account) would lead to about a 1/3 error in R. Computing Q_e from R and (5), that is, ignoring S and Q_{vo} and assuming $r = \frac{Q_s}{Q_e} = 0.1$,

n	Q_e
0	11.1 kg cal/cm^2 per month
40%	7.5
100%	3.3

The diminution in evaporation is more than a factor of two as the skies go from clear to overcast.

Now in the next figure, let us look at results of actual measurements from a weather ship of incoming radiation as a function of sky condition, coded in ascending number from one to nine.

Figure 5 is from a fine radiation measurement study by Lumb [15]. How does this reconcile, if at all, with the previous figure? It

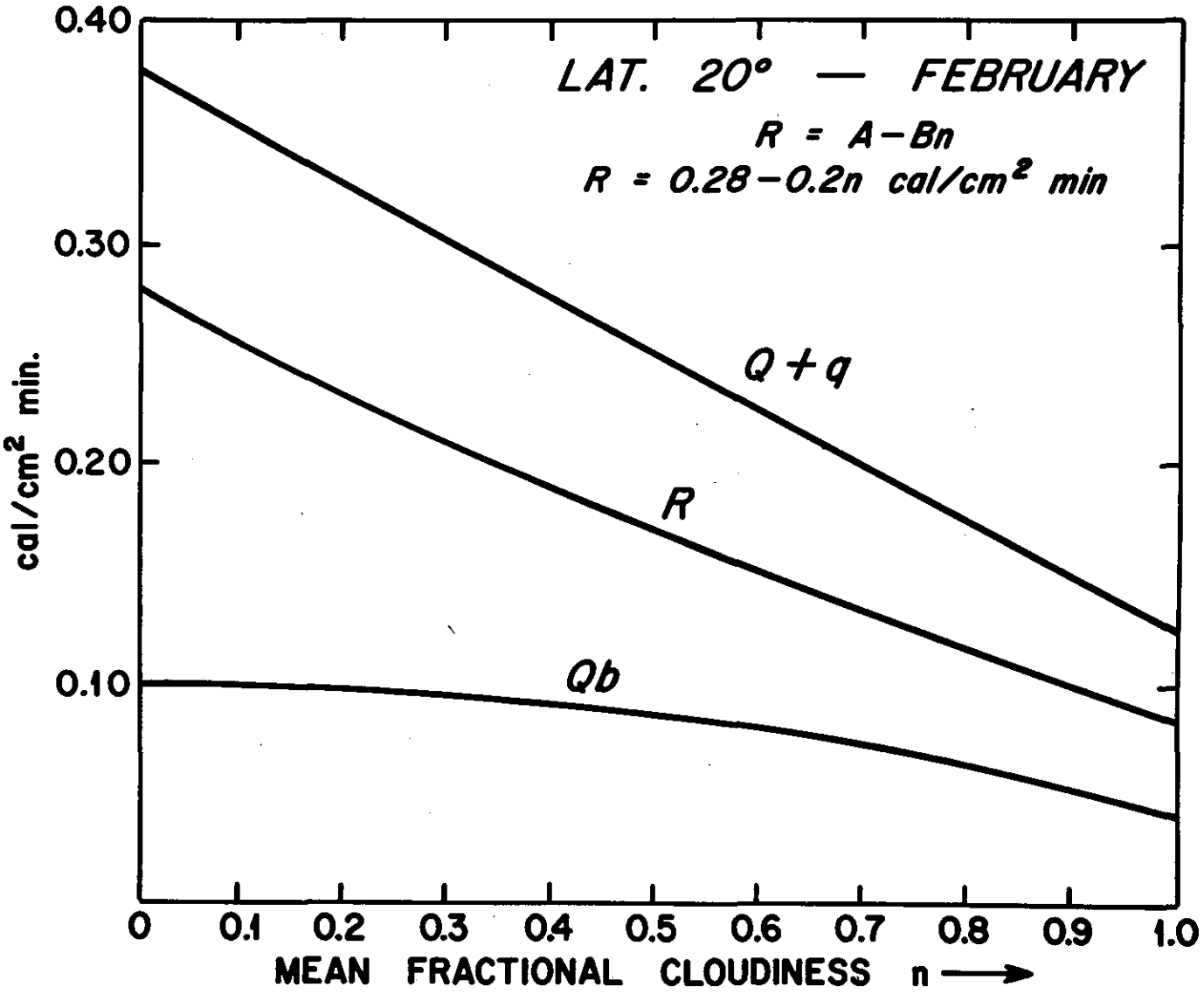

Figure 4. Empirically obtained graph of radiation balance components as functions of mean fractional cloudiness for latitude 20° in February. Adapted from Budyko's tables (see ref. 1).

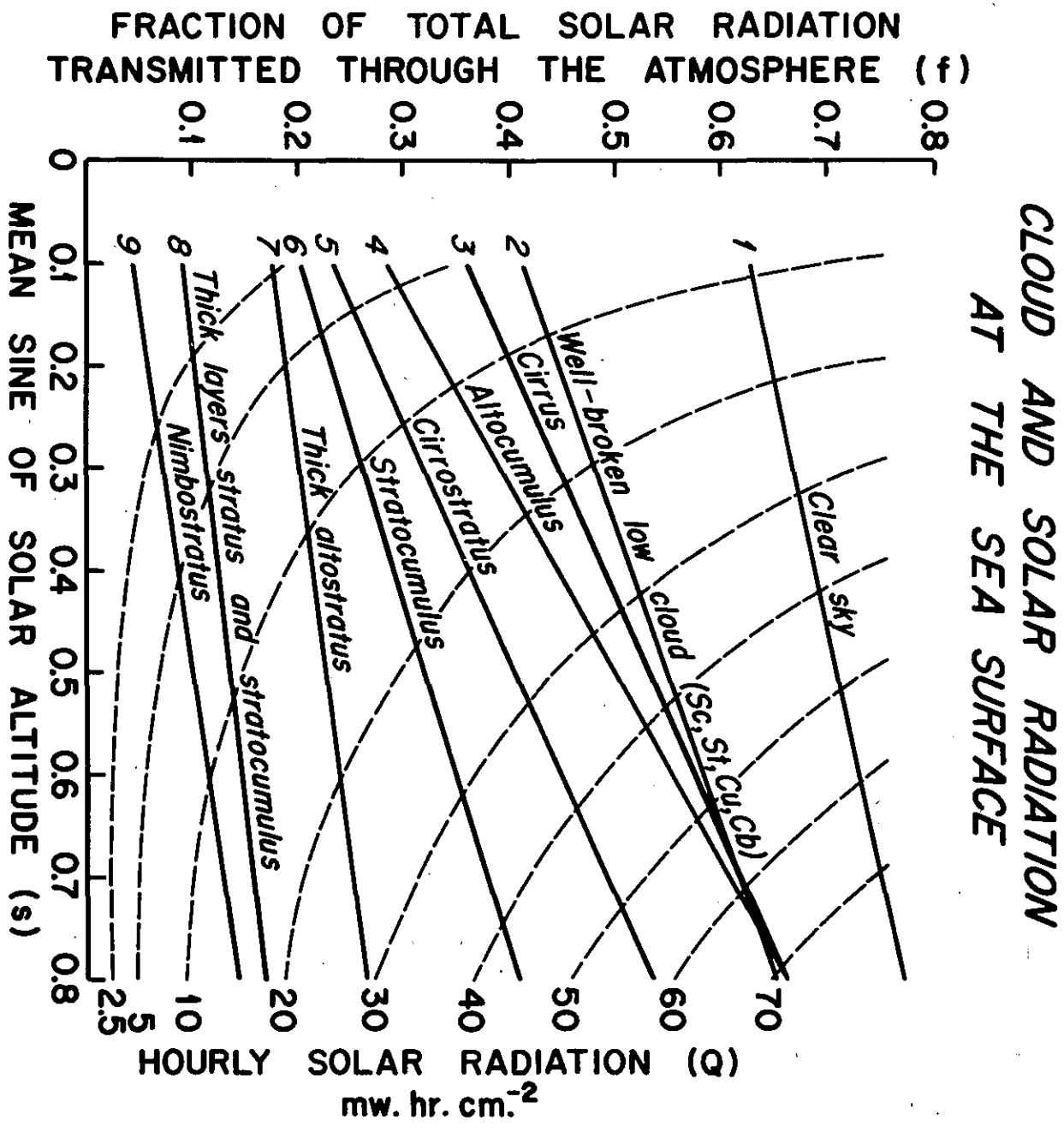

Figure 5. Fraction of solar radiation transmitted through the atmosphere as a function of cloud type and amount. (After Lumb.)

must be that cloud types and thicknesses, etc. are fairly reproducible at a given latitude in a given month. The empirical constants in (7) and (8) take this into account.

Well, where do we go from here and how can satellites help us to resolve this problem? The main contribution from satellites to global energy budgets comes in when we discuss the ocean-atmosphere system in the next section [6]. So far, satellite investigations have not been focussed directly on obtaining R, the sea surface radiation balance. One way to proceed with Q + q can be pointed out here. It would require surface measurements of R to be correlated with a satellite-derived sky code. When this is done we can code the satellite pictures and apply a better cloudiness reduction factor to the computed cloudless values of Q + q. The satellite experts say that they have satellite determination of Q_b under control, although they have not yet provided us a simple way to obtain it on a global grid. Today the best values of the oceanic heat budget components I can present to you involve radiation balances computed in the old way - although some encouraging measurement checks on the old way were made during the International Geophysical Year (IGY).

Satellites have aided this problem so far by providing better estimates of mean cloudiness over the oceans [9], although we do not yet have a long enough sample to be sure the averages are meaningful. In the next section we will check our entire budget structure with a satellite study.

Let us now look at the mean annual distribution of the oceanic heat balance components, in kg cal/cm^2 per year, as presented in Budyko's Atlas, by the methods I have discussed.

Figure 6 is the radiation balance. Note that the isopleths are pretty much parallel to latitude circles and that the radiation balance of the surface is positive everywhere up to latitudes 70°N and S. There is a slight diminution toward the equator due to increased cloudiness. The next two figures show the important sea-air fluxes of latent and sensible heat, as computed from the Jacobs transfer formulas.

Figure 7 is the mean annual distribution of evaporative heat transfer Q_e, after Budyko. There are four important features to note. 1) Very high evaporation occurs in the subtropics and trade-wind regions, ranging between 80-120 kg-cal/cm^2 per year or 250-375 cal/cm^2 day. The isopleth 120 kg-cal/cm^2 year means two meters of ocean water per cm^2 of surface are lost annually. 2) There is slight diminution in evaporation toward the equator because of the diminished radiation balance from cloudiness that I mentioned in connection with the last diagram. This reduction shows up in the transfer formulas via reduced sea-air temperature excess in equatorial regions as compared to the trades. 3) Evaporation diminishes rapidly poleward, except for very high values near the western boundaries. 4) There are zonal changes in evaporative heat loss, such that the local Q_e values may depart from latitudinal averages by a factor of two or three.

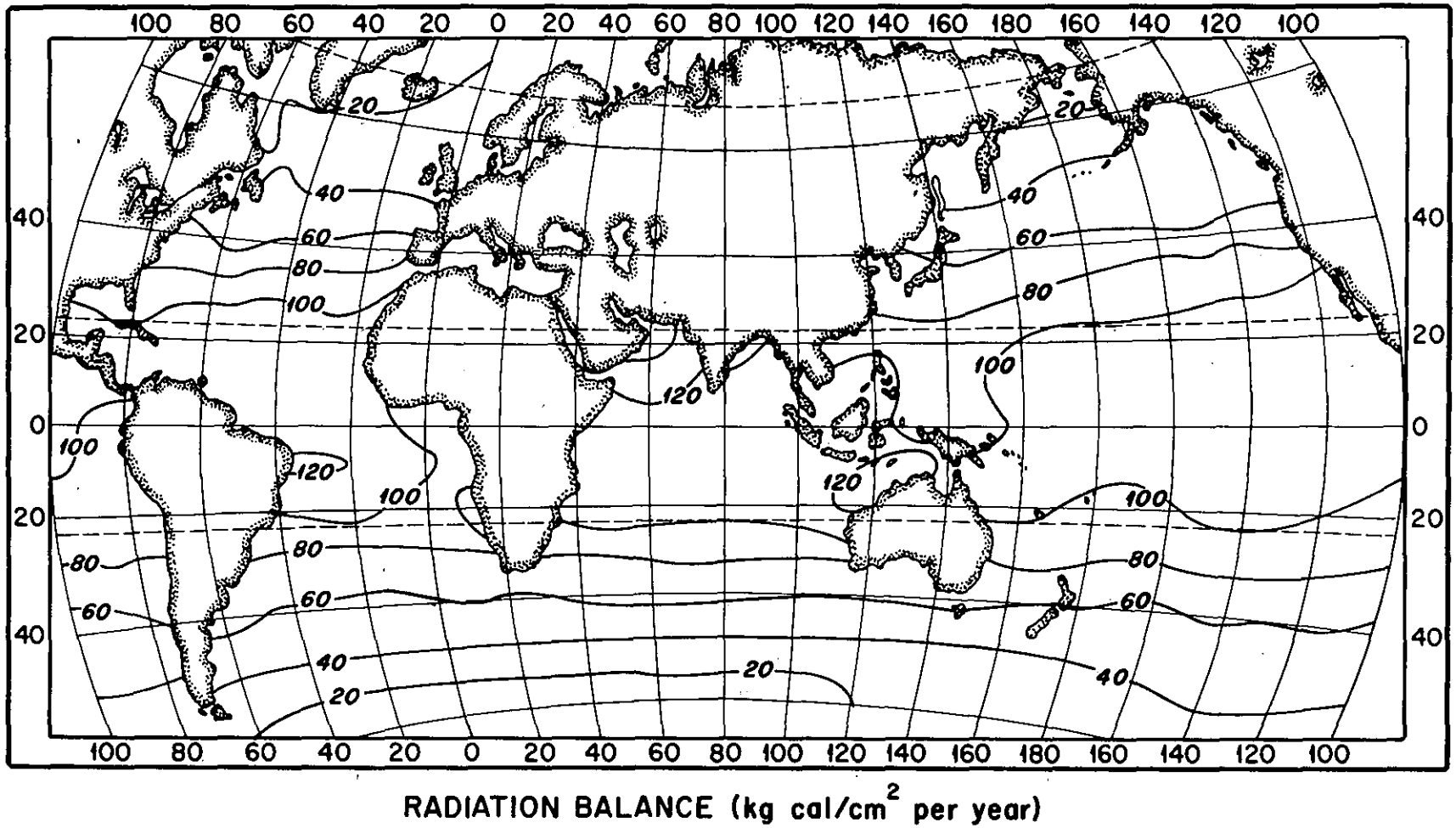

Figure 6. Mean annual radiation balance of the sea surface. (After Budyko.)

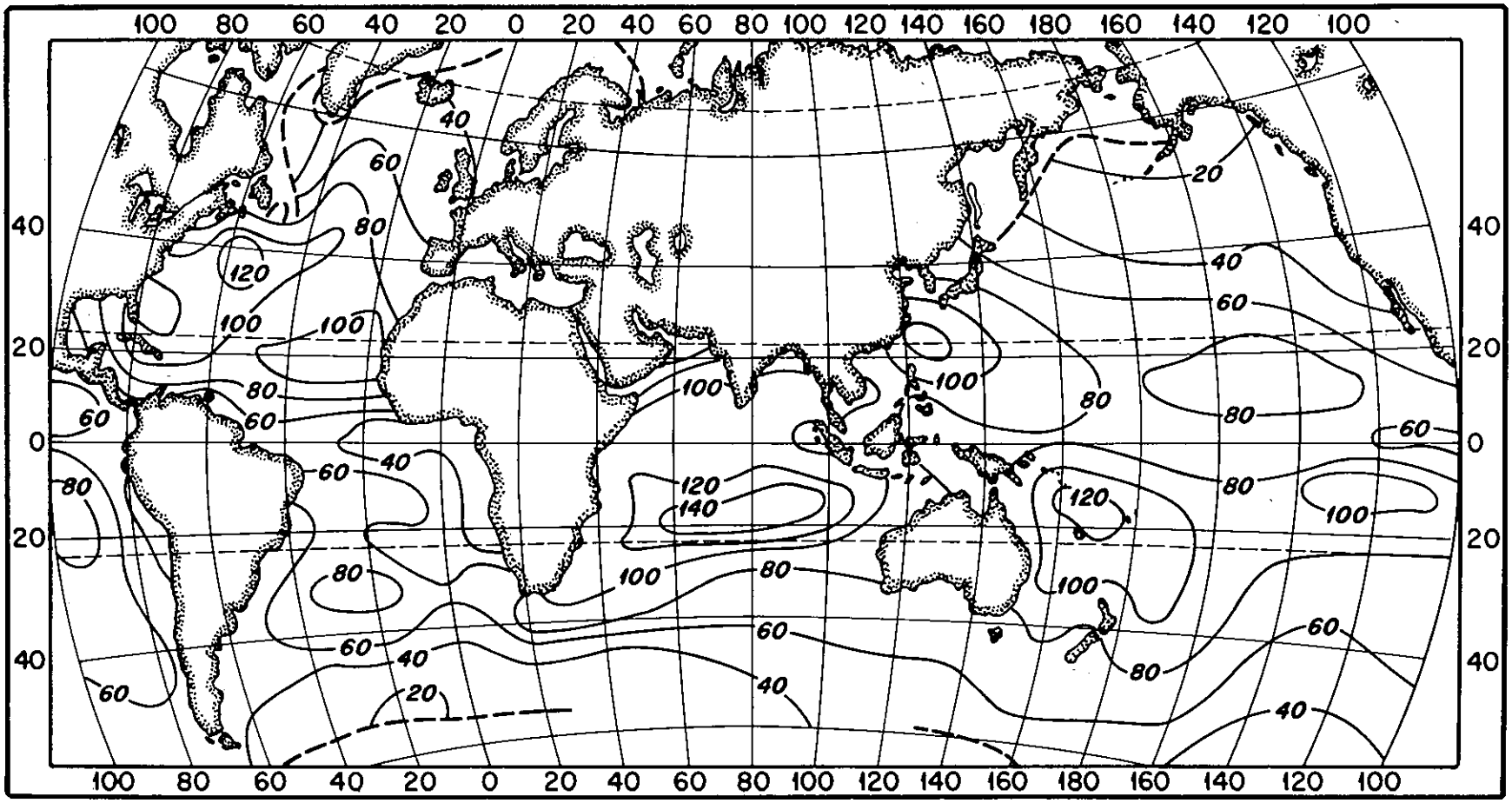

Figure 7. Mean annual latent heat transfer from sea to air. (After Budyko.)

The main reason for these zonal changes is clearly the presence of the warm and cold ocean currents which we saw in the first figure. All principal warm currents, such as the Gulf Stream, Kuroshio, and Brazilian Current, are associated with local maxima in Q_e, while cold currents like the Canaries, Benguela, California, Humboldt and Labrador currents are associated with low Q_e, or equatorward dips in the isopleths. The main difference between the Budyko maps shown here and the earlier values obtained by Jacobs is that Jacobs' fluxes show even more pronounced longitudinal anomalies than those in this diagram.

Figure 8 shows the distribution of sensible heat flux Q_s. The most outstanding feature of this figure is that the sensible heat flux is nearly everywhere positive - that is, directed from the ocean into the atmosphere. However, note that Q_s is small compared to the main heat budget components, namely Q_e and R. In fact, except for parts of the North Atlantic $Q_s/Q_e = r \approx 0.1 - 0.2$. In general, Q_s is large positive where the warm ocean currents prevail and small or negative where the cold ocean currents prevail. The large negative area in the south Atlantic and Indian Ocean, Budyko hypothesizes, is due to the advection of warm air masses over cool water, but many meteorologists believe that those values should not be taken too seriously. Firstly, data in the regions are scanty, and secondly the validity of the transfer equations is reduced when the air is stably stratified.

Figure 9 shows the result of finding the last heat budget

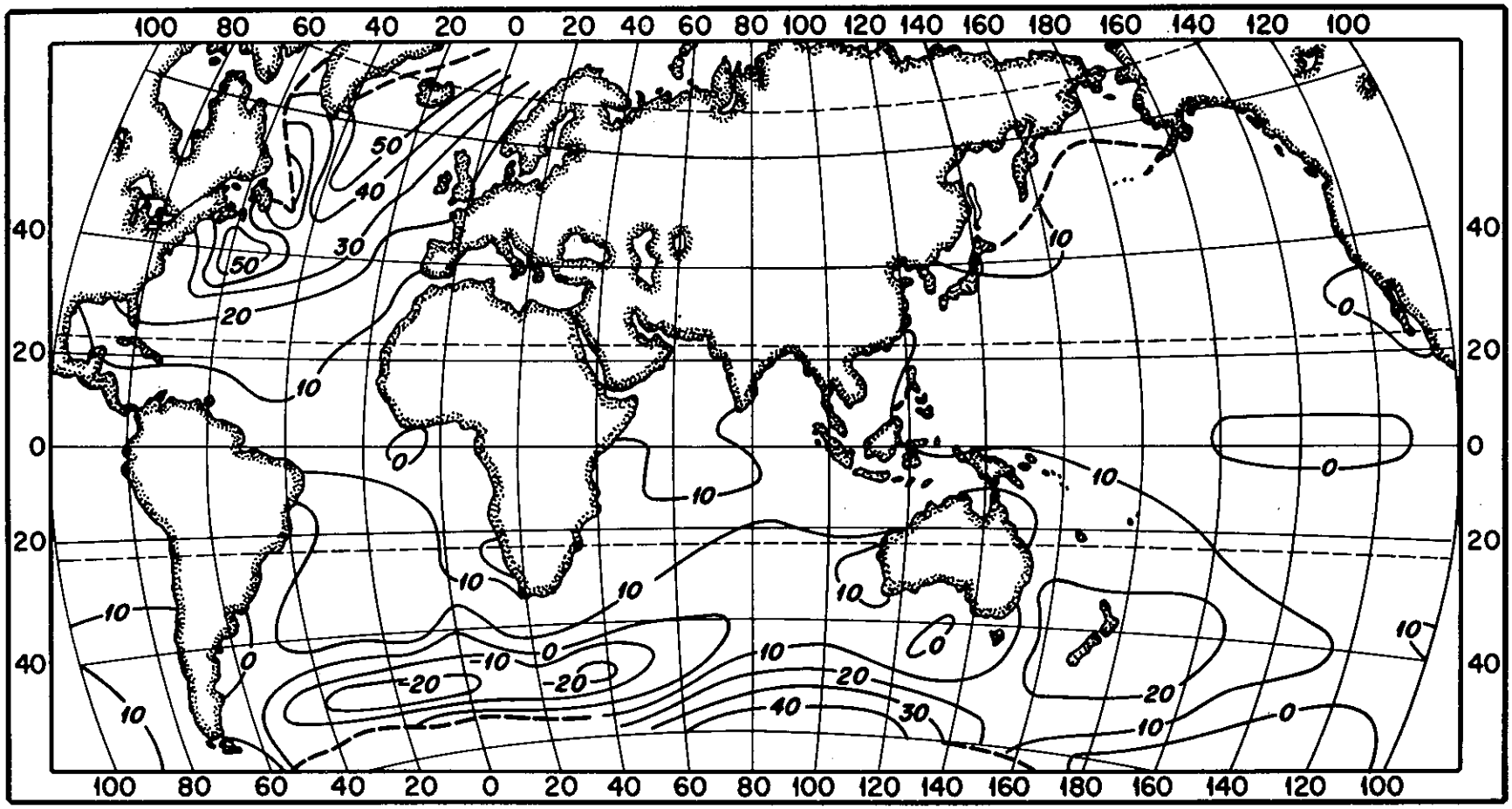

Figure 8. Mean annual sensible heat transfer from sea to air. (After Budyko.)

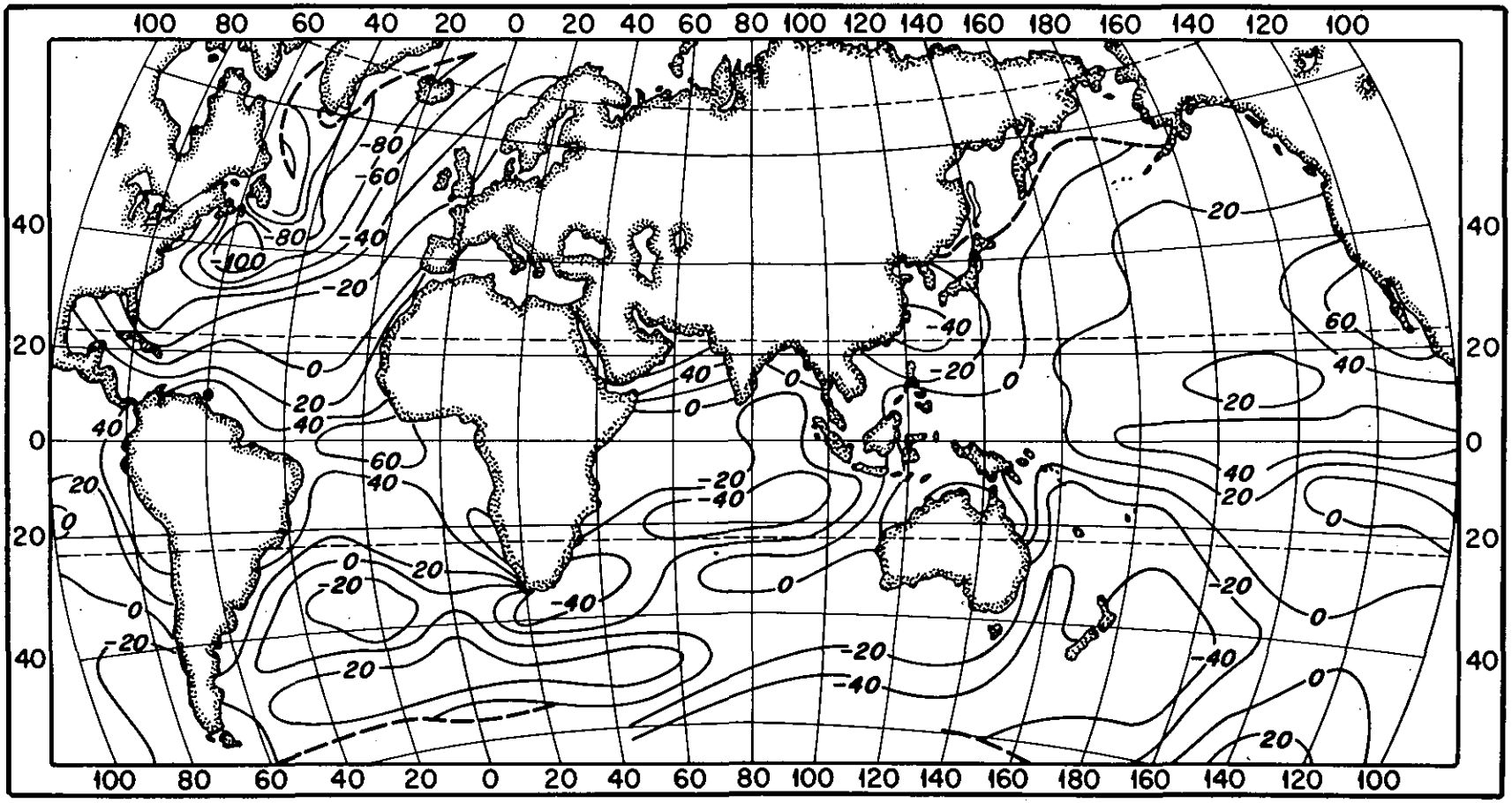

OCEANIC HEAT FLUX DIVERGENCE Q_{VO} (kg cal/cm^2 per year)

Figure 9. Mean annual distribution of oceanic heat flux divergence. (After Budyko.)

component as a residual in (1). The resulting distribution of Q_{vo} is shown. Q_{vo} is the oceanic heat flux divergence; it is positive where the ocean is taking on heat on an annual average, and negative where the ocean is giving off heat on an annual average. We see that taking on occurs in regions of cold ocean currents and vice-versa.

Before deducing too many consequences to geophysics, it is well to make careful tests of any residually-deduced quantity such as Q_{vo}, particularly to determine whether its important features could be due to uncertainties in evaluation. I have carried out quite a few such tests involving Q_{vo} [1]. Here, space permits only one example. Table 1 shows the oceanic heat balance components integrated longitudinally and averaged over 10° latitude. On the right, we compare the earth's surface radiation balance computed from the tables of London. The agreement with Budyko's surface radiation balance R is excellent equatorward of 30° and fair poleward. Since the mean latitudinal dependence of Q_e is agreed upon by all authors to a much smaller margin than radiation, or the size of the residual itself, we may substitute London's R for Budyko's in (1) to test Q_{vo}. While the negative values poleward of 30° are much decreased with London's R, the main features from 0-30°N are reproduced as is the change in sign north of 30°. Using this and other tests, all Northern Hemisphere evidence converges to support oceanic heat flux divergence south of 30°, convergence north of that, of a magnitude comparable to $1/3Q_e$ and thus not negligible in the planet's heat budget.

Mean Annual Distribution with Latitude of the Heat-Balance Components of the Ocean Surface

Units: kg cal/cm² year

Lat.	Oceans only, after Budyko (1956)						Whole earth, after London (1957)
	$Q+q$	R	Q_e	Q_s	Q_s/Q_e	Q_{vo}	R
60°–50°N	88	34	34	18	53%	−18	46
50°–40°N	109	54	51	15	29%	−12	63
40°–30°N	136	78	73	12	17%	−7	82
30°–20°N	151	100	85	7	8%	8	96
20°–10°N	156	110	89	5	6%	16	106
10°N–0°	149	107	76	5	7%	26	105
0°–10°S	152	107	81	7	9%	19	
10°–20°S	155	107	97	9	9%	1	
20°–30°S	147	94	87	10	11%	−3	
30°–40°S	128	73	77	12	16%	−16	
40°–50°S	104	53	57	5	9%	−9	
50°–60°S	84	31	37	12	33%	−18	
whole earth	128	77	68	9	13%	0	

Table 1

In other words, the oceans are taking on heat equatorward of the subtropical ridges and emitting it at higher latitudes, thus introducing an important factor in effecting a milder climate of temperate regions during the cold season. That this is qualitatively true we all know and it can hardly be otherwise. Quantitatively speaking, the tests I made convinced me that the deduced magnitudes are probably somewhere in the right ball park. We will see the clinching evidence on this in the next section. We can tentatively believe that the residual quantity Q_{vo} has some real physical meaning and exists outside the uncertainties of the calculation. This point is of the utmost concern to both meteorologists and oceanographers. To oceanographers particularly, the deduced magnitudes and distribution of Q_{vo} are crucial since it provides to date the only known way of arriving at a global picture of heat transports by ocean currents!

In order to compute the ocean current fluxes from their divergence, Q_{vo} may be integrated by mulitplying it by the ocean area between the given latitude belts and accumulating from some boundary latitude where the flux can be specified. This may be done separately for individual oceans or for the world as a whole. Before showing these transports, a further word of caution is in order. A sample calculation shows that with identical boundary conditions, a uniform 20 percent alteration in the magnitude of Q_{vo} leads easily to factors of two discrepancies in the deduced heat transports.

With this in mind, let us look at the next figure where the

integration with Budyko's Q_{vo} has been performed and compared with an earlier integration by Sverdrup, who used Kimball's radiation figures and Jacob's values of Q_e and Q_s.

Figure 10 shows the results when Budyko's Q_{vo}'s were integrated from pole to pole, assuming zero transport across each polar boundary. Sverdrup has only Northern Hemisphere figures and therefore had to assume a boundary condition at the equator. The northward heat transport across the equator in the Atlantic was inferred from direct oceanographic measurements. Sverdrup assumed zero flux across the equator in the Pacific for lack of any better information. Note that in the Atlantic there is fairly good agreement between Budyko and Sverdrup, while there is no agreement at all in the Pacific. All Budyko's fluxes in the Pacific are to the south, with a huge cross equatorward flux to the south. Considering what I said about a 20 percent error in Q_{vo} leading to 100 percent error in flux, I suggest we take these Pacific results with a big grain of salt. In 1962 Budyko revised his oceanic heat budgets and came up with allegedly improved values of R, Q_s and Q_e, although he arrived at them by the same old methods. One of my students at UCLA computed a new Q_{vo} from these new budget figures and came up with a lot more reasonable looking heat fluxes by ocean currents. Her paper appears in the references as number 19. In the North Atlantic the northward flux was reduced to slightly less than that of Sverdrup, with a corresponding small southward flux in the South Atlantic. In the North

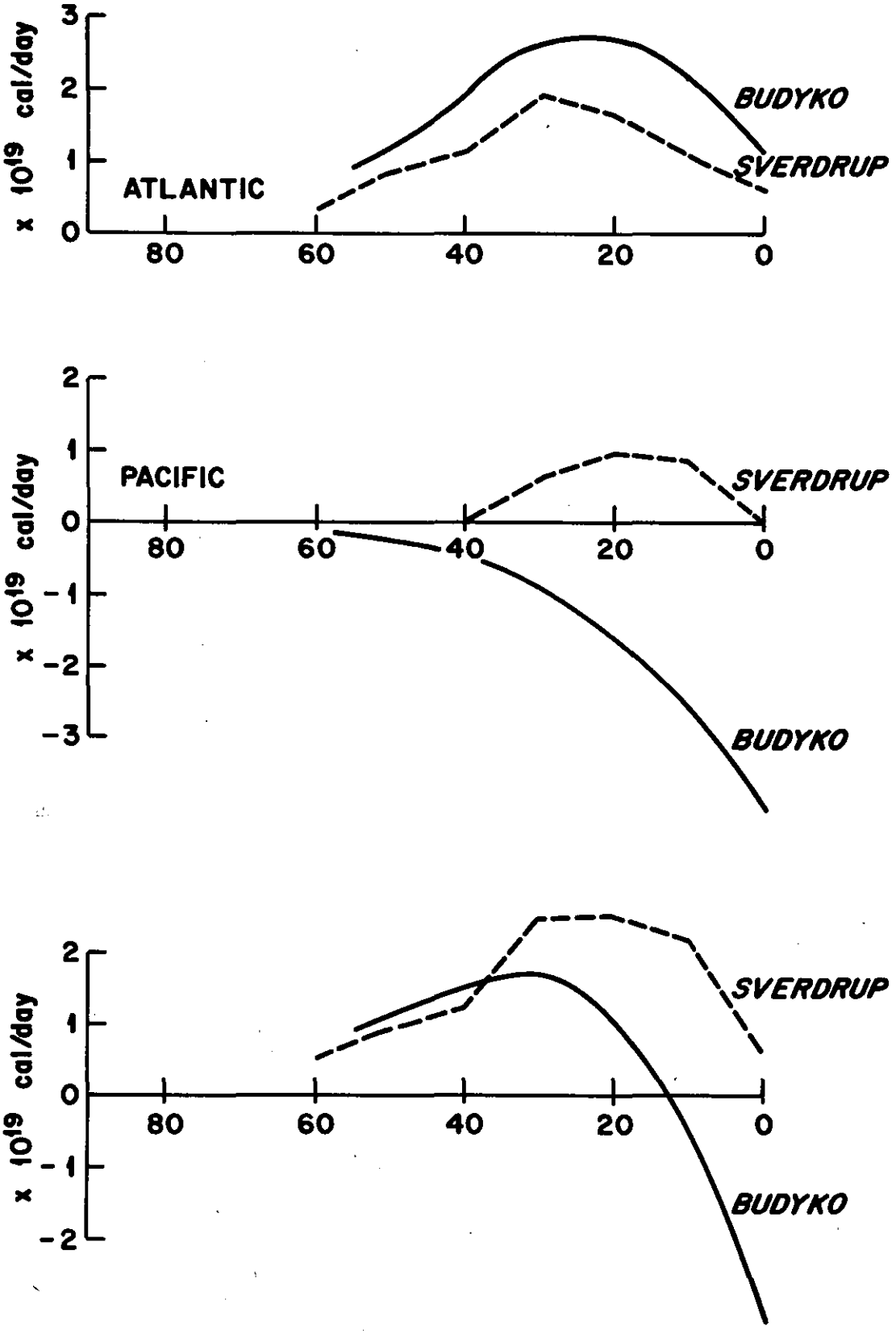

Figure 10. Poleward heat transports by the northern-hemisphere oceans, obtained by integrating Q_{vo} as described in text.

Pacific, the flux is northward north of 10°N with a maximum magnitude of about 1×10^{19} cal/day increasing to a large (-5×10^{19} cal/day) southward maximum amplitude at 20°S. This latter figure should again, I think be taken with some skepticism until it is verified in some other way. I will present the updated oceanic flux figures for the whole globe in the next section. The only oceanographic approach to these fluxes is by Kirk Bryan [18], to be mentioned further in the following.

The question naturally arises as to actually how large these deduced oceanic heat fluxes are - particularly how do they compare with the heat transports by the atmosphere? Does the ocean play an important or a negligible part in the planet's poleward transfer of heat energy? We will see a tentative answer to this question when we put all the pieces of the heat budget of the earth-atmosphere system together.

To summarize what we have learned so far, let us return to (1) for the annual balance.

$$R = Q_e + Q_s + Q_{vo}$$

We found that the ocean had a positive radiation balance, except poleward of the arctic and antarctic circles. If we average over the whole globe so that Q_{vo} goes out, we find that the ocean spends about 85 percent of its radiation balance on Q_e. This means of course that the atmosphere receives nearly all its energy input in the form of latent heat, i.e. in evaporated sea water. We shall investigate this more later. When we examine the heat budget on a

latitude-by-latitude basis, Q_{vo} is significant and may be as large as 1/3 Q_e. We deduce significant ocean transports from it, remembering the reservation that errors in R can throw these way off. So far, satellites have not helped us much with improving R directly. It is still computed with crude cloudiness values, which are at best satisfactory for whole latitude belts and whole months or seasons. We have as yet no immediate hope of using (1) on a daily basis until satellites together with direct R measurements help us to get reliable daily values of R. Even then, S and Q_{vo} present problems.

We will conclude this section with a brief discussion of the seasonal variation of the oceanic heat budget components.

So far as I know, only one oceanic region of the world, namely the Caribbean Atlantic, has enjoyed the month-by-month calculation of each one of its heat budget components. This was done by Colón [16] as a step toward obtaining Q_s and later precipitation to use in an energetic-dynamic study of the atmospheric trade-winds. This is a highly important study. The oceanic heat budget part of the results is shown in figure 11.

In figure 11, S and Q_{vo} have been computed from oceanographic data, R is computed in the manner I outlined earlier and the sum $Q_s + Q_e$ is found as a residual for each month. Q_e and Q_s are found by assuming a Bowen ratio of 0.1, which is justified by observations. Q_e and Q_s then checked out well against separate evaluation with the transfer formulas. Q_s and Q_{vo} are the small terms in the budget, although Q_{vo} averages

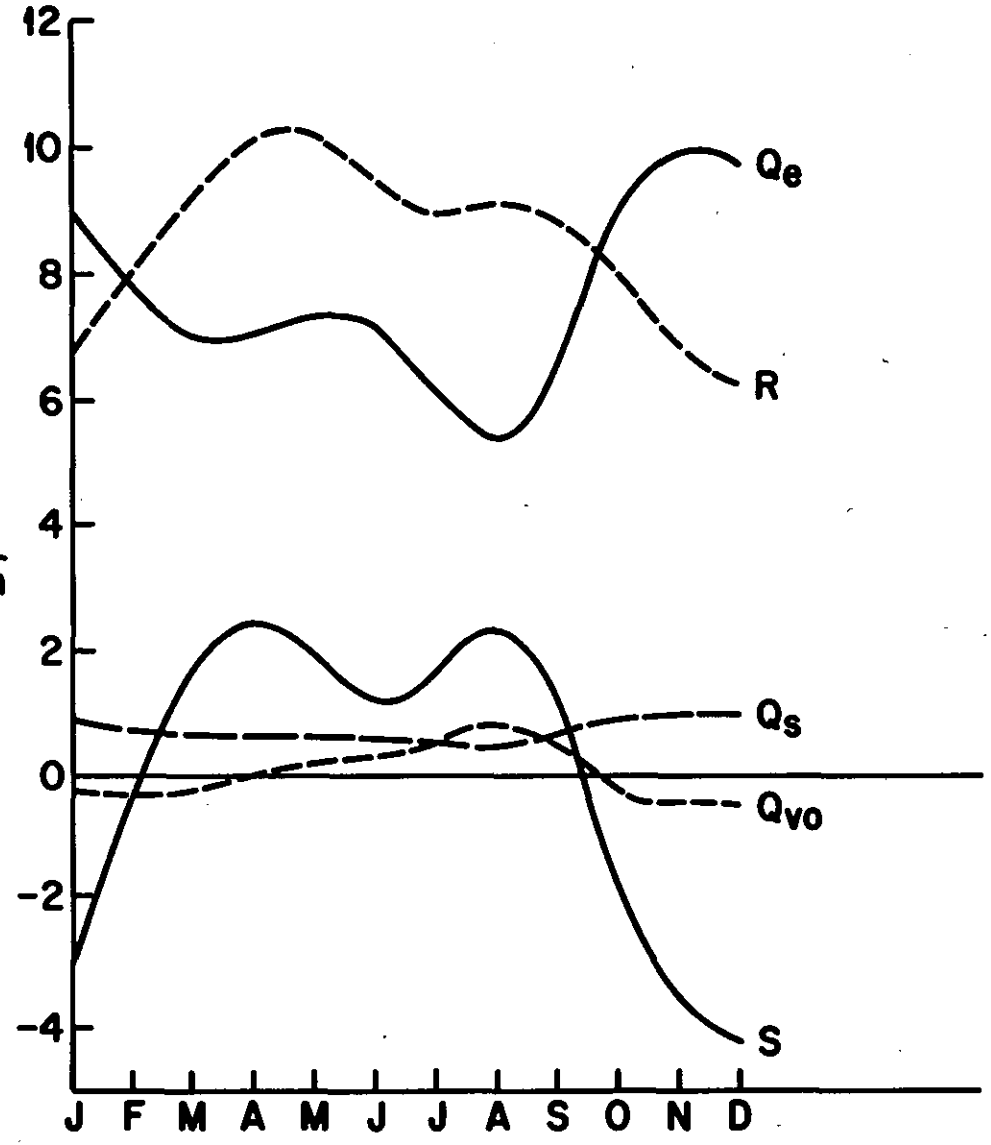

Figure 11. Heat budget components of the Caribbean Sea. (After Colon.)

positive over the whole year, so that the ocean is taking on heat as it should be. However, it gives off heat in the winter as the negative Q_{vo}'s indicate. Q_{vo} was actually computed from the velocities and temperatures of the horizontal ocean current which flows westward through the region. Note that the maximum of the radiation balance occurs in late May; the summer and fall downward trend is due to the cloudiness associated with the rainy season weather disturbances, which we will discuss later, again showing the effect of circulations upon energy budgets. The storage is negative in the fall and winter when the sea is cooling by giving up heat, and positive in the spring and summer when the sea is warming by taking on heat. Its maximum in December is roughly half the magnitude of Q_e and R. The storage was computed from 8000 bathythermograph soundings, with the assumption that seasonal temperature changes vanish at 90 m depth. Q_e has a maximum in winter and a minimum in summer, reflecting the storage cycle. In the transfer formulas, we find that the "reason" for the Q_e cycle is the reduced trade-wind speed in summer, as we saw earlier in the much weaker Hadley cell. Next, let us look at the opposite side of the ocean at the same latitude, in the region of the cold Benguela current off South Africa.

Figure 12 shows that a quite different exchange regime prevails. Here the expenditure of heat for evaporation, Q_e, is reduced by about a factor of four relative to the Caribbean. Unlike almost every other region, Q_s is negative - that is, directed from the atmosphere to the cold ocean

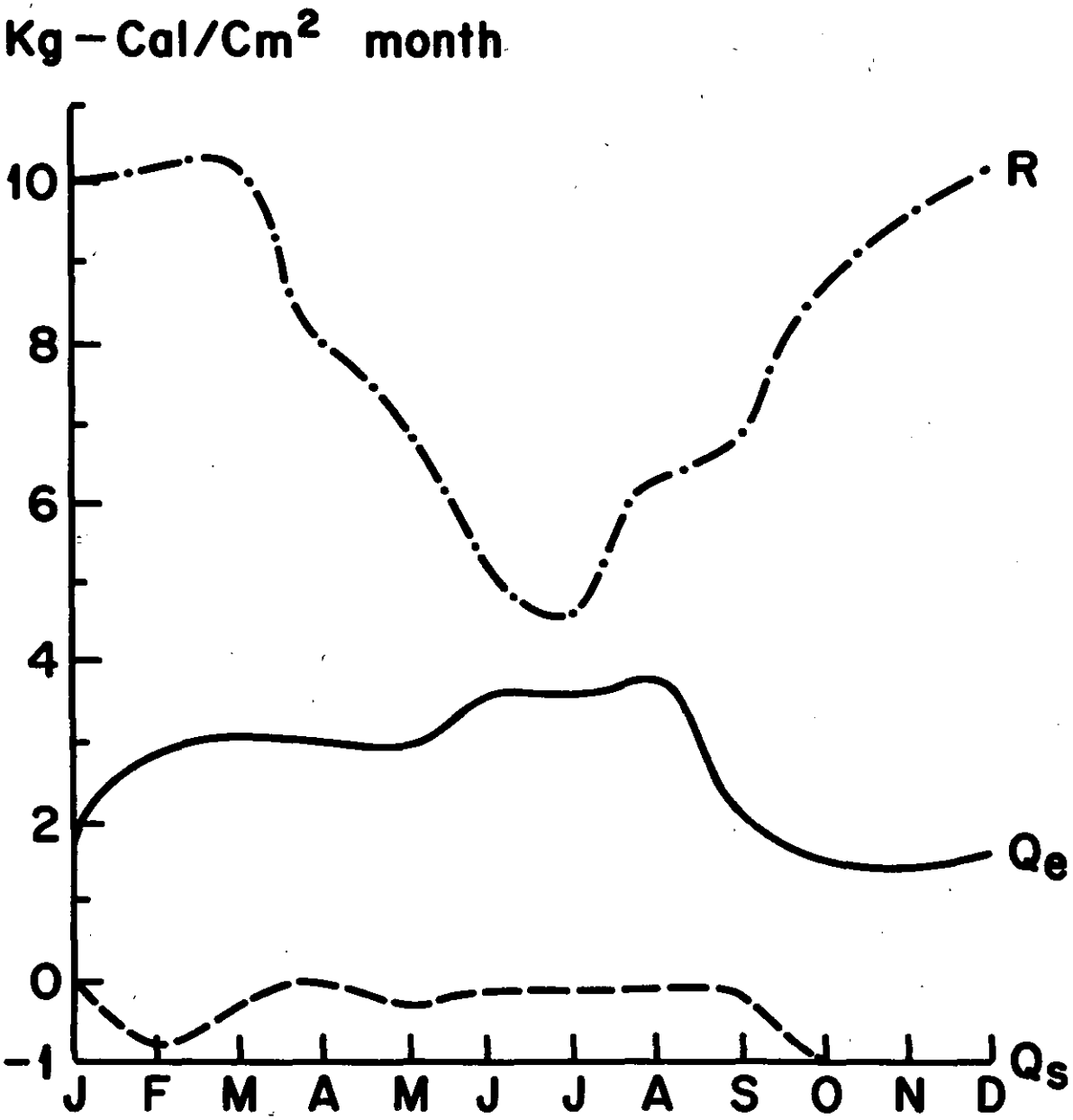

ATLANTIC OCEAN, 20° S, 10° E

Tropical climate of eastern periphery of oceanic anticyclones.

Figure 12. Heat budget components of the south Atlantic Ocean. (After Budyko.)

surface. It is larger negative in summer when the effect of the cold Benguela current is strongest. In this region, the ocean's gain of heat radiation balance and Q_s is much larger than its losses from evaporation and a great amount of heat energy is transmitted to the deeper layers which is spent on heating the cold water masses carried by the current.

Figure 13 shows the situation in the North Atlantic area affected by the Gulf Stream. At 55° latitude, the radiation balance of the ocean surface has a large amplitude, with pronounced negative values prevailing during winter. Here Q_s and Q_e are comparable. Q_s is largest for any oceanic region and is larger in winter than in summer. Q_e is also very large and shows a winter maximum. The ocean surface must receive a great amount of heat from lower layers to compensate for the total expenditure in evaporation, Q_s, and outgoing radiation. There is a very large negative sum of $Q_{vo} + S$ in the winter. Comparison of areas shows that release of locally stored heat is not adequate to provide exchange and thus Q_{vo} must average out large and negative - that is to say, the powerful heat transports of the Gulf Stream are drawn on to provide a significant part of the evaporative and turbulent heat fluxes from sea to air.

Next we will construct the mean annual energy budget of the earth-atmosphere system and discuss how the whole system works on an average yearly basis. Then we will start to inquire about the mechanisms of and fluctuations in sea-air interaction by examining its variations on the scale of synoptic-scale weather systems in the atmosphere.

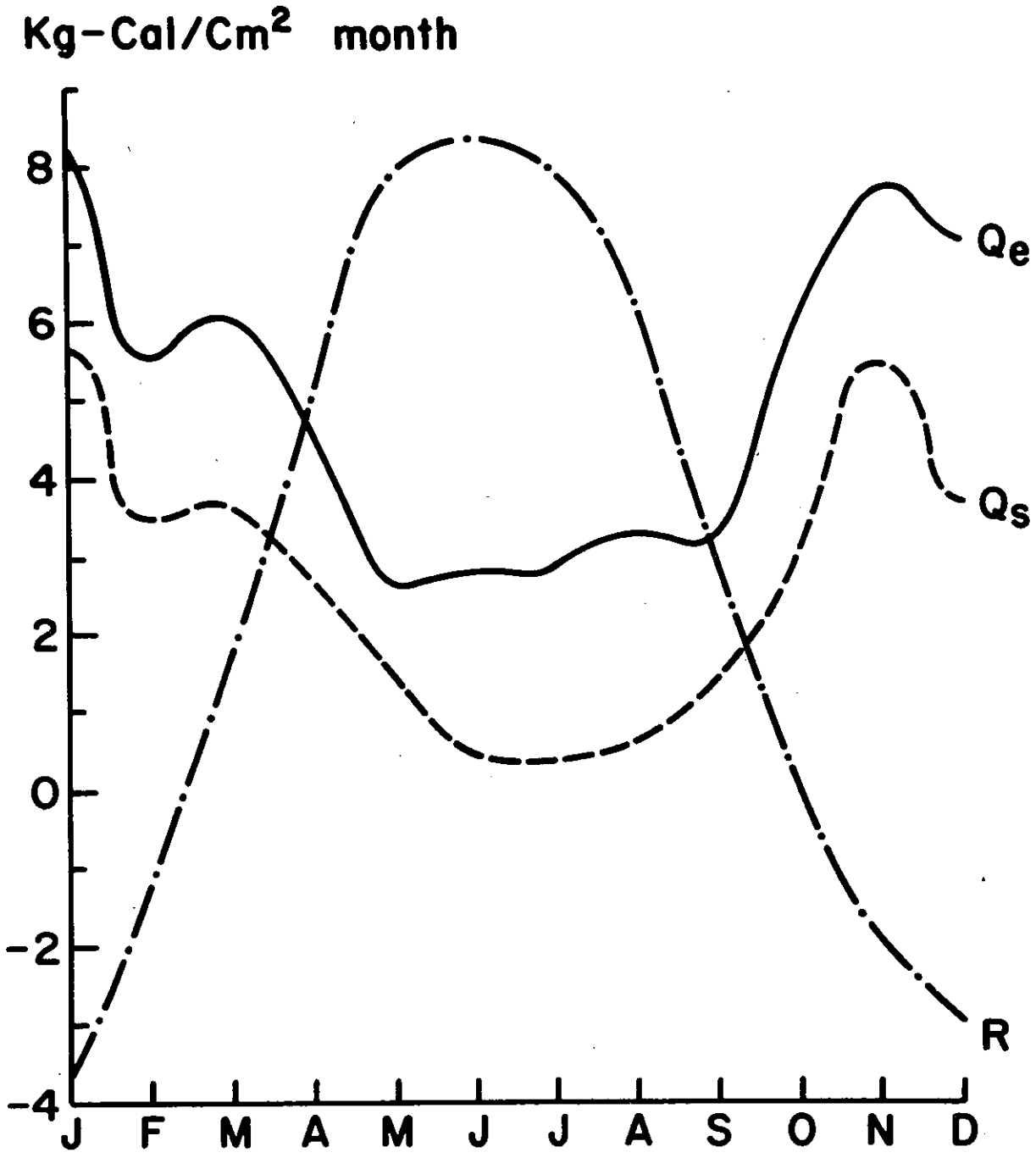

Figure 13. Heat budget components of the north Atlantic Ocean. (After Budyko.)

2. GLOBAL HEAT BUDGETS (CONCLUDED); AND SYNOPTIC VARIATIONS IN AIR-SEA INTERACTION

In section 1 we discussed the ocean's average annual heat budget using (1):

$$R = Q_s + Q_e + Q_{vo} \qquad (1)$$

We saw that the main ways the ocean gives off heat is in back or longwave radiation Q_b and in evaporation of sea water Q_e. We saw that Q_s was calculated as about $0.1\ Q_e$ equatorward of the subtropical ridges and about $0.2\ Q_e$ poleward. Q_{vo}, the oceanic flux divergence, had to be calculated as a residual and in some places it came out quite large. These analyses raise questions that are vitally important to marine scientists. Among these are questions concerning the relative importance of poleward heat transport in ocean versus that in the atmosphere. If the ocean does contribute an important fraction of the poleward heat transport, does it do so mainly by its horizontal gyres, or by vertical thermo-haline circulations or by lateral eddies? We found that Q_e is the ocean's main contribution to the atmosphere, but how and where is this water vapor fuel combusted to drive air circulations? How are the various scale wind systems created and what role do they play in sea-air exchange and in the driving of ocean circulations? The quantitative heat budget of the sea surface provides an initial foundation for pursuit of these

questions, but to build it further we must consider the mean annual heat budget of the joint air-sea system.

In order to analyze the joint annual heat budget, it is first necessary to formulate a conservation law analogous to (1) for a column of unit area extending from the top of the atmosphere down into the ocean interior, namely

$$R_s = L(E - P) + Q_{vo} + Q_{va} \tag{10}$$

The same small terms have been neglected as previously, as well as storage terms in sea and air. Air storage is always negligible compared to ocean storage and both average out when annual averages are being considered. P is precipitation in grams (or cm) per cm^2 per sec; E is evaporation in grams (or cm) per cm^2 per sec. Thus the term L(E - P) may be described equivalently either as the excess evaporation over precipitation rate at the ocean surface or as the flux divergence Q_{vw} of water vapor transport in the atmosphere.

$$Q_{vw} = L(E - P) \tag{11}$$

Q_{vo}, we recall, is the flux divergence of ocean heat transport in cal per cm^2 per sec. Q_{va} is the flux divergence of horizontal heat and potential energy transport in the atmosphere in cal per cm^2 per sec or very nearly the flux divergence of the transport of $C_p\theta$ where θ is potential temperature

$$C_p\theta \cong C_pT + AgZ \quad \text{(A is heat equivalent of work)}$$

The compressibility of air necessitates this formulation for the heat energy

transport in the atmosphere, since vertical ascent within a column may convert sensible heat into potential energy and conversely depending on the prevailing lapse rate. Some authors call the sum of sensible heat and potential energy "realized energy."

Our procedure for (10) will be to find Q_{va} as residual in this equation, then finally to integrate it to obtain the atmospheric flux of realized energy. We have enough aerological observations to make a good comparison. Q_{vo} is taken from the distribution showed earlier, where it was calculated as residual in (1).

R_s is the radiation balance of the entire column, or the difference between the short wave radiation absorbed and the net long wave radiation. Some of the most recent and complete radiation evaluations are cited in the references. Again, the greatest difficulty in these calculations resides in ascertaining the amounts of various cloud types and their radiative, reflective and absorptive properties, particularly in assessing the absorption of shortwave radiation in the atmosphere. One of these heat budget studies [6] is a satellite study, using the TIROS radiometers. The problems in it were different and caused by the gradual degradation of the radiometers and a possible drift in calibration which was corrected for empirically.

Despite the problems, all evaluations of R_s show that the earth-atmosphere system as a whole gains radiation heat equatorward of about latitudes 38° and loses heat by radiation poleward. If the high latitudes

are not to cool progressively with time and the low latitudes to warm up, specified transports in the earth's movable parts, namely sea and air, must take place. Thus (10) states physically that in regions of positive radiation balance the excess heat energy may be carried away by sensible heat transport in the ocean and by a combination of latent heat, sensible heat and potential energy export in the atmosphere, while regions of negative radiation balance must make up the deficit by corresponding imports. Therefore, computation of R_s as a function of a latitude immediately permits assessment of the total heat energy flux divergences in sea and air together (sum of terms on right side of (10)) and by integration, enables the total heat energy flux across latitude circles to be obtained. A figure shows the results of this computation shortly, but first we must look at the distribution of precipitation.

Adequate assessment of oceanic rainfall has posed a problem. Direct shipboard measurements are difficult and have only been obtained reliably in a few short-period research programs. Buoys are coming into existence which can measure rainfall and can be interrogated by satellite. So far only one has actually been used, for a 100-day period during BOMEX in 1969. This is still a long way from a global network.

So the rainfall distribution in figure 14 was obtained in 1953 by extrapolation from land and island stations. Debates have raged in the literature about whether precipitation is increased by land and island effects.

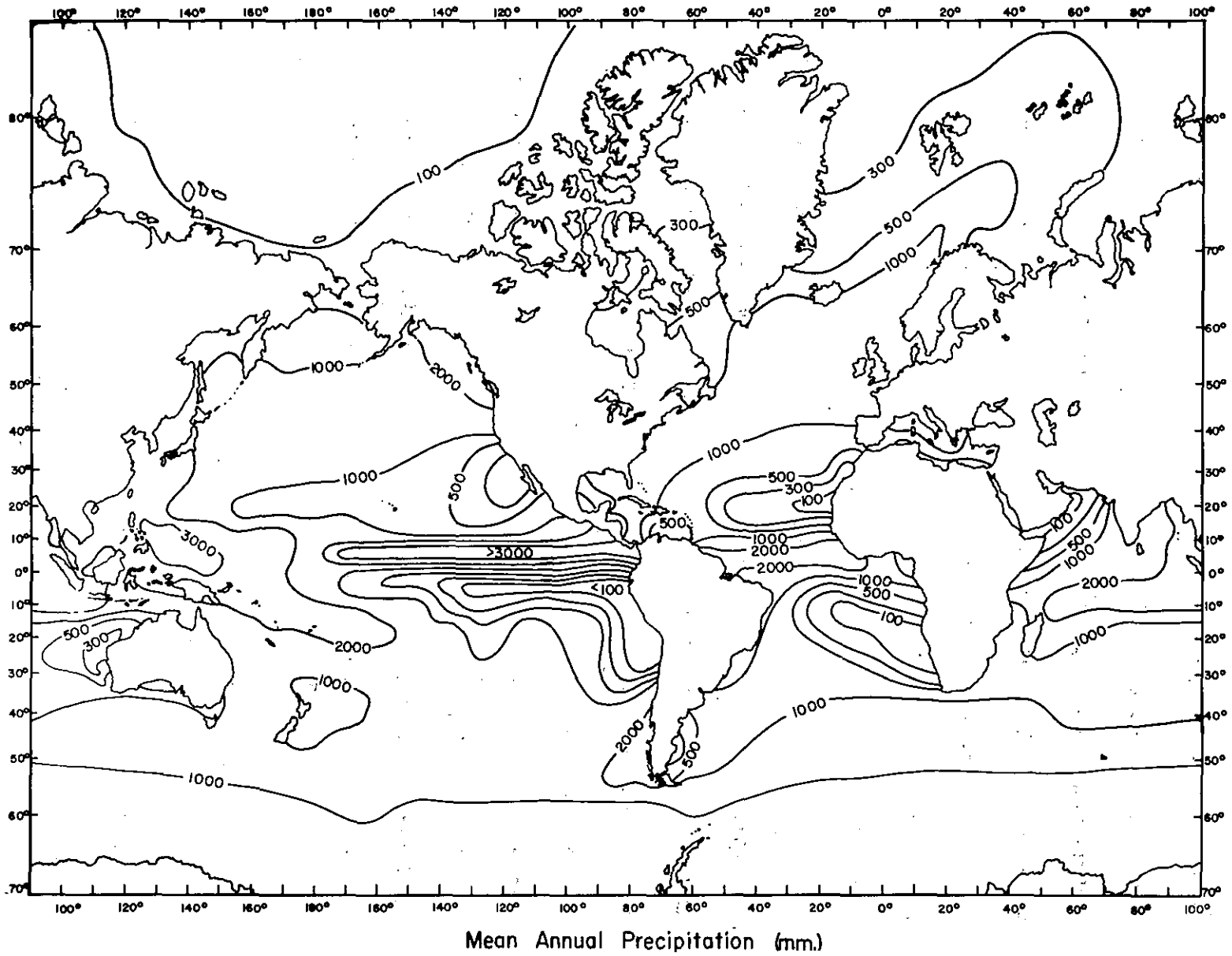

Figure 14. Mean annual precipitation over the oceans. (After Budyko.)

In the old days it was found necessary to reduce oceanic rainfall by 20 - 30 percent to effect a global water balance and this reduction was explained away as compensation for the land effect. In using figure 14, the Soviet authors found they only had to reduce the values shown by 10 percent to get water balance, both for the globe as a whole and for individual oceans. We can for the time being either regard this 10 percent reduction as a land effect, or if we are more cynical, as a "fudge factor" well within the accuracy of determining either precipitation or evaporation.

Figure 15 shows the values of P, E and E-P by latitude after averaging over longitude. Now for the first time we see the firebox function of the equatorial trough zone in the atmosphere exhibited by the huge release of precipitation just north of the equator. Here is where the water vapor fuel picked up by evaporation in the trade-wind region is combusted, i.e. converted by condensation and precipitation into sensible heat plus potential energy. A secondary P maximum is found in the cyclone belt. Note the asymmetry in the P curve, due to mean position of the equatorial trough in the northern hemisphere. This means there must be a southward transport of water across the equator and a northward transport of water vapor. In the bottom curve we compare two independent estimates of E-P. The solid curve uses the E and P measurements we have shown in the figures (right side (11) while the dashed curve is Q_{VW} from the measured atmospheric fluxes for 1958 only[17] (Starr et al.). Considering the uncertainties, the

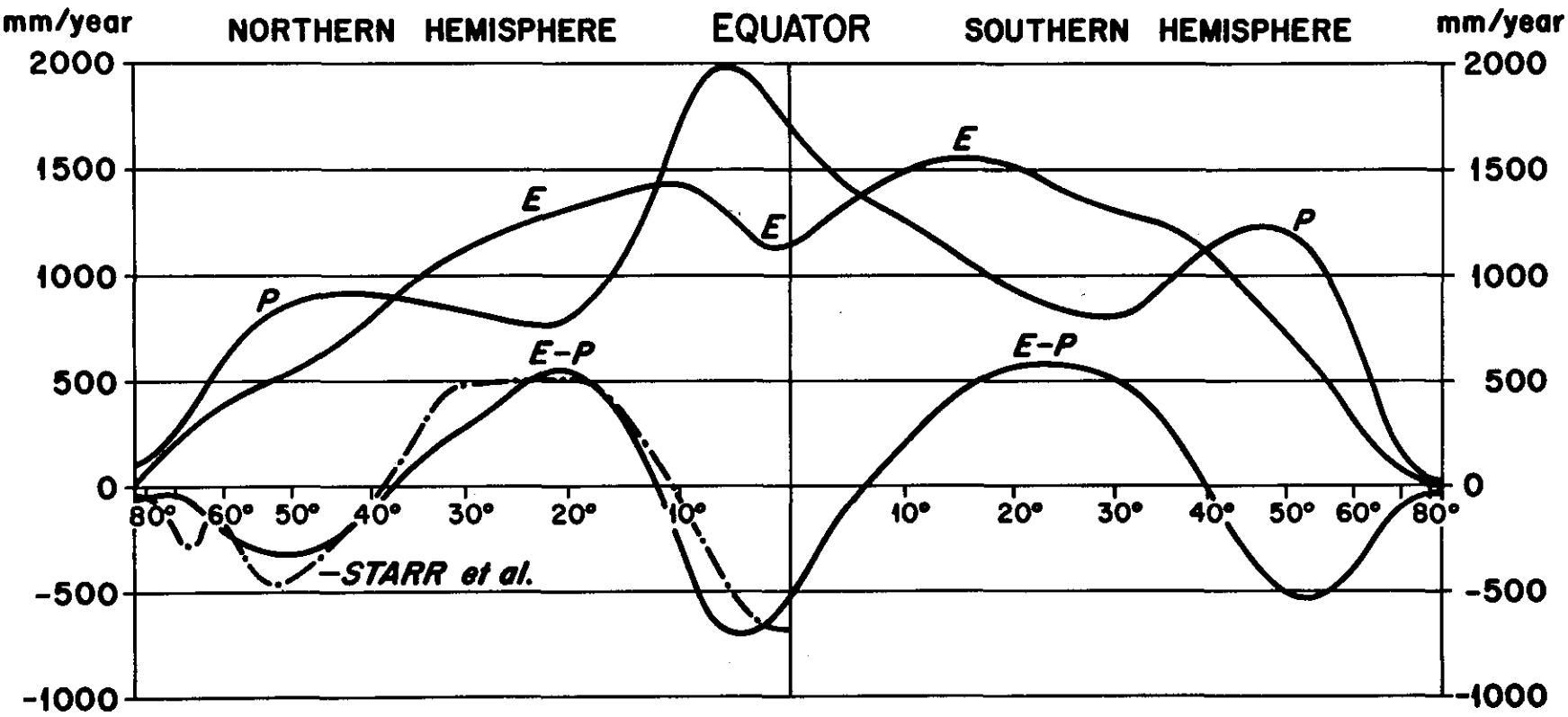

Figure 15. Longitudinally integrated values of mean annual precipitation P, evaporation E and their difference, E-P, as functions of latitude. (After Palmen and Newton.)

degree of agreement is very encouraging.

In figure 16 we plot together the latitudinal dependence of each component of the budget of the air-earth system. The three best assessments (by the classical method still) of R_s are compared. I have compared the integrated fluxes [1] from these different radiation measurements; those of London give 50 percent smaller heat transport by the sea-air system than do the larger values of Houghton and Bagrov. We will look at some checks shortly on the residually-calculated Q_{va}, the atmosphere heat and potential energy flux divergence, including a satellite study.

Using this diagram, we are now prepared to place a quantitative foundation under the discussion of the whole system's operation and climatology.

As can be seen in figure 16, four basic latitudinal zones exist in both hemispheres, each with essentially a different relationship between the heat balance components. In the equatorial zone (which extends 10-15° on either side of the equatorial trough) the gain of heat from positive radiation balance is supplemented by a comparably large net release of precipitation heating (flux convergence of water vapor). These together assure the great export of heat by atmospheric and oceanic transport, for which the relatively narrow region from 0° to 10° latitude constitute the primary energy source. This diagram clearly demonstrates that the equatorial trough plays its role as atmospheric firebox not solely or even mainly due to excess

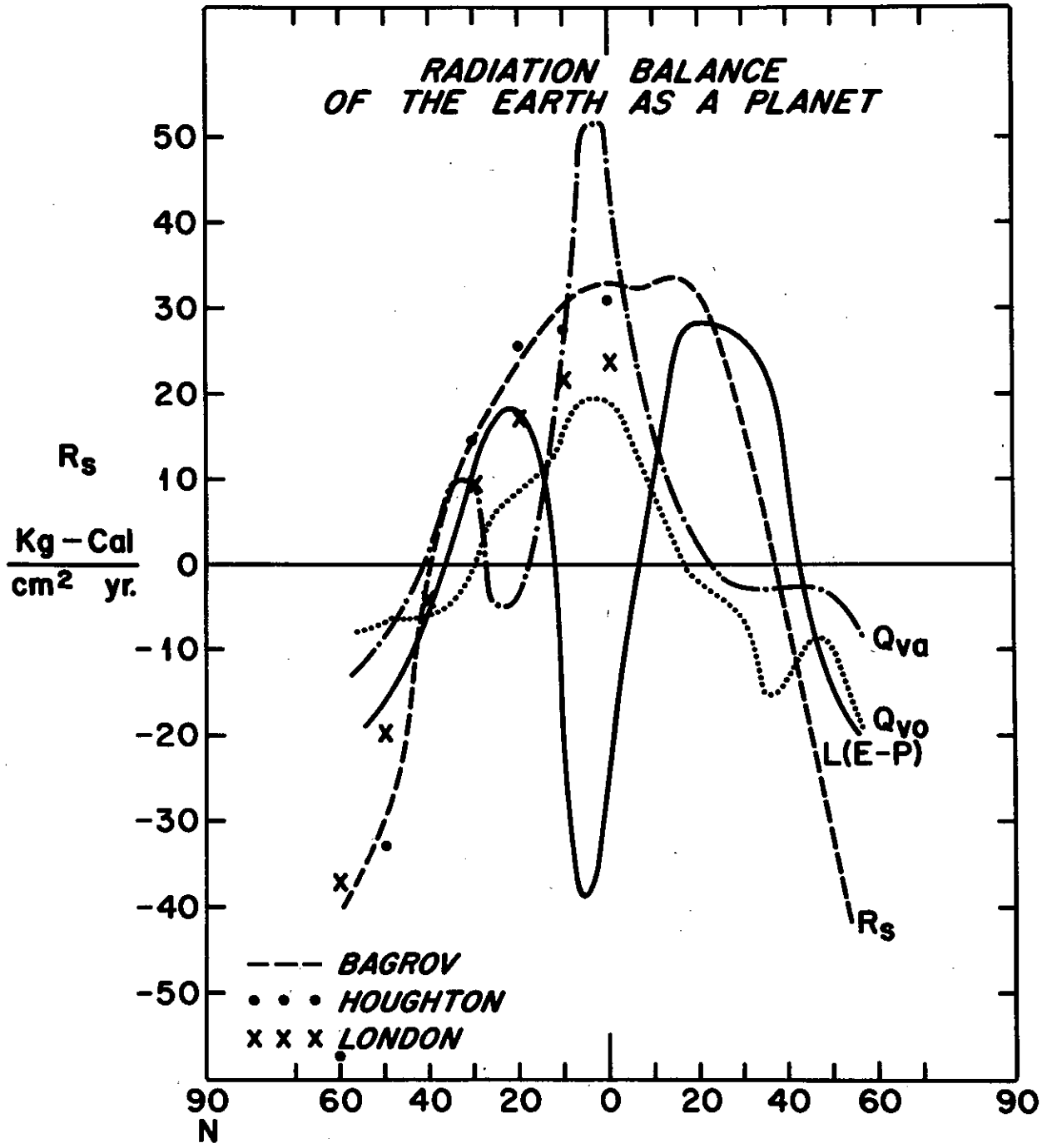

Figure 16. The radiation balance of the earth as a planet, showing the latitudinal dependence of its major components. R_S is the radiation balance of the earth-atmosphere system. Q_{VO} is the flux divergence of heat in the oceans. Q_{Va} is the combined sensible heat plus potential energy flux divergence in the atmosphere. L(E-P) is the same as Q_{VW} the water vapor flux divergence in the atmosphere. (After Budyko, with comparisons to other investigators by the author.)

radiative energy received, but even more largely because there the water vapor fuel is combusted by precipitation release, an energy source which is closely tied to circulation dynamics. The mechanism of release is large cumulus clouds, whose operation will be described later. Northward and southward from the equatorial zone are the tropical regions, i.e. the location of the atmosphere's famous easterly trade-winds which prevail thoughout the equatorward side of the subtropical high pressure cells or "ridges." In these zones, with a positive radiation balance (diminishing with latitude), a large expenditure of heat for net evaporation is observed. In the major portion of the trade-wind regions, the loss of heat for moisture exchange (evaporation from the sea into the air) approaches the value of the radiation balance and thus the input to sensible heat and potential energy flux (Q_{vo} and Q_{va}) is small. The fact that the trade-winds act as fuel accumulators for the atmospheric heat engine is thus also shown quantitatively in this diagram. In the subtropical ridge region of 35° - 40° latitudes, a transitional zone is found. In this latitude belt, the gain and expenditure of heat in all the budget components is fairly evenly distributed and no single component is numerically large. As we shall see soon, however, the poleward fluxes themselves are a maximum at these latitudes. In the high troposphere, this is the average position of the famous subtropical jet stream, whose wave-like meanders provide the channels of poleward energy flow from the tropics. Thus the temperate atmosphere is fed with the heat to balance its radiation loss and to

store in potential energy of air mass contrasts, a small fraction of which is released to maintain the cyclonic storms, which themselves control the sea-air fluxes in mid-latitudes as we shall see later.

Poleward of the subtropical ridge and jet stream, all higher latitudes are regions of radiation deficit, increasing rapidly toward the poles. Energetically this zone lives on imports: from excess precipitation over evaporation, atmospheric advection and sea-current transports.

The next figure (figure 11) is the climax of the work so far showing the integrated flux divergences, i.e. the energy transports themselves. In looking at this figure try to keep in mind the circulations that are carrying out the transports.

Figure 17 shows the results obtained by integrating each term in (10) from pole to pole, using the best and newest available values for the flux divergences. The solid line, or total flux is obtained by integrating R_s. Note the maximum across the subtropical ridges and the small southward flux across the equator to make up a small southern hemisphere deficit which is not found by the satellite study. It is within the present-day errors of determination. Note particularly that oceanic flux is comparable to that of the atmosphere at low latitudes. The most comprehensive check of the ocean flux using oceanographic data and methods is found in Bryan [18]. The author, Kirk Bryan, concludes that most of the oceanic heat flux is effected not by the horizontal gyres, which we showed you in figure 1, but in much weaker,

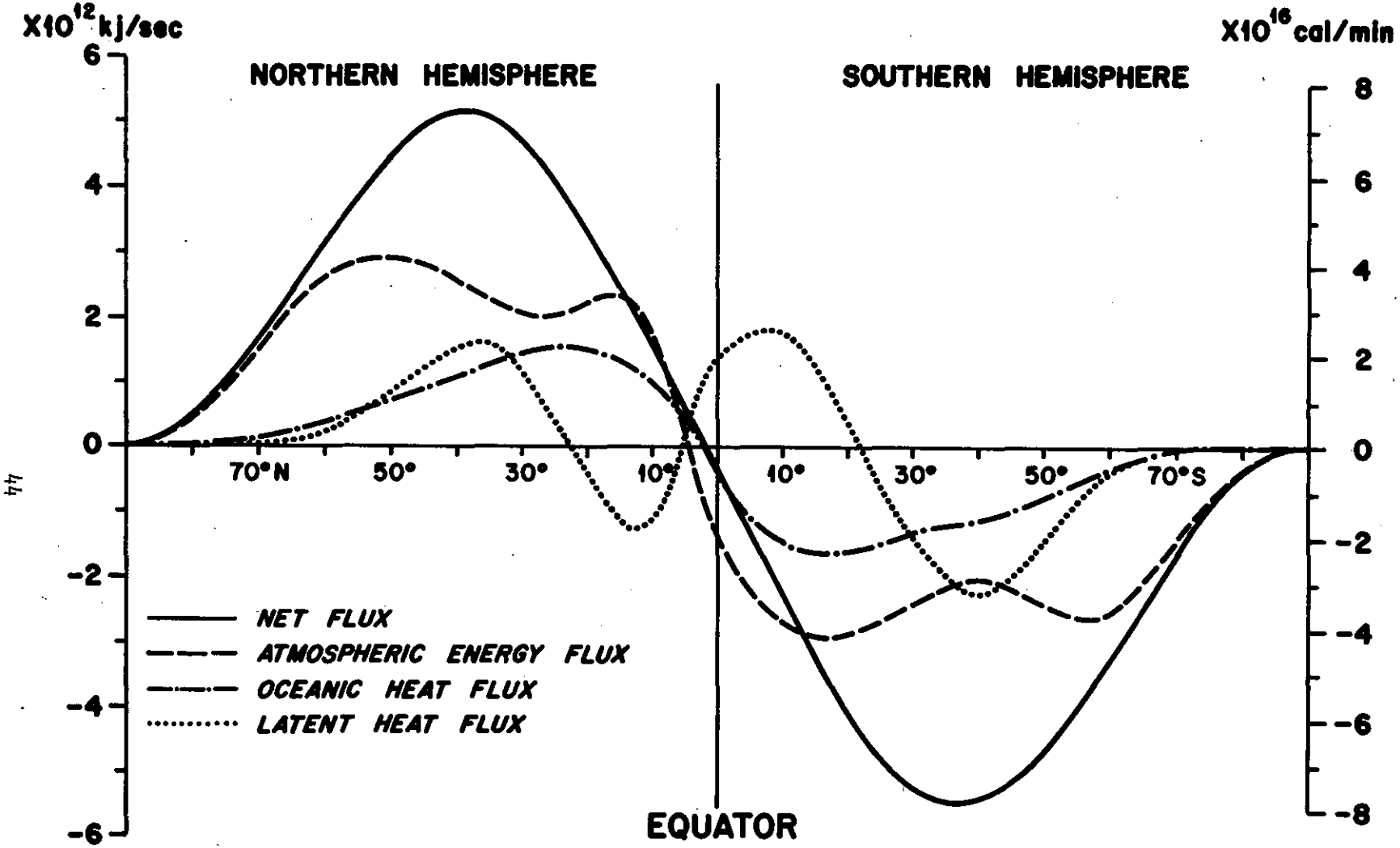

Figure 17. Northward transports of energy by oceans and atmosphere, computed by integration of source and sink terms similar to those in figure 16. Units are (right scale) 10^{16} cal/min or (left scale) 10^{12} kilojoules/sec. (After Palmen & Newton.)

meridional thermohaline circulations analogous to the Hadley cells in the atmosphere. This is quite puzzling in view of the good agreement we saw between the Q_{vo} distribution and the location of the warm and cold ocean currents. The last, or maybe barely the first, word has clearly not yet been said on heat transports in the ocean.

Note the small but still significant southward oceanic flux across the equator, which comes from the difference between a large southward flux in the Pacific, partially compensated by a smaller northward flux in the Atlantic.

The atmospheric water vapor fluxes (deduced from integrating L(E-P)) are mainly confined to low levels where the air's moisture content is high. Note the equatorward flux of vapor in both Hadley cells, with a poleward flux farther north and south. The vapor flux across the equator is northward, due to the asymmetrical location of the equatorial trough in the northern hemisphere, so that the southern hemisphere Hadley cell on an annual average protrudes a little way into the northern hemisphere. Note that at the equator, the northward flux of water vapor in the atmosphere is exactly balanced by a southward flux of realized energy, accomplished by the upper branch of the southern hemisphere Hadley cell. The most outstanding feature of the atmospheric flux of sensible heat plus potential energy is the double maximum in both hemispheres, one just poleward of the equatorial trough zone and the other just poleward of the cyclone belt in the

Westerlies. Fortunately we have a direct check upon the integrated Q_{va} from aerological measurements, as well as a satellite check upon the whole business.

Figure 18 shows the comparison between the flux required for energy balance and the same flux computed from aerological observations for three winter and three summer seasons. Note the good agreement which is well within the error of either determination.

In figure 19 we compare these computed fluxes with the same fluxes obtained when the TIROS satellites' radiometers are used to obtain R_s. Before we examine the figure, it is necessary to describe briefly the satellite study. The incoming short-wave radiation is calculated from the formula

$$E_s = E(1 - \bar{A})$$

where E is the average radiation flux incident at the top of the atmosphere for the month and $\bar{A}$ is the monthly mean albedo for the latitude belt. The values of $\bar{A}$ are based on TIROS VII measurements in channel 5(0.5 - 0.7μ) as corrected for degradation in response of the radiometer. The outgoing terrestrial radiation in the far infrared is measured by TIROS VII's channel 2 and monthly values obtained for each 10° latitude belt. R_s are obtained by subtraction. The authors, Rasool and Prabhakara [6] used the same values of L(E - P) as Budyko did and figure 19 shows the integration for the sum of Q_{vo} and Q_{va}, in other words, the sum of the oceanic heat transport and the realized energy transport in the atmosphere. The agreement is remarkably

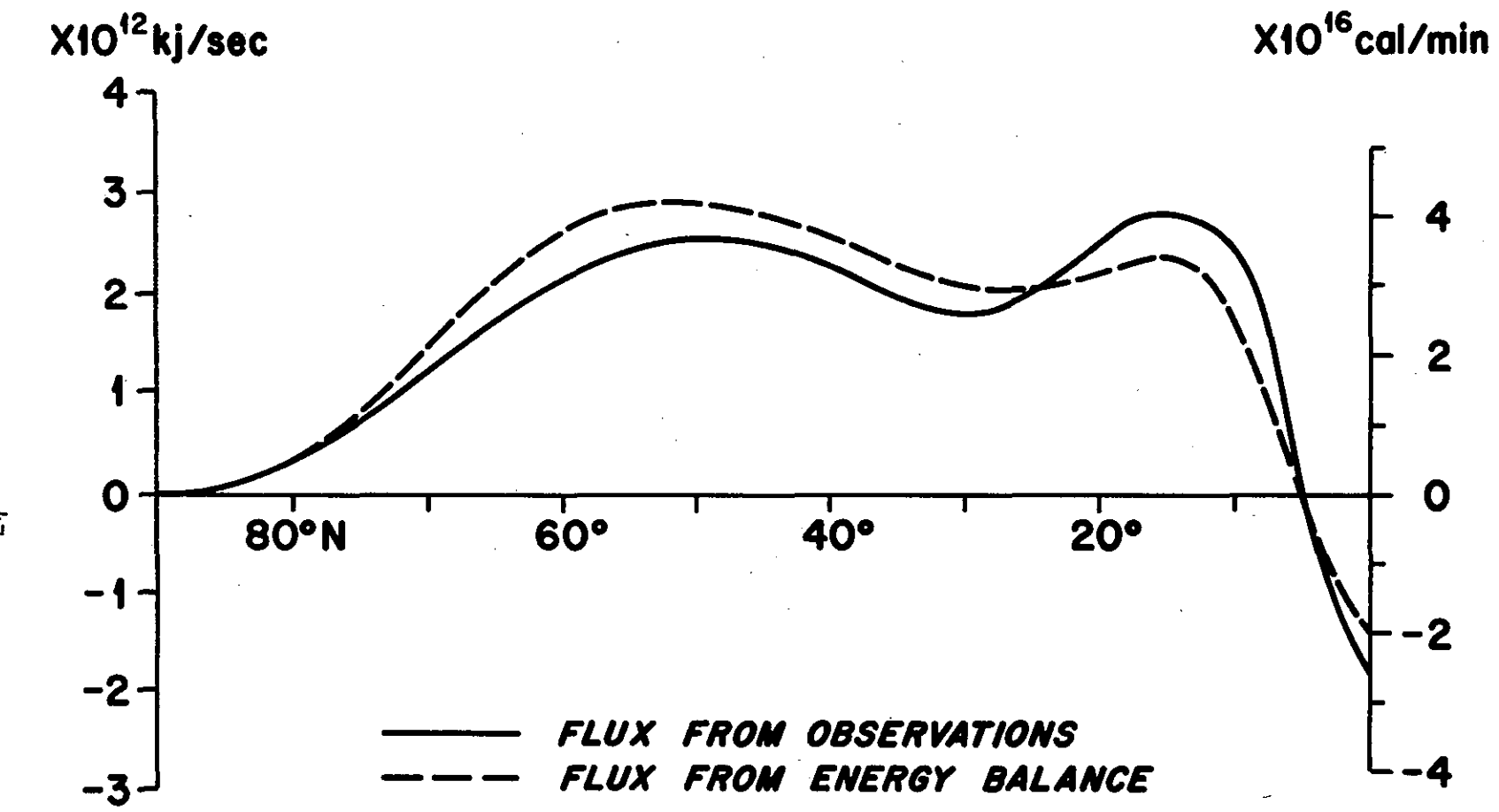

Figure 18.

Comparison between the annual northward energy flux in the Northern Hemisphere, as computed from aerological observations for three winter and three summer months, and the flux required for energy balance.

(After Palmen & Newton.)

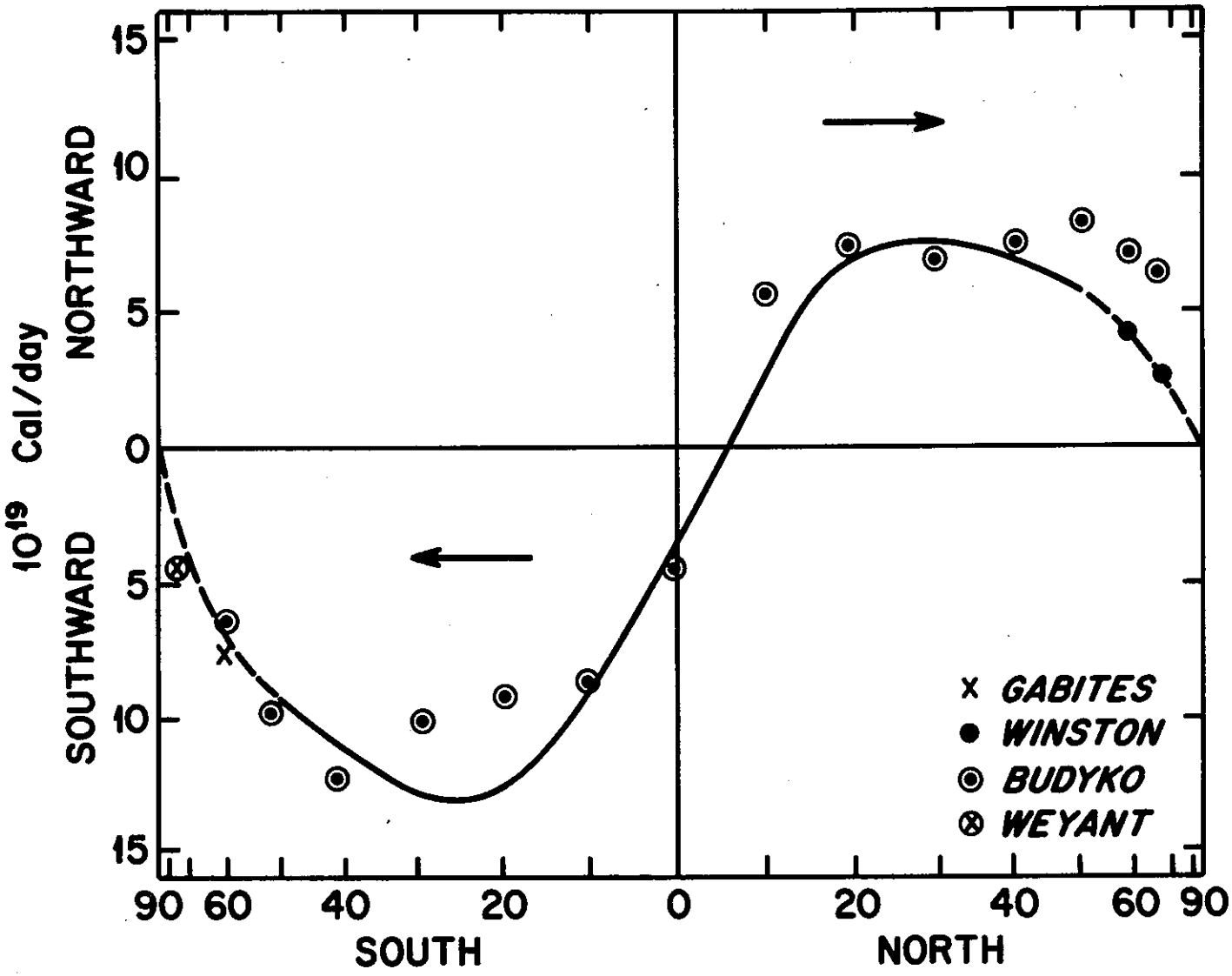

Figure 19. Mean annual poleward transport of heat energy as a function of latitude for the northern and southern hemispheres (in 10^{19} cal/day), computed from R_S obtained by satellite radiometers. (After Rasool and Prabhakara.)

good - 20 percent in the southern hemisphere and about 30 percent for the worst place in the northern hemisphere. Thus we may finally place some limits of confidence on the budget components. To summarize, the transport of atmospheric water vapor and realized energy have been checked out very closely. Although there is till some uncertainty in radiation balance, it is now reduced to about 10 - 20 percent or less and hence at worst, the deduced oceanic transports must be correct within 50 percent or so. Van der Haar at the University of Wisconsin is presently working on radiation balances from the NIMBUS satellite series with improved radiometry. This work, when completed, should reduce the uncertainties still further.

So far we have emphasized the tremendous importance of both evaporation and sensible heat exchange to the energetics and dynamics of sea and air. We have said nothing about momentum exchange or shearing stress, which is the main brake on the atmosphere and probably the most important way of driving the ocean currents. Momentum exchange can also be described by a transfer formula, namely

$$\tau_0 = \rho C_D u_a^2 \tag{12}$$

similar to the bulk aerodynamic equations for the transfer of heat and moisture which we wrote

$$Q_s = B_s c_p (T_o - T_a) u_a \tag{13}$$

$$Q_c = B_e L (q_o - q_a) u_a . \tag{14}$$

So far we have said little about the mechanisms and shorter than seasonal

time variation in sea-air transfer. Actually these mechanisms and time variations are mainly controlled by the atmosphere. The reason can be seen in the transfer formulas. The sea temperature changes are much smaller and much slower than the changes in air temperature. Furthermore, sea current speeds are very small compared to the windspeed and they change much more slowly. Hence exchange variations are governed by changes in air temperature, humidity and windspeed, that is to say, the air circulations regulate their own fuel supply and braking action.

The elements or mechanisms of exchange differ somewhat, depending upon whether you are equatorward or poleward of the subtropical ridges.

Figure 20 reviews the surface circulations in the atmosphere, emphasizing their strength and steadiness.

In the tropics, the main effectors of exchange are the strong and steady trade winds themselves. In some tests made in reference 1, we find that the summation of three-hourly exchanges over a month differs little from the exchange computed from the monthly average or resultant wind, whereas this is far from true in mid-latitudes. Nevertheless, there are weather disturbances on the easterlies, particularly pronounced in the equatorial zones, that do superimpose important variations upon exchange. Tropical disturbances fall into two main categories, namely weak disturbances and strong disturbances. Weak disturbances are summarized in table 2. They

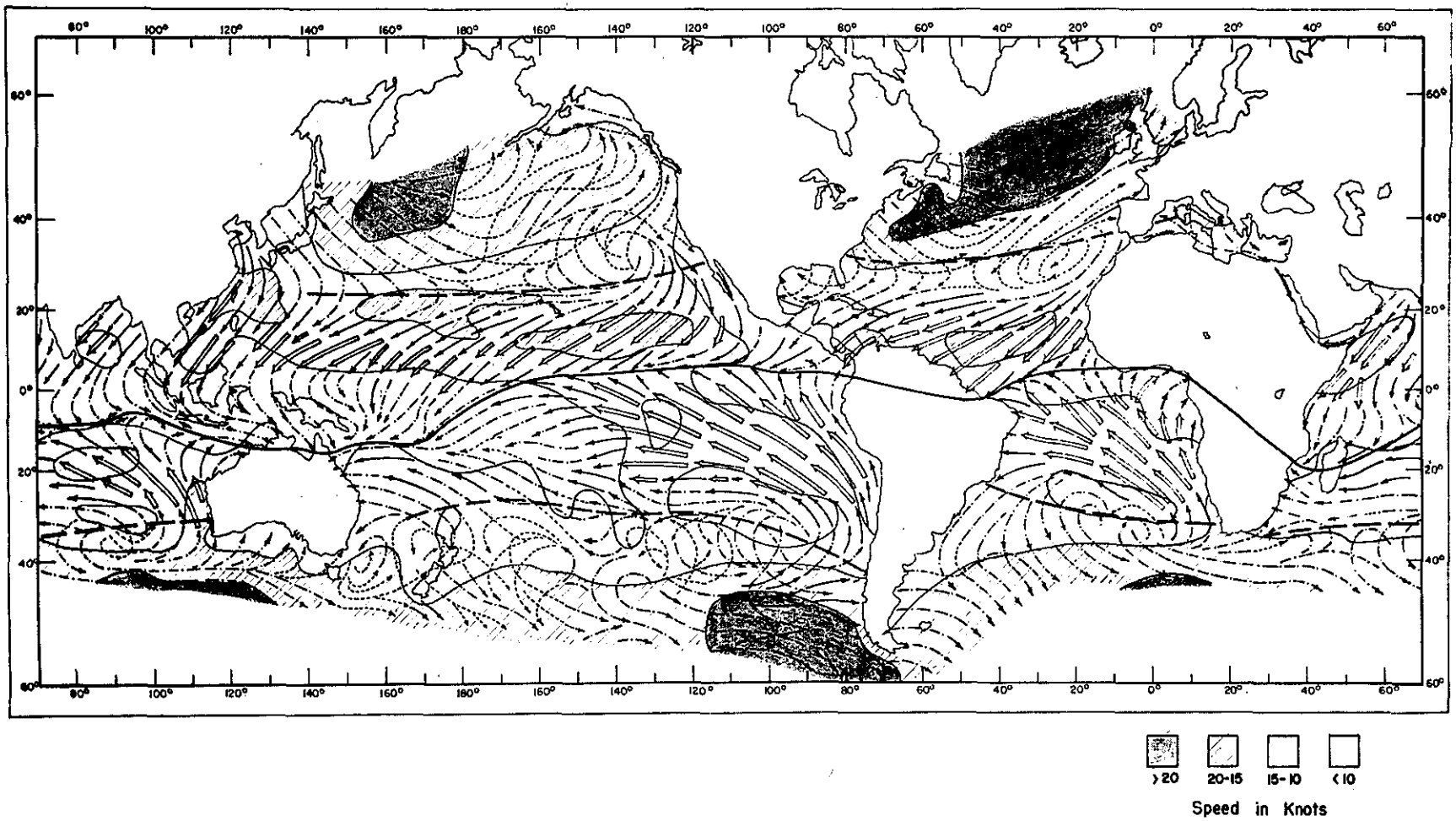

Figure 20. Prevailing surface winds over the oceans in winter. Direction and constancy in January. Direction lines based on dominant wind arrows computed for each 5° square, with direction constancy as follows: ⟹ 81% and over; → 61-80%; -·→ 41-60%; - → 25-40% of all winds from the quarter within which the line is a median solid line, mean position of equatorial trough. Dashed lines: mean positions of subtropical ridges (Atlas of Climatic Charts of the Oceans).

WEAK TROPICAL DISTURBANCES

TROPICAL DISTURBANCE: A DISCRETE RAIN SYSTEM GENERALLY 100-300 MILES IN DIAMETER, OF A NON-FRONTAL MIGRATORY CHARACTER.

TROPICAL WAVE: A TROPICAL DISTURBANCE WHICH IS REFLECTED IN THE CIRCULATION AS A TROUGH OR CYCLONIC CURVATURE MAXIMUM IN THE TRADE-WIND EASTERLIES.

TROPICAL DEPRESSION: A TROPICAL DISTURBANCE ASSOCIATED WITH CLOSED CIRCULATION IN THE LOWER TROPOSPHERE, MAXIMUM WINDS LESS THAN 34 KNOTS. THE WEAK STAGE OF A TROPICAL CYCLONE.

Table 2

contain convective bands and rainy areas but generally show windspeeds below normal (first two categories) or at most only slightly above normal (third category sometimes).

Figure 21 shows schematically a typical tropical depression of the western Atlantic. Cumulonimbus lines are associated with the asymptotes of convergence and may also be found to the eastward, or the rear of the wave trough. These clouds are performing the firebox function of the atmosphere, as we shall see later.

Table 3 shows the effect of these weak disturbances upon exchange. Note that we are comparing a disturbed period with both an unusually fair or suppressed period, as well as with the average of several normal periods. The first thing to notice is that the disturbed period wind speed is considerably less than that of the other periods and the sea-air temperature difference is much higher. The latter is mainly due to the air's being cooled from the evaporation of rain in the thunderstorm downdrafts. The air-sea specific humidity differences are nearly the same in all three regimes. As a result of these alterations in sea-air property difference, the latent heat exchange is weaker in the disturbances but the sensible heat exchange is more than doubled. Further research has shown that heightened sensible heat exchange is an invariable signature of a tropical disturbance.

In most regions and seasons of the tropics a weak disturbance passes about once every three days. The strong tropical disturbances,

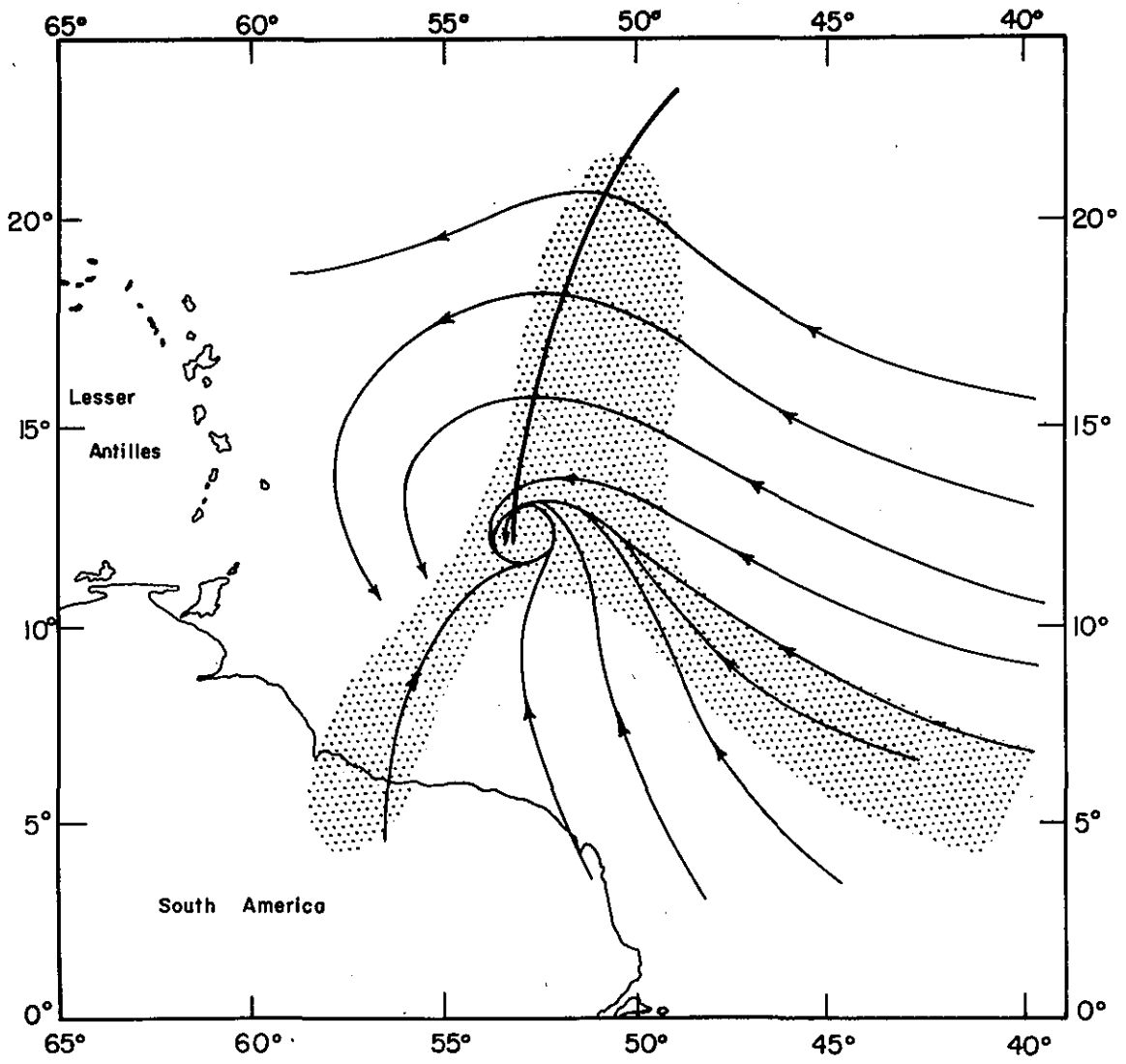

Figure 21. Schematic picture of a typical tropical depression of the western Atlantic in summer. This type of disturbance is sometimes called an "equatorial vortex." It commonly sets off a wave-like perturbation to the north of the vortex. Surface streamlines are light solid lines with arrowheads. Area of convergent low-level flow, with cloud bands and showers, shown by stipples.

Synoptic-Scale Exchange Fluctuations in the Equatorial Atlantic. From R.V. *Crawford* Cruise August 14–September 5, 1957

Period	$T_0 - T_a$, °C	$q_0 - q_a$, g/kg	u_a, m/sec	Q_s, cal/cm^2 day	Q_e, cal/cm^2 day
Disturbed: convergent and rainy (Period A) (96 obs.)	0.68	5.3	4.5	12.7	245
Very fair (Period B and C) (96 obs.)	0.06	4.9	6.0	1.5	302
"Normal"—all other (188 obs.)	0.22	5.4	5.6	5.1	310

Table 3

described in table 4 are much more rare. Only 10-15 named storms occur each year in the Atlantic and even a very hurricane-prone location rarely experiences more than one in five years. Therefore, although hurricane exchanges are extremely large, they probably do not contribute significantly to the global heat budget. Enhanced heat exchange is, however, absolutely essential to the very existence of the phenomenon hurricane. In Malkus and Riehl, 1960 [21], I have explained that this is so because the oceanic heat source, coupled with the latent heat release of the huge cumulus towers, creates the sharp pressure gradients that drive the furious winds.

Poleward of the subtropical ridges, the situation is entirely different. Like the weather, the main characteristic of sea-air interaction in these regions is fluctuation. A typical sample from the north Atlantic Weather Ship C is shown in figure 22. The graphs are time sequences of sensible and latent heat exchange Q_s and Q_e and shearing stress τ. These were computed from the ship's three-hourly observations using the Jacobs exchange formulas.

The figure shows that the exchange fluctuations are not random, but quite organized. The main organization is on a time scale of two to three days, with superposed mesoscale variations of a few hours. In the 22-day period shown, 4.35 cm (net) of sea water evaporated into the atmosphere at Ship C and 58 percent of the evaporation took place in just 1/6 of the three-hour intervals while 84 percent was achieved in 1/3 of them. The shearing

STRONG TROPICAL DISTURBANCES (NAMED)

TROPICAL STORM: A TROPICAL CYCLONE WITH CLOSED ISOBARS, DISTINCT ROTARY CIRCULATION, HIGHEST WIND SPEED 34-63 KNOTS.

HURRICANE: CLOSED ISOBARS, STRONG ROTARY CIRCULATION. WIND SPEED 64 KNOTS AND ABOVE. CLOUD WALL SURROUNDING OR PARTIALLY SURROUNDING RELATIVELY CALM CENTRAL "EYE" NEARLY ALWAYS PRESENT.

HURRICANE EXCHANGE (MODERATE STORM)

SENSIBLE HEAT Q_s 720 cal/cm^{2}day $\sim$ 50 TIMES NORMAL

LATENT HEAT Q_e 2420 cal/cm^{2}day $\sim$ 12-13 TIMES NORMAL

MOMENTUM EXCHANGE $\tau \sim$ 40 dynes/cm^2 $\sim$ 40-50 TIMES NORMAL

$$T_o - T_a \sim 2 \text{ TO } 3^\circ C$$

Table 4

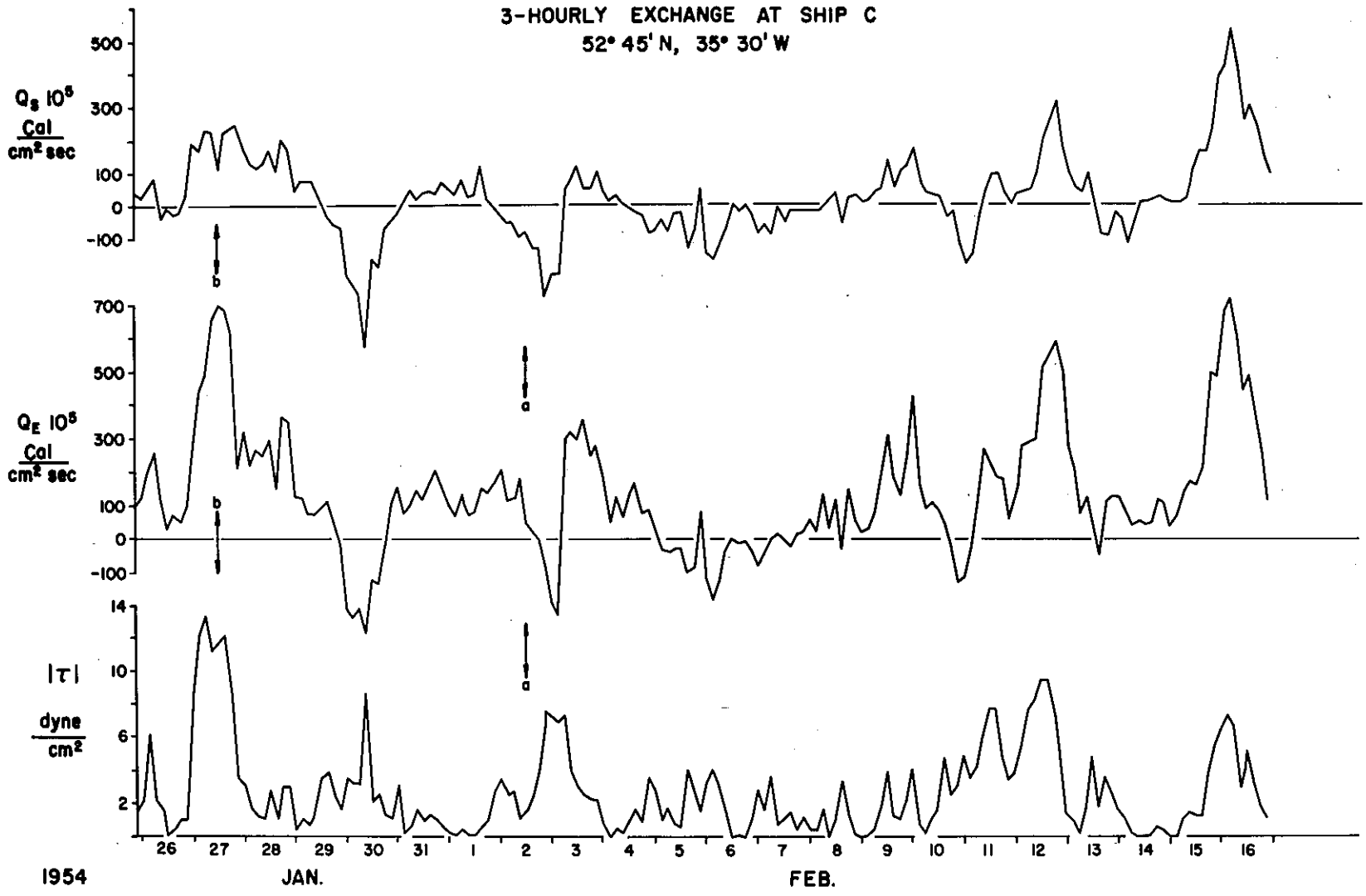

Figure 22. Three-hourly sea-air exchange at Weather Ship C for January 26 to February 16, 1954. These values were calculated from the transfer formulas.

stress imposed on the ocean and the sensible heat flux were similarly concentrated. The significant air-sea exchange in mid-latitudes is thus restricted almost entirely into synoptic scale disturbances. It requires little daring to identify these with the traveling frontal cyclones which march across the weather map of these regions. This exchange pattern contrasts with that of the tropics, where we saw that the major energy exchange is effected by the strong and steady trade winds.

In this diagram, the shape of the exchange curves permits deductions about the weather pattern and its stage of development. In the sequence February 2-4, a surge in stress (wind) coincided with negative heat flux abruptly changing to positive just before midnight on February 2. Then the evaporation and heating of the air persisted for about a day after the strong winds diminished. These features suggest a simple cold front or young warm-sector cyclone wave, with warm air flowing northward first, followed by a sudden cold outburst over the sea. Figure 23 shows that this was indeed the chain of events. A front is as much an "exchange discontinuity" as it is an airmass transition.

A deeper, older and more occluded cyclone is suggested by the exchange pattern for January 27 - 29. The greater deepness is indicated by the stronger stress and the age by the lack of surface warm air and advection (negative heat exchange) ahead of the storm. However, the skew-shaped Q_s and Q_e curves, with positive heat flux and evaporation lasting beyond the

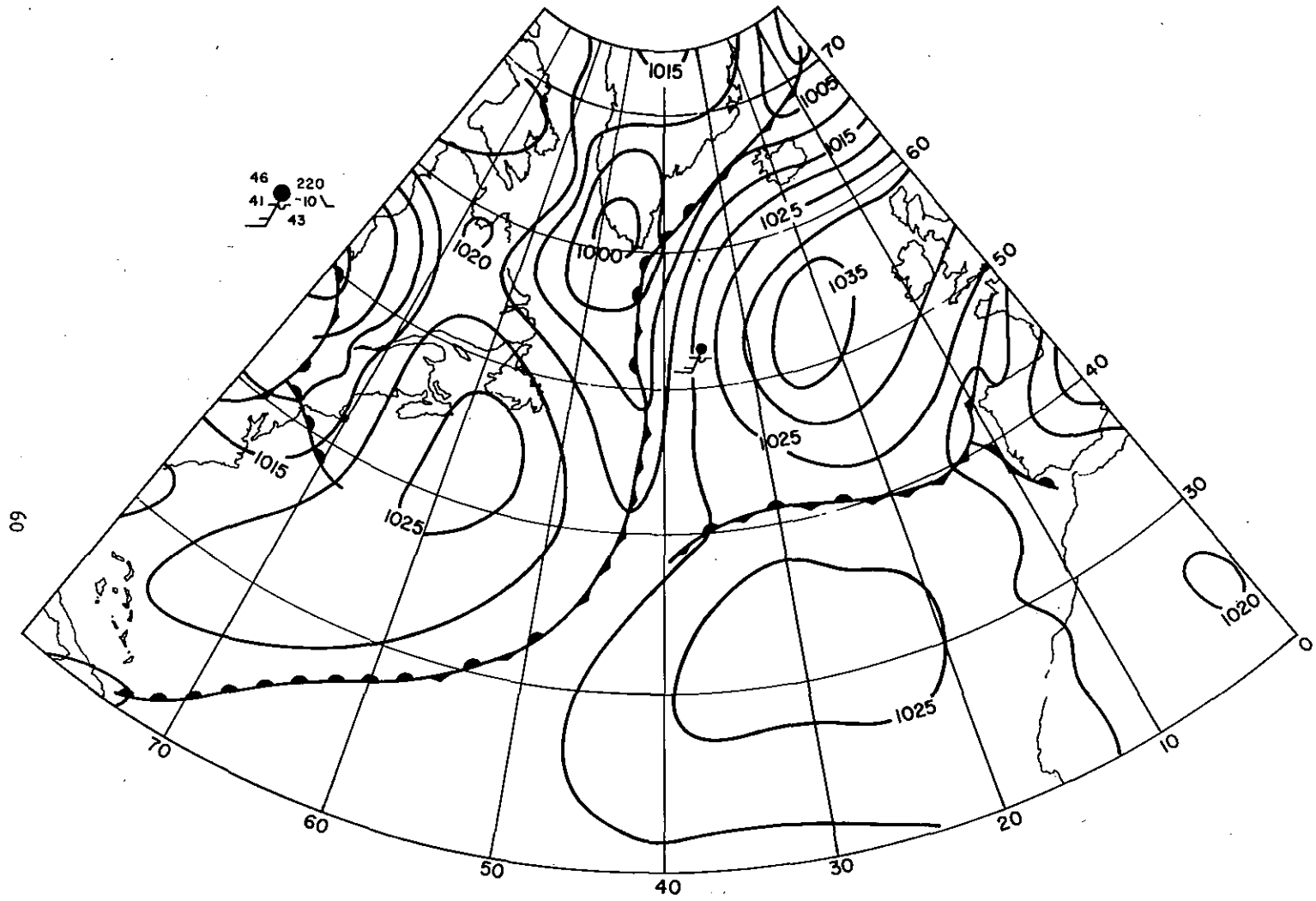

SURFACE CHART
FEBRUARY 2, 1954
1230 G. M. T.

Figure 23. Surface weather map for February 2, 1954. Standard symbolism.

wind maximum, again suggests a cold air outbreak behind the system. Figure 24 bears out these deductions.

The deepening cyclone is an outstanding feature of the mid-latitude atmosphere. It both characterizes the instability of the westerly winds and releases the energy that maintains their motion. We just saw that they also control sea-air interaction over the extra-tropical oceans.

Models of the deepening wave cyclone were evolved early in the century by the great Norwegian meteorologists to describe and explain physically the three-dimensional distributions of wind, cloud and weather patterns as a "typical" frontal system goes through its life history. It is thus fitting that successors of these great Norwegians at Chicago, namely Pettersen, Bradbury and Pedersen, have incorporated the sea-air interaction distribution into the cyclone model so that exchange becomes quantitatively and coherently related to the developing disturbances and its processes. I have summarized their work in reference 22.

Perhaps even more exciting, a possibility has concomitantly emerged of an important feedback of sea-air interaction upon the growth of cyclones themselves, which will be mentioned just briefly later.

Pettersen, Bradbury and Pedersen constructed a composite oceanic cyclone in each stage of development and documented the distribution of exchange in relation to its winds and weather pattern. The synoptic situations were chosen to be typical of the various stages of cyclone development,

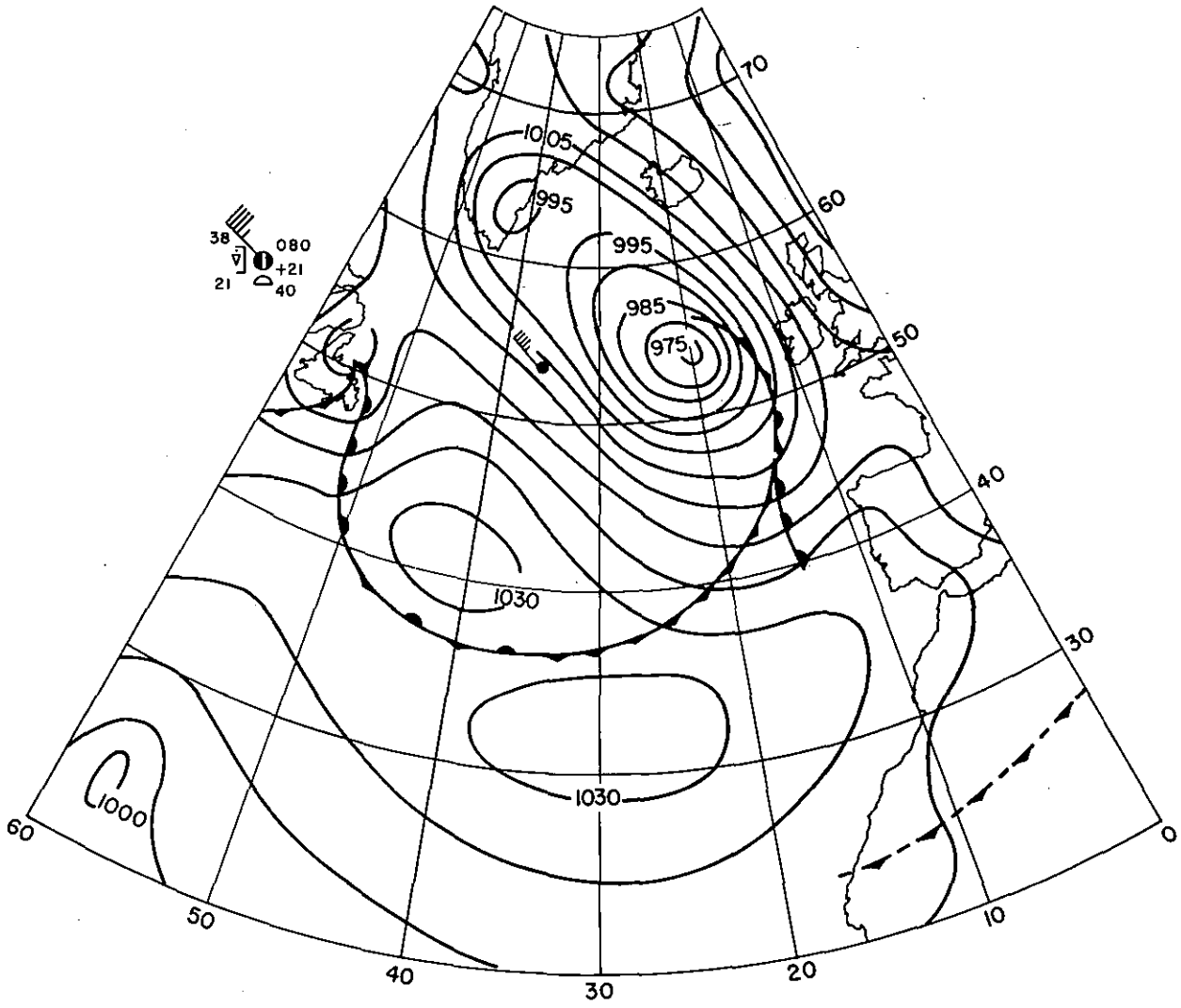

SURFACE CHART
JANUARY 27, 1954
1230 G. M. T.

Figure 24. Surface weather map for January 27, 1954. Standard symbolism.

namely the nascent cyclone wave, the warm sector cyclone, the partly cloudy occluded cyclone, the full occlusion and the frontless cold core low. In addition arctic outbreaks were similarly investigated.

Fifty-one individual cases during a single winter were selected for compositing. In each, analyses were drawn for the pertinent variables. The sea-air transfer was computed from these analyses with the Jacobs formulas at grid points oriented with respect to the cyclone center. These were then transferred to a master grid constructed for each of the five stages of development. As an example, figure 25 shows the results for the open wave stage.

Charts A show the sequence of pressure distribution and frontal structure at sea level for the developing cyclone. The young wave is generously supplied with tropical air dragged north from the trade-wind belt, which is perturbed in tune with the wave disturbance. Charts B show the rate of kinetic energy dissipation at the ocean-atmosphere interface, or the surface shearing stress times the windspeed. The maximum stress is found in the warm sector of the open wave, while it increases and moves to the cold air in the rear as the storm develops. Note that the kinetic energy dissipation is nearly two orders of magnitude less that the heat exchanges.

The patterns of energy exchange (charts C and D) exhibit remarkable peaks associated with the cold air. These peaks are developed by and locked into the cyclone patterns as it progresses. Typical maxima of the

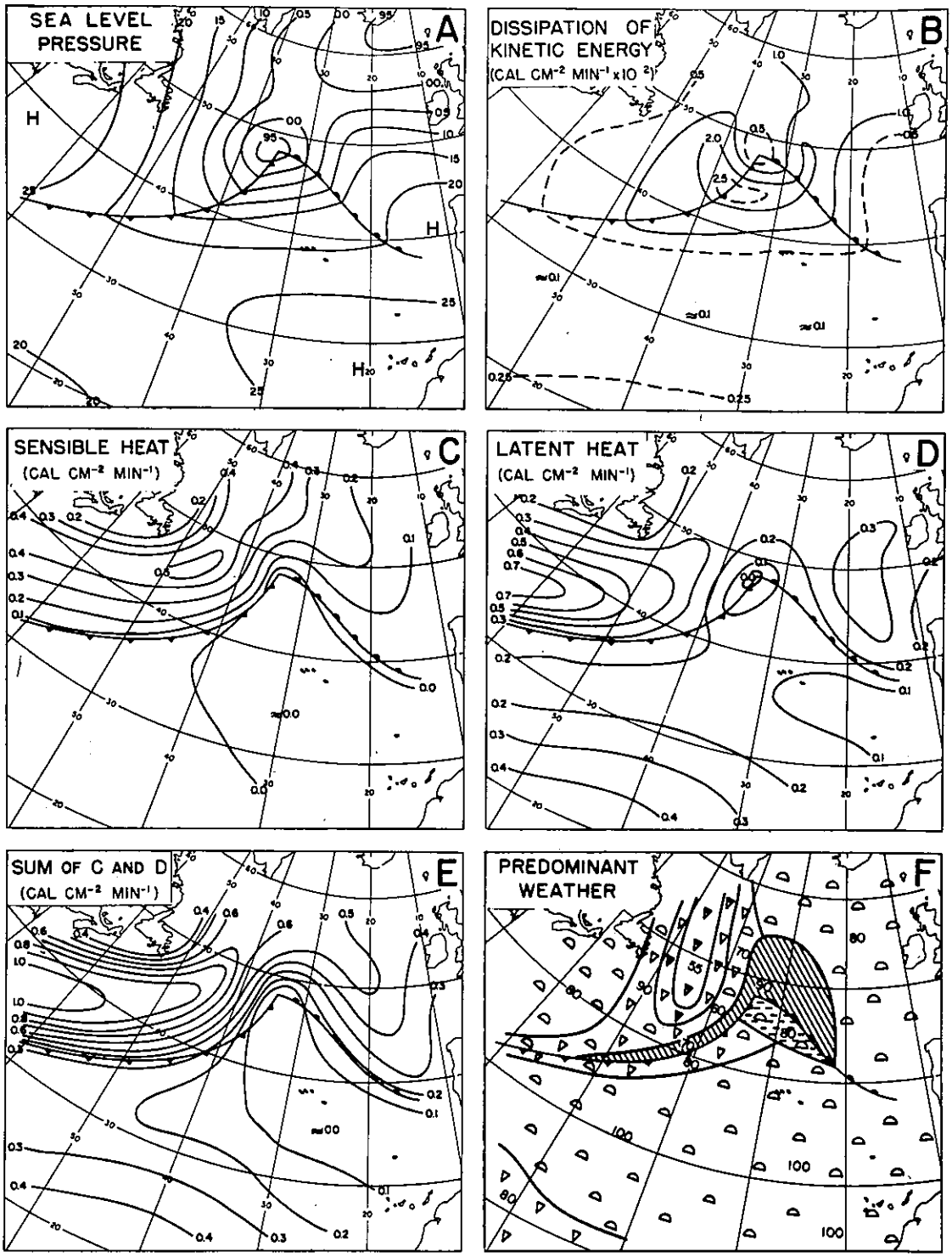

Figure 25. Models of warm sector cyclones and their sea-air interaction patterns. (After Petterssen, Bradbury and Pedersen.)

sensible flux were about 1 cal/cm^2 min or 1440 cal cm^{-2} per day (twice as big as the hurricane) and the maximum isopleths of latent heat were about 1.4 times this or 80 percent that of the hurricane. Still higher peaks were found in single cases. Q_s and Q_e are highly correlated, as can be seen by comparing charts C and D with charts E which show their sum. The net radiative fluxes from sea to air were computed to be an order of magnitude smaller.

Standing above any doubts about Jacobs formulas, the main feature of the cyclone exchange is its large size coupled uniquely to the moving system. In the extreme case, the ocean heat loss to the atmosphere amounted to 2.5 cal/cm^2 min. This is about 20 times the average absorption of shortwave radiation at latitude 50° N in winter and more than 40 times the net radiation balance that the sea surface has in the radiation bank! Now the usefulness of storage and heat flux convergence becomes very vivid indeed. Consequences to the ocean of these huge spasmodic heat losses have not yet been investigated in any case studies.

The most remarkable feature, however, of this series of diagrams is the comparison of the heating patterns with the weather patterns in charts F. The latter draw upon the standard weather code to characterize the dominant sky type as: strong convective (heavy shower symbols); moderate convective (plain shower symbols); weak convective (fine weather cumulus symbols); fog or stratus (dashed); and frontal precipitation (hatched). The numbers between the weather symbols in charts F signify the probability

of occurrence of that weather type. Most noteworthy is the relationship between charts E and F. The axes of the heavy convective areas are oriented at right angles to the heating pattern. A band of moderate to heavy convective activity is present to the northwest of the apex of the wave where the rate of heating is moderate. The convective activity decreases to moderate off Newfoundland where the rate of heating is quite large. Still farther to the west only flat cumulus develop although the heat inputs by exchange reach a max in this area. These features are maintained througout the life history of the cyclone, as we see in figure 26 which shows the occluding stage.

Comparison of charts F, E and A at all stages shows that heating from the underlying sea surface always results in some convective activity. However, unless the air takes part in a cyclonic circulation, moderate and heavy precipitating convection will not take place even if the surface heating is very intense. This illustrates the close coupling between sea-air interaction, cumulus convection and the vorticity of the air circulation. When I compared the foregoing with a non-developing case, the cold outbreak took place in anticyclonic flow so that no penetrative convection was set off. In the explosive deepening case, the cold outbreak occurred in cyclonic flow, with deep convection to the tropopause. I was able to show that the convection, probably via induced convergence, added a source of cyclonic vorticity in the vorticity equation, thus accounting for the rapid deepening that vorticity advection alone miserably failed to predict.

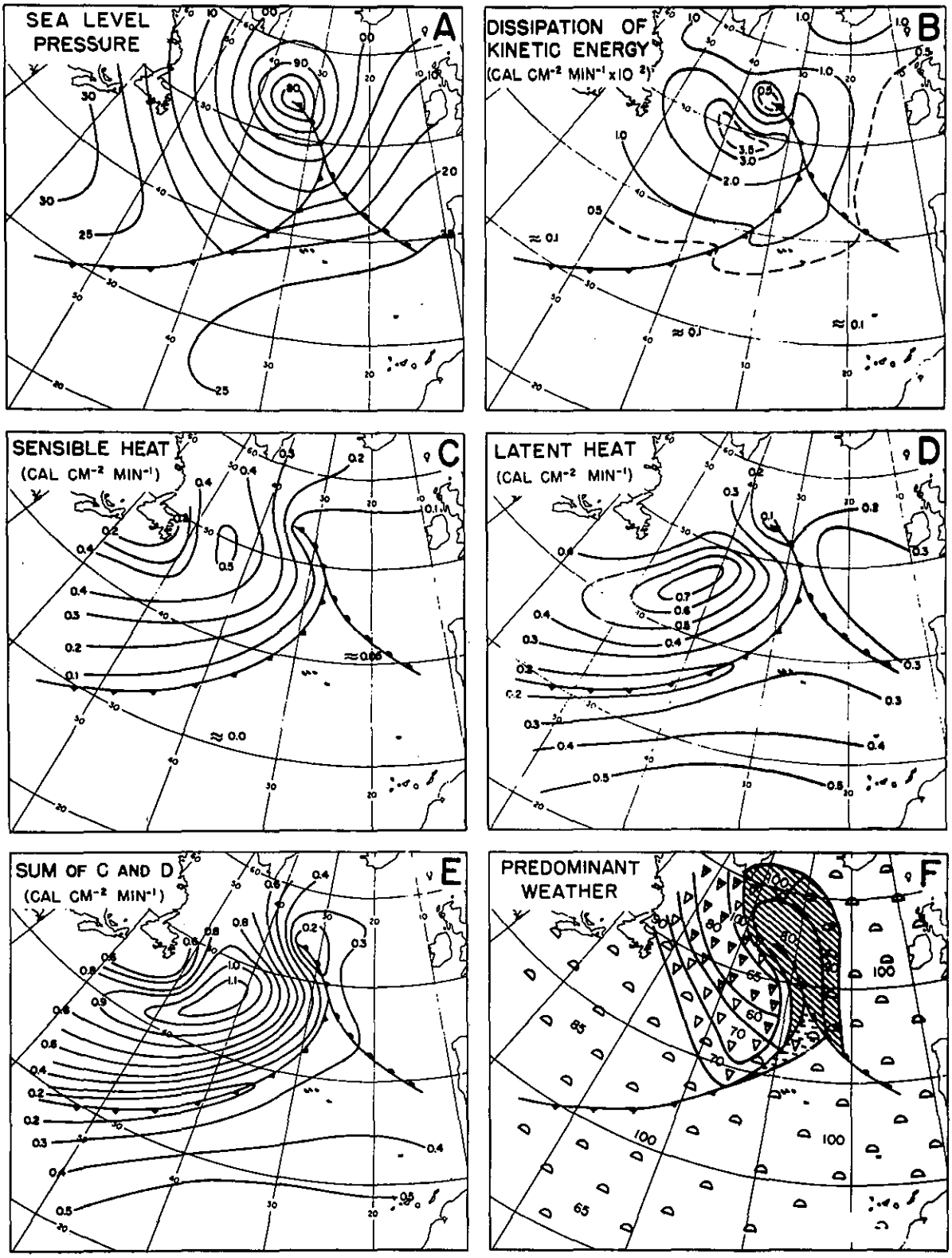

Figure 26. Models of occluded cyclones and their sea-air interaction patterns. (After Petterssen, Bradbury and Pedersen.)

Once again we glimpse the importance of convective clouds in coupling with sea-air exchange to utilize and release the energy, thus maintaining and developing important air circulation systems which, in turn, feed back to alter the exchange. Cumulus clouds are a very important linkage in exchange processes and their effects. In the next two sections we will examine the operation of cumulus clouds and look somewhat more closely into how they interact with the large scale wind systems.

3. CLOUD DYNAMICS, PHYSICS AND MODIFICATION EXPERIMENTS

The remainder of this report concerns clouds, particularly cumulus clouds, their role in large scale and boundary layer processes and their organization into groups and patterns. Modification experiments are introduced here, not mainly for the intrinsic interest or potential practical value, but because they have served, in the United States, as very powerful catalysts in advancing our understanding and modelling of cumuli. We will view them here in that context.

Why are clouds so important that we should be devoting so much attention to them? Actually, clouds are one of the most important of all geophysical phenomena. Their first obvious value is the life-sustaining rainfall which probably makes the earth unique among the planets. Clouds also regulate incoming radiation from the sun and that lost by the earth to space, thus affecting the temperature and temperature gradients on the earth and in the atmosphere. We discussed briefly this role played by clouds in section 1. Less obviously, research has shown that cumulus-type clouds are the firebox of all severe storms, such as the hurricane, tornado, hailstorm and thunderstorm. These towering clouds also play a critical role in the development of oceanic cyclones in mid-latitudes and in driving the large-scale trade winds which cover the earth on both sides of the equator. As we saw in section II,

Corrected page 70 for ERL WMPO-8

the equatorial regions themselves are the firebox of the atmosphere as a whole, releasing the heat that balances the radiation losses and drives the large-scale planetary wind systems. In the equatorial zones themselves, clouds are the mechanism by which the heat, which is picked up in the air-sea boundary layer, is made available to the atmosphere. As we will see, only a few thousand large clouds existing at one time are necessary to carry out the firebox function. These large clouds are clustered in bands and patterns in tropical disturbances that we shall see later in pictures. Furthermore, thunderstorms probably maintain the electrical potential difference between the ionosphere and the earth's surface. Last but by no means least, cumulus clouds are a prototype of convection, which is one of the key processes at work in most planetary boundary layers. It is also a primary process by which heat energy is converted into motion in geophysical systems. Convection occurs on many scales, in many settings ranging from the earth's core to the solar atmosphere. Cumulus clouds are an accessible and relatively reproducible manifestation of the convective process. They are also one of the few geophysical phenomena which have been successfully subjected to controlled field experiments. These experiments will be a main focus of this section.

Cloud physics and cloud dynamics were essentially born since World War II and have reached adolescence in the intervening 25 years. They are just now, rather belatedly taking serious steps toward being combined into a single discipline. A major impetus toward bringing these disciplines

together are the modification experiments to be described. To make meaningful modification experiments on clouds we must have models capable of predicting both their modified and unmodified structure and behavior. We found in the process of making numerical models to do this that we had to model both the dynamics and the physics of the clouds and the interaction of these two aspects.

By cloud physics, we mean the microphysics of the droplet and ice crystal growth, or the physics of the structure and growth of the cloud particles themselves.

Table 5 shows a list of some of the key problems in cloud physics. We will come back to the first five of these briefly in the course of discussing our numerical cloud model. Up until very recently, most cloud physicists have been trained in classical experimental physics, some in solid state and crystal physics, and their exposure to meteorology and the turbulent rotating atmosphere outside the laboratory has often been slight.

Cloud dynamics, on the other hand, deals with the relation between forces and motions in the clouds, with the purpose of predicting and understanding the structure and life cycle of the updrafts and downdrafts. Cloud dynamicists have mainly had their schooling as meteorologists, with a good feeling for air circulations, but with often inadequate knowledge of advanced physical theory or laboratory techniques. The recent merging of the two disciplines is well illustrated in the Experimental Meteorology

KEY PROBLEM AREAS IN CLOUD PHYSICS

1. PRECIPITATION GROWTH AND FALLOUT

2. CONDENSATION NUCLEI AND CONDENSATION GROWTH OF CLOUD DROPS — DIFFERENCE BETWEEN MARINE AND CONTINENTAL CLOUDS

3. COALESCENCE GROWTH OF DROPLETS — CLOUD SIZE (5–20μ) TO PRECIPITATION SIZE (500μ–9mm)

4. FREEZING NUCLEI AND ICE NUCLEATION

5. ICE GROWTH AND ICE CRYSTAL HABITS. GRAUPEL AND HAIL

6. CLOUD ELECTRIFICATION, LIGHTNING

Table 5

Corrected page 73 for ERL WMPO-8

Laboratory in NOAA where we do not just have cloud dynamicists and physicists working closely together but we actually have several individuals who are advancing both areas of study jointly.

Because of their importance, we will confine our limited time here to cumulus clouds, as depicted in figure 27. Here we see a hierarchy of three important sizes of tropical cumuli. Naturally, they come in all gradations of sizes, but we have just picked out three here for convenience.

Aircraft and laboratory studies have shown that these cloud towers are commonly like a growing plume or jet, with a vortex-like circulation near the top. The energy driving the motions comes from the condensation of water vapor into liquid cloud drops. The cloud drops grow to 5-20μ by condensation and have negligible fall speeds relative to the upcurrents, which are 2-3 m/sec and up to 20-30 m/sec in the giant ones. There are normally between 20-2000 cloud drops per cm^3, depending on the number of condensation nuclei present. The release of the latent heat of condensation makes the cloudy air warmer and hence less dense than the clear air surroundings and therefore buoyant. The buoyancy sustains and maintains the updraft, thus keeping the condensation process alive.

Like people, cumulus clouds have a life cycle. They are born, they grow up and eventually age and die, but unlike people, the fatter they are the longer and more vigorously they live and the taller they grow. Small trade cumuli, like the ones on the right, may enjoy an active lifetime of about ten minutes, while the medium ones thrive on the order of a half hour at most.

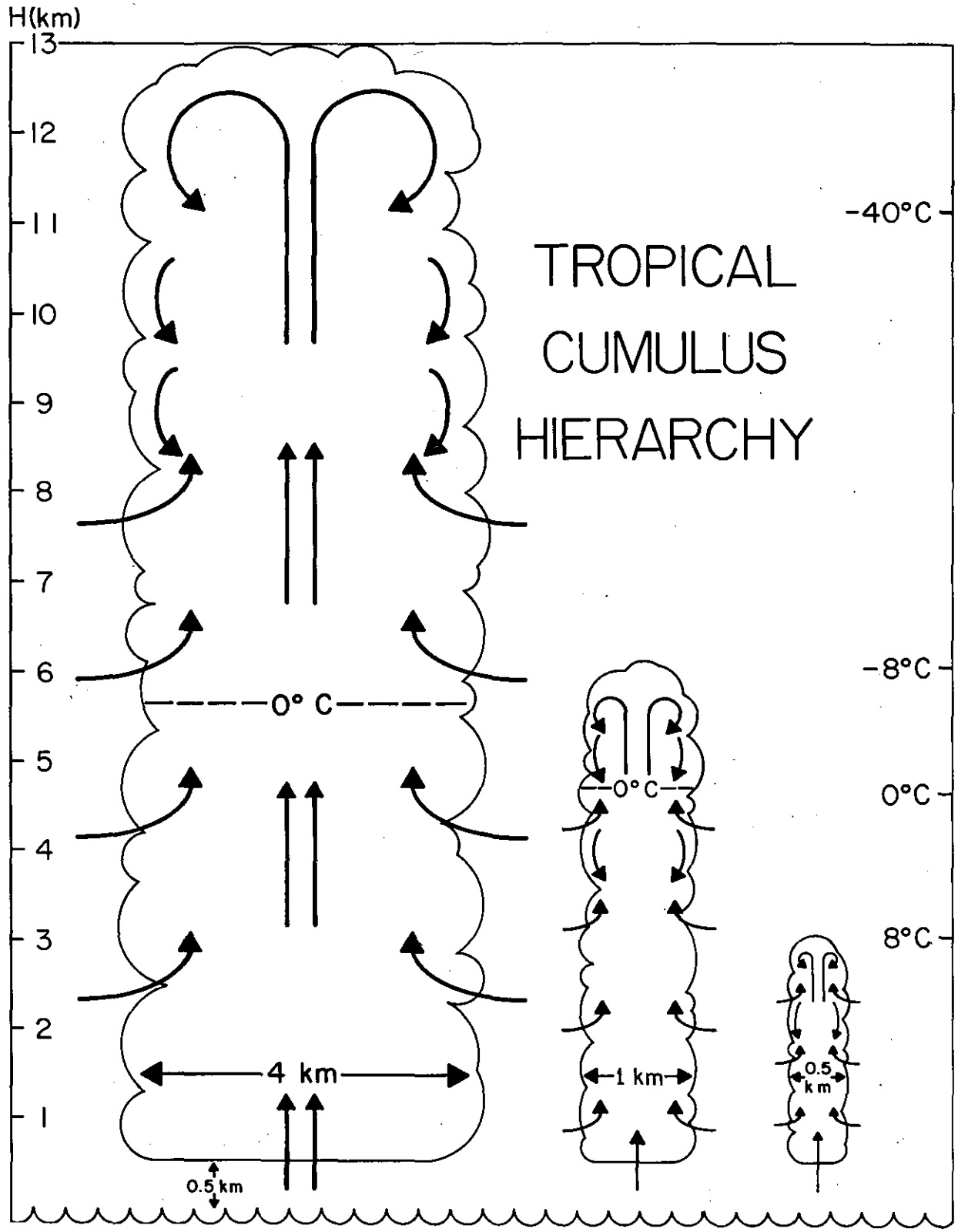

Figure 27. Schematic hierarchy of tropical cumulus clouds.

A giant cumulonimbus of a hurricane or squall line may be active for more than an hour. But at all times, natural existence is a desperate struggle for a cumulus cloud. Its life is a precarious balance between the forces of growth and those of destruction. We have just described the buoyant growth forces. Now what are the destructive forces and how do they work?

The science of cumulus dynamics began in 1946 with the discovery of these resistive forces and their documentation by measurement. Prior to 1946, meteorologists had been largely unaware of interactions between clouds and their surroundings. Ignoring them, they had derived very beautiful stability criteria (called the "parcel theory") for cloud growth which depended only on the vertical temperature gradient or lapse rate of the surroundings. The increased interest in tropical meteorology stimulated by World War II revealed that there was something drastically amiss with these criteria.

Figure 28 illustrates the problem in terms of the cloud hierarchy shown in figure 27. According to the parcel theory, all tropical clouds should penetrate into the stratosphere, or to that height (above 100 mb) where "negative area" becomes equal to positive on a thermodynamic diagram. But only the fat giant clouds actually penetrate to the tropopause and these top out at the top of the positive area where, theoretically, the ascent rate should be largest. This indicates some kind of drag, or friction force in near balance with the buoyancy. An even more obvious deficiency of parcel theory is that most tropical clouds terminate between 3-6 km, at the very levels where the

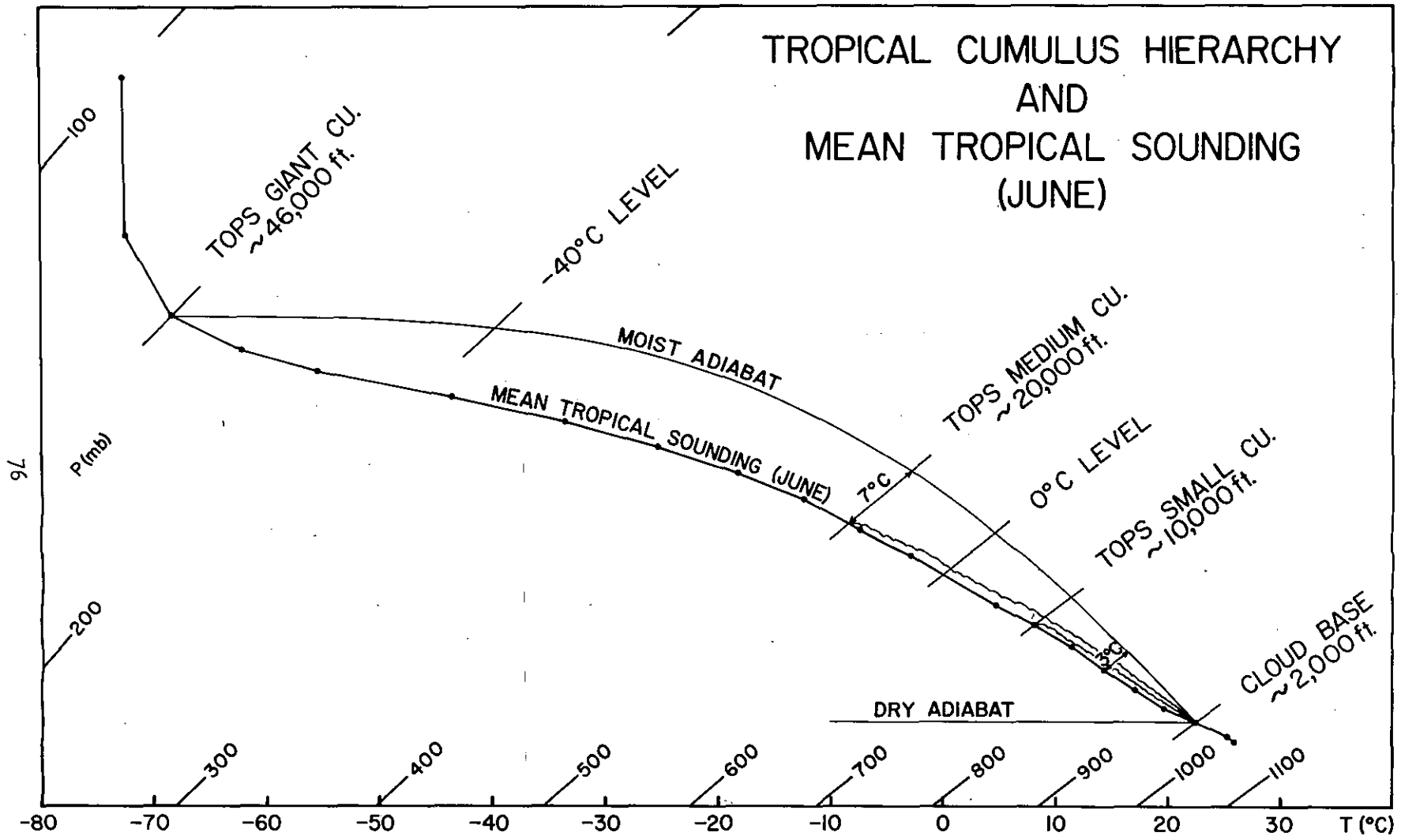

Figure 28. Tephigram illustrating temperatures inside clouds of tropical cumulus hierarchy in comparison with mean tropical sounding. The abscissa is temperature in °C; the slanted ticks are pressures in mb.

parcel buoyancy is greatest! The advent of the research aircraft provided the solution to this paradox. For the small and medium clouds, the in-cloud temperatures were closer to that of the clear air than to the wet-adiabatic ascent, so that a typical middle-sized cloud had temperature excesses of only about 0.5 - 1.0° C. Similarly, cloud liquid water contents ran only about 1-3 gm/m^3 instead of the 8-10 gm/m^3 predicted by the parcel theory. In 1946 the brilliant oceanographer, Henry Stommel, postulated that the clouds were entraining or mixing in the outside air from their drier surroundings. Using the newly available aircraft soundings of temperature and humidity made inside and outside the clouds, Stommel devised a mathematical and a graphical method of computing the amount or rate of entrainment. The concept of entrainment virtually revolutionized tropical meteorology. Furthermore, an entrainment calculation is a basic ingredient of the one-dimensional cumulus model presented soon. Hence, the graphical method of computing entrainment is illustrated in figure 29. The cloud is envisaged as a rising jet of air with internal temperature T and specific humidity q which are homogenous or well-mixed across its diameter. The clear air and cloud soundings are plotted on T, q graph with with same scale in T in ° C and in q in gm/kgm. The continuous cloud process is broken down into three finite difference steps. The first is a dry adiabatic cooling at 1° C per 100 through a rise in elevation Δz. Then a "mixing line" is drawn to the environment point at $z = \Delta z$. An amount of cloud mass M is mixed with an amount of outside mass dM to bring the mixture

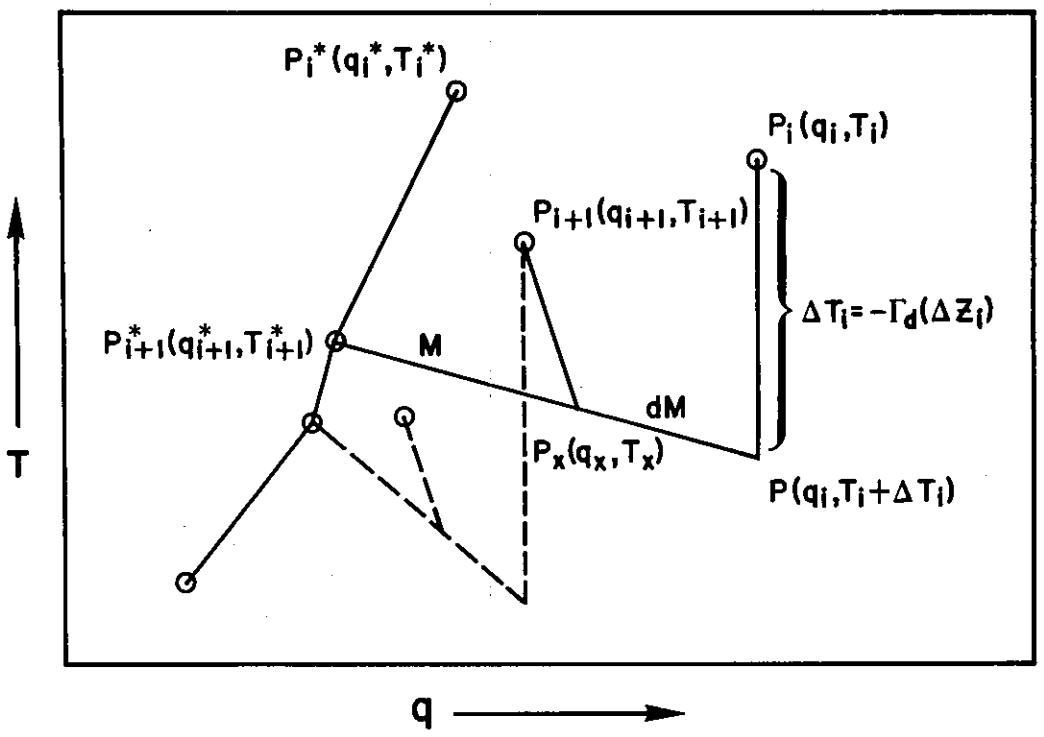

$$\frac{dT}{dq} = -\frac{L}{c_p} = -2.5$$

When T in °C q in gms/kgm

$$\text{Entrainment} = R = \frac{1}{M}\frac{dM}{dz}$$

Figure 29. Schematic diagram illustrating entrainment calculation by Stommel's method. Abscissa is specific humidity q in gm/gm. Ordinate is temperature T in °C. Circles on left denote environment; circles on right relate to cloud. Subscript i stands for lower level, 1+i next higher level. Details in text.

to point P_x, and then condensation occurs along the slanting line to reach the cloud point P_{i+1}. In practice we have the point P_{i+1} from the sounding but not the point P_x, so that P_x is found by constructing the "condensation line" through P_{i+1}. Where this line crosses the mixing line separates dM and M, which are measured with a ruler to determine their ratio dM/M. The amount of water condensed in the ascent Δ z can be found by substracting q_{i+1} from q_x. If none falls out as precipitation, accumulating the Δ q's should give the cloud water content. The rate of entrainment R is defined as 1/M dM/dz. For example, for small trade cumulus clouds, calculations from observations show that 1/M dM/dz is about 10^{-5} per cm. This means that it is 1 in 10^5 cm or 1 km, or that in 1 kilometer's rise the cloud entrains in just about as much air from outside as it originally contained. This is quite a bit of dilution. The details of entrainment theory and its applications to cloud observations are discussed in references 1 and 2.

Following the discovery of entrainment in 1946, the Woods Hole group investigated the entraining cumulus in a shearing wind field. The highlights of this work are shown in figure 30 and the details are discussed in references 2-4. We were able to show, with both theory and aircraft observations that the cloud entrains mainly on its upshear side and it sheds moist air or "detrains" on its downshear side. Thus the cloud imparts its heat, moisture and momentum to the surroundings, a vitally important exchange that had not been considered before 1946.

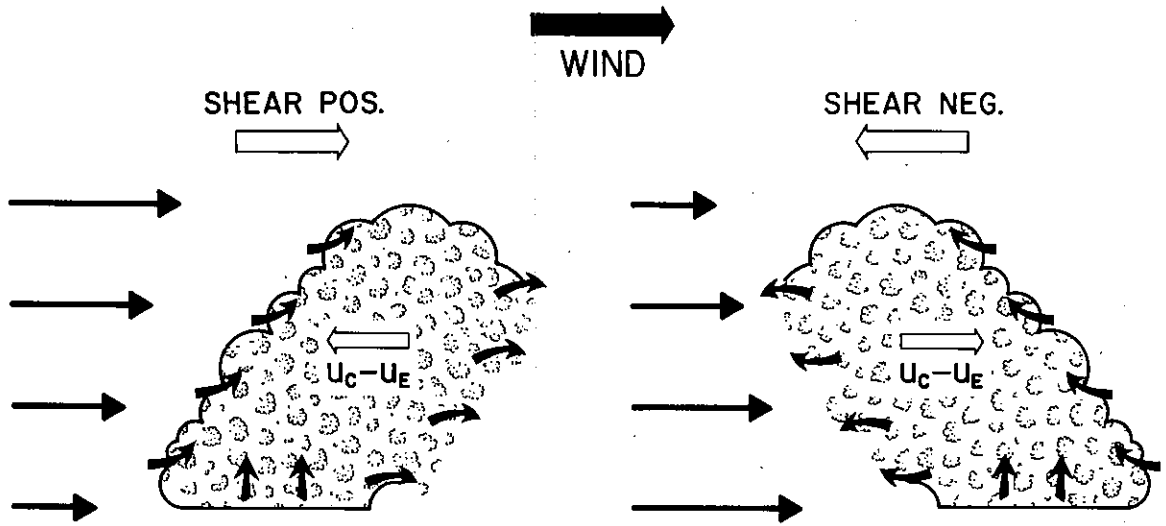

$$d(Mu_c) = u_E dM_i - u_c dM_o \qquad dM = dM_i - dM_o$$

$$\frac{du_c}{dz} = (u_c - u_E)\frac{1}{M}\frac{dM_i}{dz} \quad \text{if} \quad u_E = u_{Eo} + bz \quad \therefore \quad \boxed{u_c - u_E = \frac{b}{R}(e^{-Rz} - 1)} \quad \text{Neg.}$$

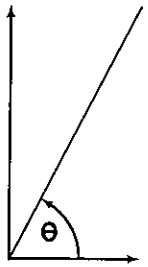

$$\tan\theta = \frac{W}{u_c - u_{Eo}} = \frac{W}{b\left[z + \frac{1}{R}(e^{-Rz} - 1)\right]}$$

$$R = \frac{1}{M}\frac{dM_i}{dz}$$

Figure 30. Illustration of how cumulus clouds lean with the vertical shear of horizontal wind. On the left the cloud velocity U_c is less than the windspeed U_E, while the reverse is true of the cloud on the right.

It is probably not an exaggeration to say that the discovery and documentation of entrainment and detrainment revolutionized meteorology because now it was possible to recognize the role played by clouds in large-scale weather processes. In the 1950's, paper after paper began to come out on the role of cumuli in forming and maintaining hurricanes, on their role in driving the trade winds, on their role in marine cyclogenesis and on their role in maintaining the planetary wind systems. Some of these papers appear in the references as numbers 27-30. Some of these important effects of tropical clouds will be discussed in the next section. Today we have advanced to the point where these effects of clouds are introduced into the computer models predicting the growth of hurricanes and, still crudely, into the large-scale forecast models in daily use. In fact, the effects of clouds are now believed so critical that the main focus of the 1974 GATE experiment of the Global Atmospheric Research program will be on tropical cloud clusters, to try to find out how to better simulate cloud processes in numerical prediction models.

After the discovery of entrainment, one of the next major problems was to specify its functional dependence. This problem is by no means completely or satisfactorily solved today. Great progress on it was made from laboratory experiments in the 1950's [27, 28, 29, 30]. In these it was shown that entrainment depends inversely on the horizontal dimension of the convective element. This important dependence was verified to first order by various types of measurements on real clouds. Now we can understand much

better the cloud hierarchy shown in figure 28. Since the largest cloud shown is eight times the diameter of the smallest, it will require eight km instead of one to be diluted with an equal amount of mass as it originally contained. Its core is protected from entrainment by the much greater amount of volume per unit surface area, and hence it can rise through essentially the whole troposphere before losing its buoyancy. The postulation of the inverse dependence of entrainment upon diameter enabled the first crude progress we were able to make toward numerical cumulus models. This class of model is one-dimensional and based on the resemblance between a cumulus cloud and an unsteady plume or jet. We will discuss these models in connection with modification experiments. Actually there are two classes of numerical cumulus models that people have been working on. The first class I call "entity" models [32]. A cumulus is likened to a jet or a plume, a buoyant bubble or some other physical entity. Then semi-empirical laws derived from measurements or theories about these entities are introduced as a key part of the model. A typical example is described shortly; in it, the inverse radius entrainment law forms a key part. The other class of model I call the "field of motion" models. The hydrodynamic equations of motion are set up in finite difference form and are integrated in a series of finite time steps starting from a resting unstably stratified fluid. The size and shape of the initial perturbation, which is either a small temperature or humidity elevation, has to be assumed. The next figures illustrates this type of model. Table 6 illustrates the equations used

Table 6

"MOTION FIELD" CONVECTION MODELS

DRY MODEL MALKUS — WITT (1959)

WET MODEL MURRAY — ANDERSON (1965)

VORTICITY EQUATION

$$\text{I} \quad \frac{\delta}{\delta t}(\nabla^2 \Psi) = -J(\Psi, \nabla^2 \Psi) + \frac{g}{T_m^*}\frac{\delta T}{\delta x} - g\frac{\delta r_L}{\delta x} + \upsilon_M \nabla^4 \Psi$$

TEMPERATURE EQUATION

$$\text{II} \quad \frac{dT}{dt} = -w\frac{g}{C_p} + \left(\frac{dT}{dt}\right)_{PH} + \upsilon_T \nabla^2 T$$

T^* = VIRTUAL TEMPERATURE

$$u = -\frac{\delta \Psi}{\delta z} \qquad w = \frac{\delta \Psi}{\delta x}$$

$$\nabla^2 a = \frac{\delta^2 a}{\delta x^2} + \frac{\delta^2 a}{\delta y^2} \qquad J(a,b) = \frac{\delta a}{\delta x}\frac{\delta b}{\delta y} - \frac{\delta b}{\delta x}\frac{\delta a}{\delta y}$$

WET MODEL

Eq. II USES LAGRANGIAN SYSTEM. REVERSIBLE CONDENSATION–EVAPORATION. SATURATION MAINTAINED BY STATIC AND DYNAMIC ADJUSTMENT (WHEN $r_L > 0$)

when the model is two-dimensional. Axisymmetric and even three-dimensional versions have been begun as described in references 12 and 15. The earliest model of this type was a dry model done by myself and Witt in 1959 [31] which I will describe a little more here because it is the simplest to understand.

Murray and Anderson [33], among others, have done moist models with the condensation of vapor into liquid and the consequent release of latent heat. To the theoretician, especially the purist, this class of model, starting as it does from "fundamentals" would seem much more esthetically satisfying than the more parameterized entity type of model. These field of motion models so far have not produced much in the way of realistic results and are more an interesting sort of exercise. The reasons are twofold: firstly, the results have been sensitive to the type of differencing scheme and initial perturbation used; secondly, the most important factor in cloud dynamics, namely entrainment, is not handled properly. We all know that use of constant eddy coefficients is a very poor way of handling mixing in a convective situation. Actually much more sophisticated mixing schemes have been tried [35] but so far none has worked out very realistically or satisfactorily. For these reasons these models are at present better suited to study the very early or organization phases of convection, where the non-linear advective processes dominate, as illustrated in the next two figures.

Figure 31 shows an example of initial conditions in an early numerical convection experiment.

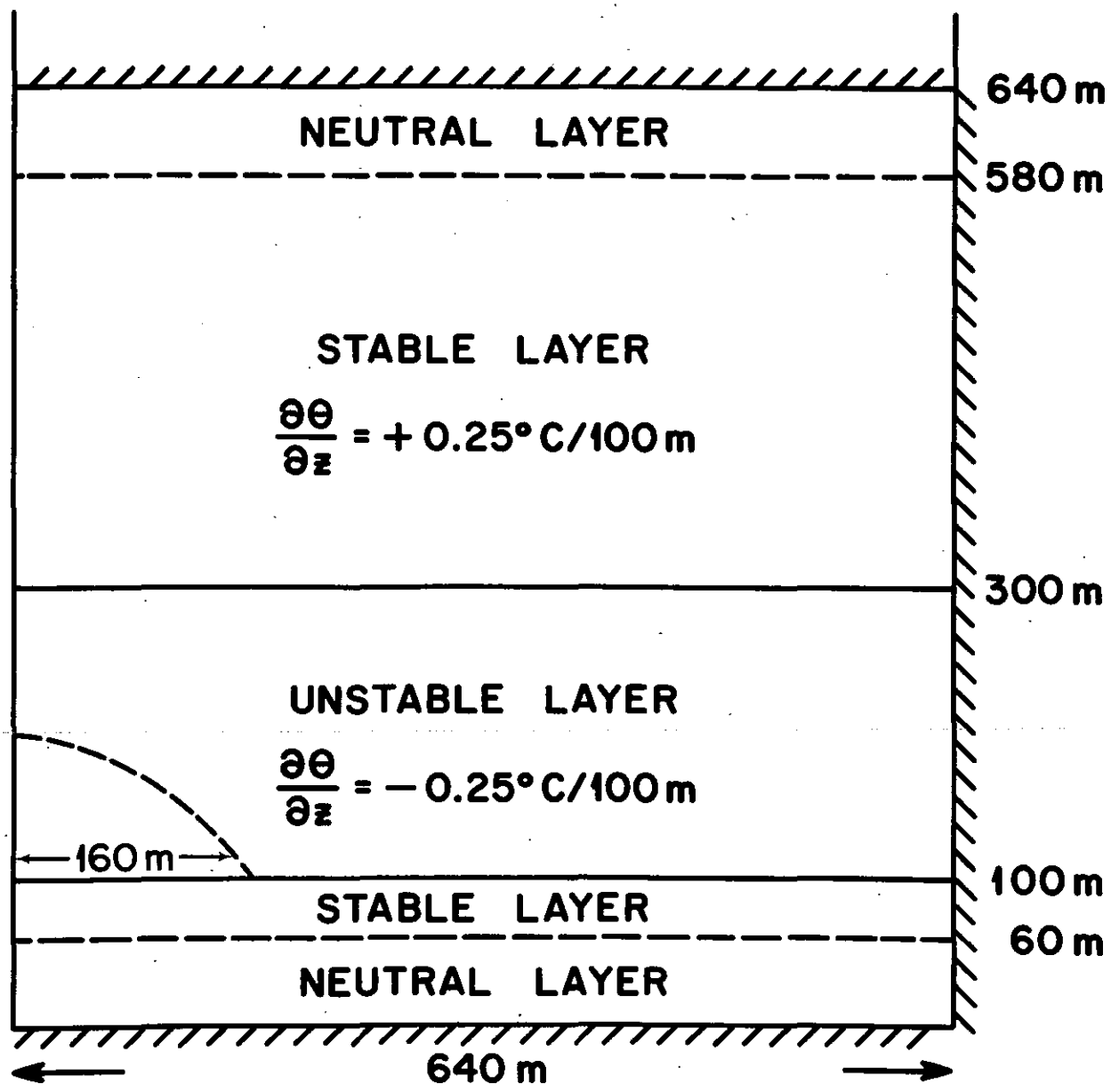

Figure 31. Framework for pioneering "field-of-motion" cumulus model. The initial density perturbation is shown by the dashed half semi-circle on the left (the other half is a mirror image). The space is divided into a 32 x 32 grid, with points separated by 20 n.

Figure 32 shows the growth of the convection bubble which follows.

For many years dynamical models of cumulus could progress either without any consideration of cloud physics or with very rough allowances for it. Cloud physics enters dynamical problems as follows: after entrainment, the largest resistive force against updraft growth is the weight of the liquid water that the cloud carries. As long as no precipitation is formed, the cloud particles are too small to fall out and hence all the condensed water is carried upward. We need to know how and how much precipitation falls out to determine the water loading. Due to the impetus of the modification experiments, in the late 1960's, cloud dynamic models had gotten advanced enough so they could go no farther without considering precipitation physics. The way we introduce precipitation physics in our simplified entity model is the same way it is presently put into virtually every cumulus model, so we shall use our model as the illustration.

Our model grew for and by means of seeding experiments on individual supercooled cumulus clouds. These seeding experiments were done with a quite different scientific foundation and motivation from the seeding experiments others have done to increase rain. We aim to release all the latent heat in the supercooled water, thus increasing cloud buoyancy and, under the right conditions, causing greatly increased vertical cloud growth. This is called "dynamic" cloud seeding because, in contrast to early seeding

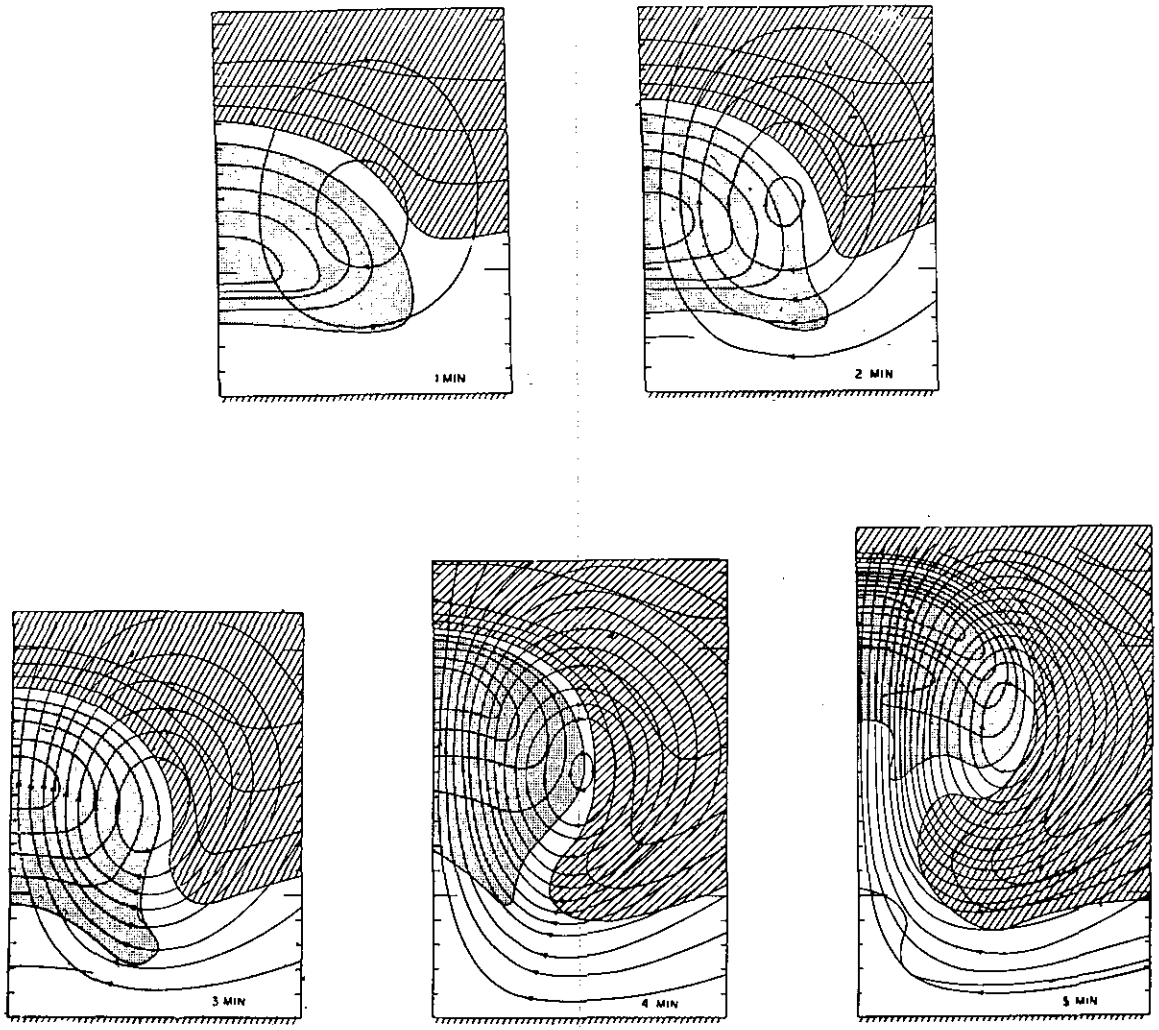

Figure 32. Resolution of solution in time steps of numerical "model" cloud of figure 31, for the first five minutes of its lifetime. Note the "bubble-like" thermal which develops, associated with a vortical circulation. Potential temperature isopleths (interval of 0.1°C) are solid lines without arrows; the dotted region includes all potential temperatures higher than that characteristic of the lower neutral layer, while the hatched region includes all those more than 0.1°C lower. Lines with arrows are streamlines of the flow.

work, the dynamics of the clouds are changed. Massive amounts of silver iodide are required for dynamic seeding and the seeding technology is an interesting topic in itself, which we do not have space to discuss here.

An ordinary medium sized tropical cumulus has a temperature excess over its environment of only 0.5 - 1.0° C. It is readily shown that freezing 3 gms/kg, or roughly 1.5 gm/m^3, of liquid water would raise the cloud temperature by 1° C ($dT = \frac{dQ}{C_p} \approx \frac{3 \times 80 \times 10^{-3}}{0.24} = \frac{0.24}{0.24}$) thus approximately doubling the cloud buoyancy. Under the right conditions, this could cause greatly increased vertical growth. We have defined the increased vertical growth attainable from dynamic seeding as the "seedability" of a cumulus cloud. Next we show how the numerical model has been evolved to predict seedability and other important features of natural and modified clouds, and how associated seeding experiments have interacted with the modelling activity to improve and accelerate the development of the model [36].

Figure 33 shows the key result of the 1965 single cloud seeding experiments and modeling effort. Seedability (abscissa) is predicted by the model. It is defined as the difference in maximum top height achieved by the cloud when seeded and unseeded. Seeding effect (ordinate) is measured in the statistically controlled or randomized experiment (fig. 34). If models and data were perfect, all seeded clouds would lie along the straight line with slope one, i.e. seeding effect equal to seedability, while control clouds would lie along the horizontal line, since regardless of seedability, they should not

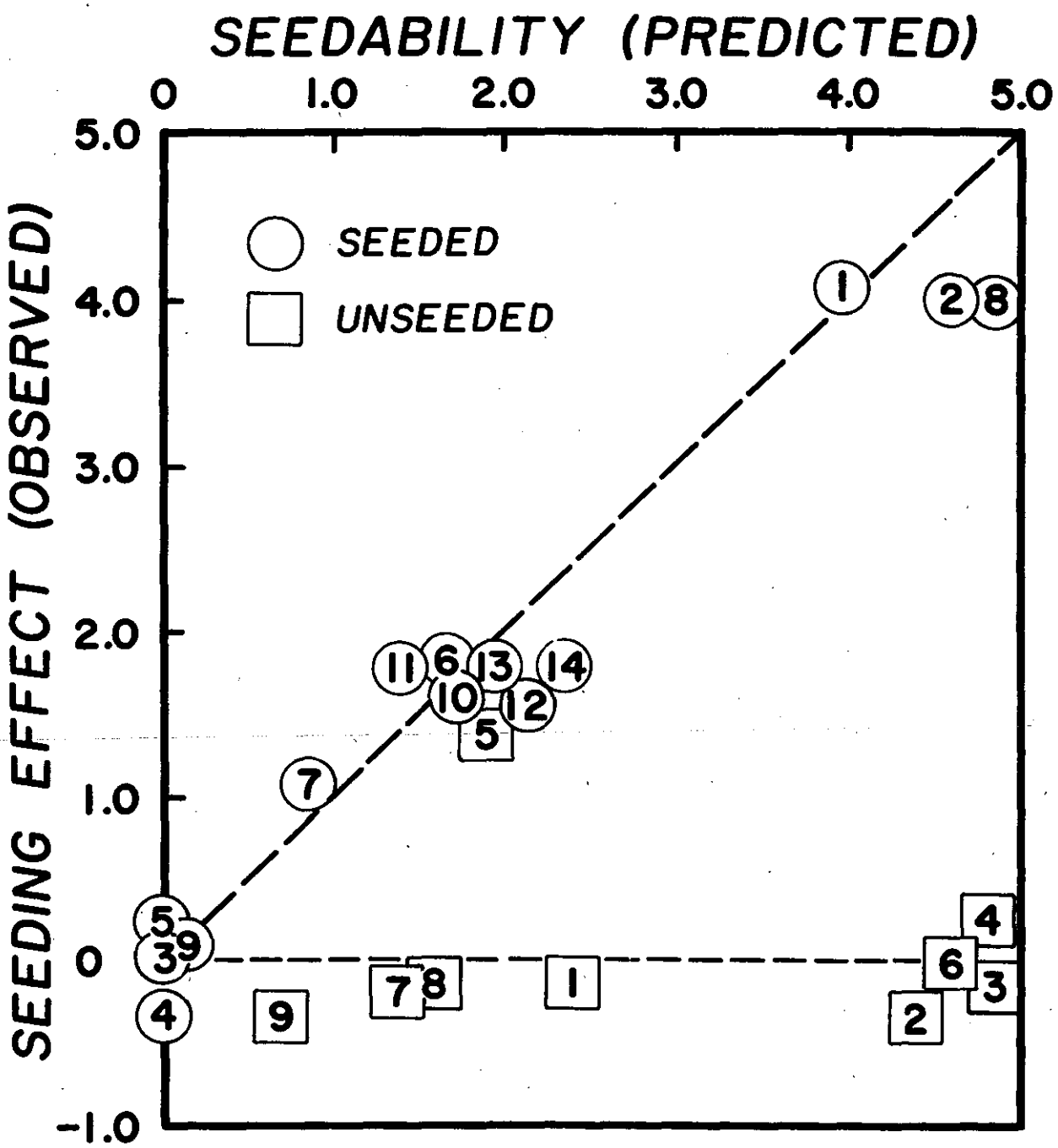

Figure 33. Seedability (predicted) vs. seeding effect. Both in km. Seedability is predicted top height difference between cloud when seeded and unseeded. Seeding effect is measured top height minus model predicted unseeeded top height.

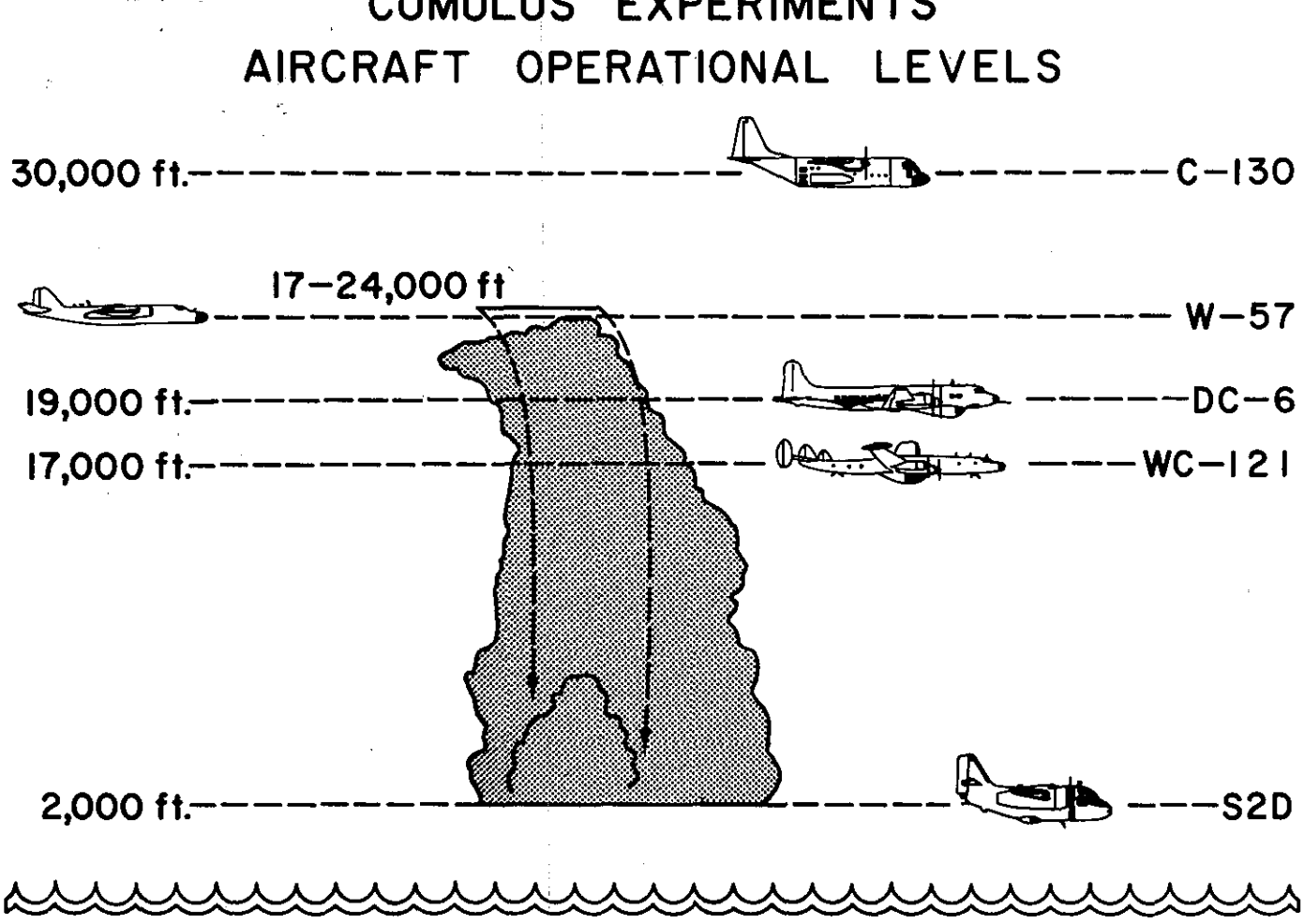

Figure 34. Schematic diagram of dynamic seeding experiment on single cloud. Seeder aircraft is flown near cloud top. Monitoring aircraft make one penetration prior to seeding and several afterwards.

exhibit any seeding effect. This diagram was a real landmark in modification work since it showed both a statistically significant height difference in seeded and control populations and also that the model has real skill in predicting seeded and control cloud properties. Different cumulus growth regimes (figs. 35-38) were shown to follow dynamic seeding, depending on the initial conditions of the cloud-environment systems.

The next step in the single cloud work was to establish that the seeded clouds rained more than the controls. This documentation was carried out by means of a calibrated radar as illustrated in figure 39. A series of experiments in south Florida showed that seeded clouds rained on the average three times more rain volume than the controls, the difference being about 270 acre-ft, significant at a level better than five percent. In the process of these experiments, it was found that "mergers" of two or more cumulus clouds rained about ten times more than the sum of their components. A series of randomized multiple cumulus experiments are currently underway in a 4000 sq mi target area to determine whether "mergers" can be induced by dynamic seeding and whether rainfall over the whole target can be modified. Early results are encouraging, but whether or not practical benefits ensue directly, continuation of the experiments is shedding light on the vital interactions of clouds which are so important in fueling and regulating the atmosphere.

The Experimental Meteorology Laboratory in NOAA is also making efforts on all fronts of cumulus modeling. In particular, we are

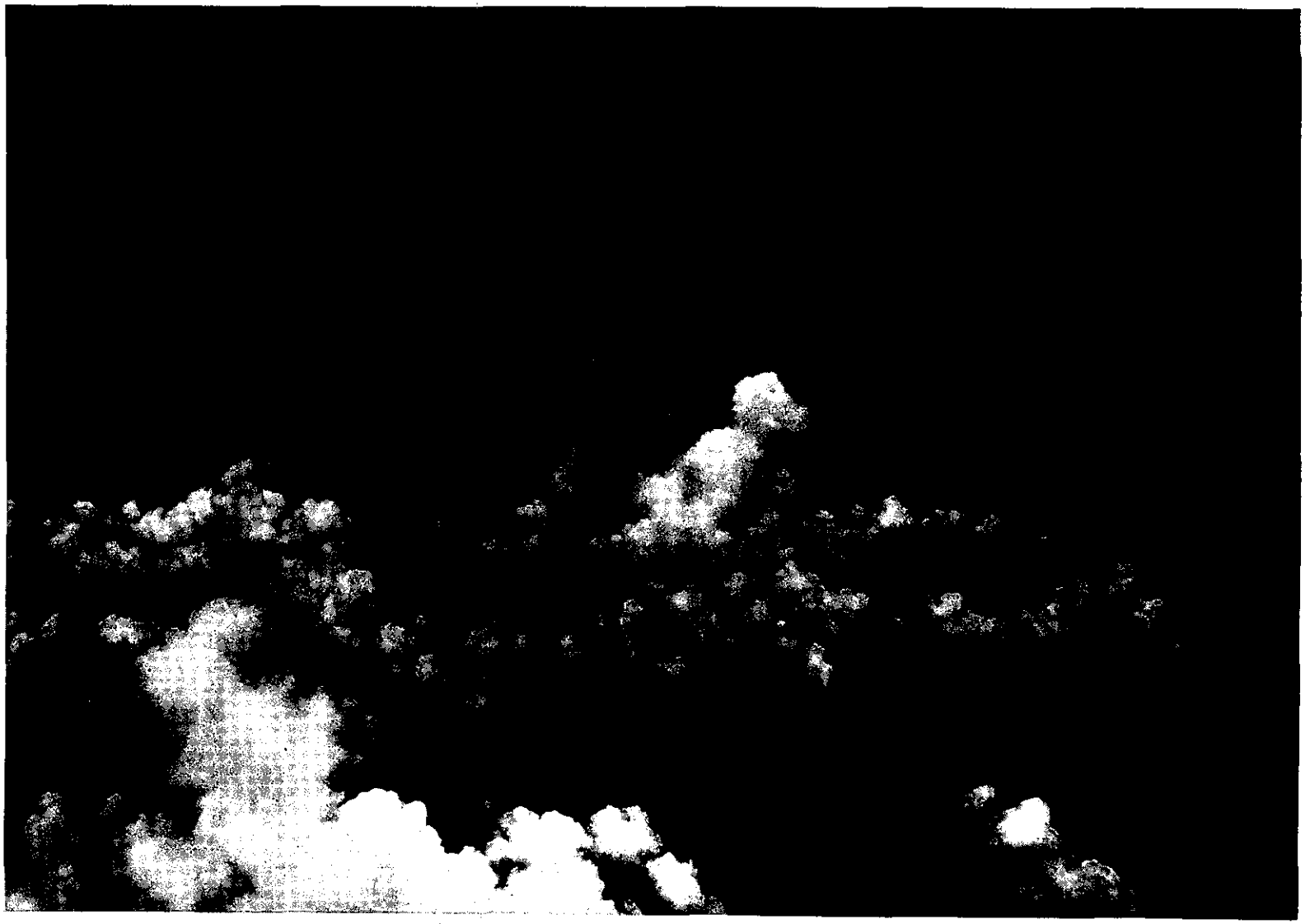

Figure 35. Typical tropical cumulus at time of seeding. Top at about 7.5 km or 24,000 ft.

Figure 36. Same cloud as figure 35, 38 minutes later. It is now a full-blown cumulonimbus.

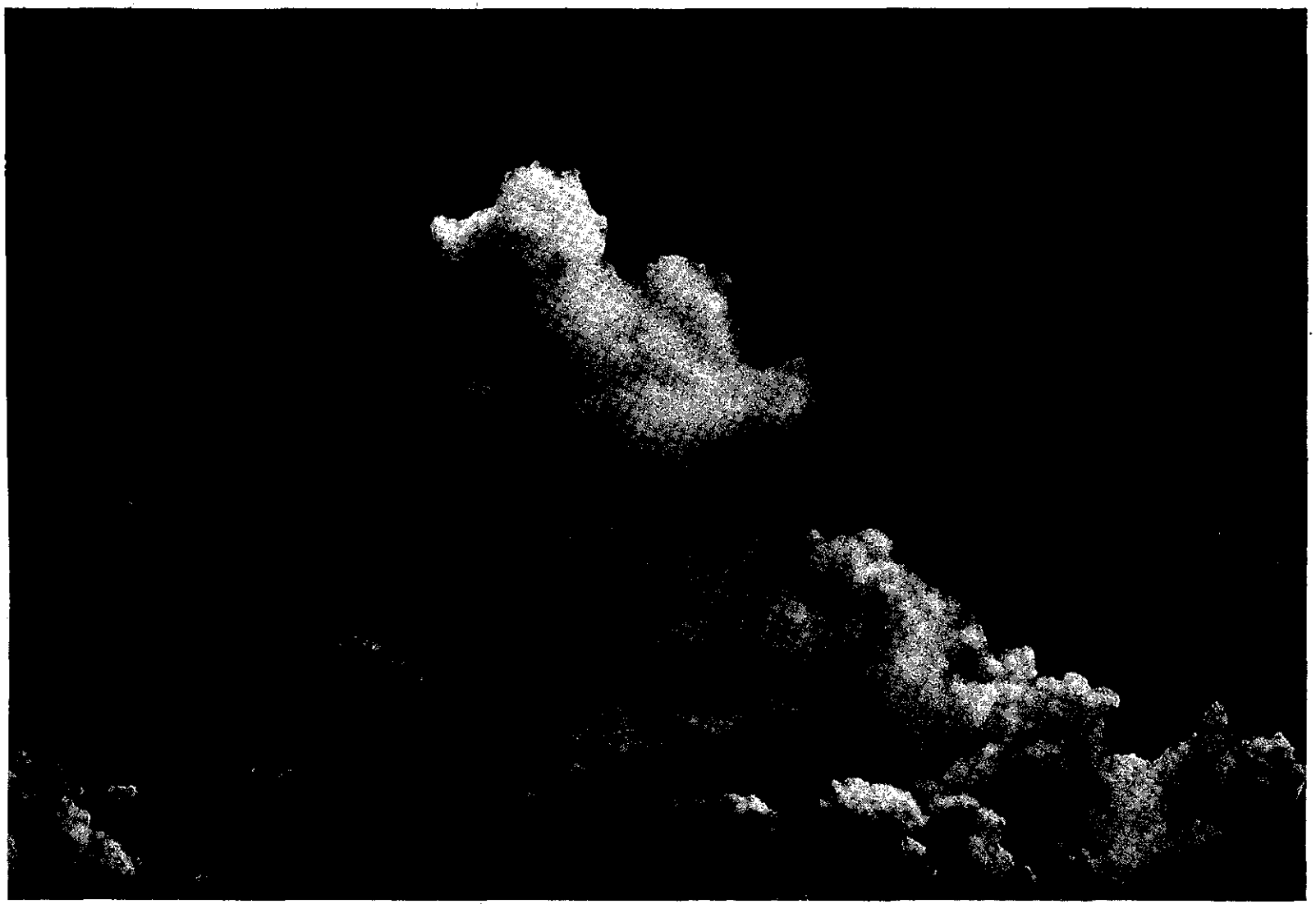

Figure 37. Photograph illustrating "cut off tower regime" which often follows dynamic cumulus seeding.

Figure 38. Photograph illustrating "no growth regime" following dynamic seeding. At 12 minutes after seeding, cloud looks unchanged, except that top has glaciated.

EXAMPLE OF CLOUD BASE ISO-ECHO CONTOURING
CLOUD 6, MAY 16 1968

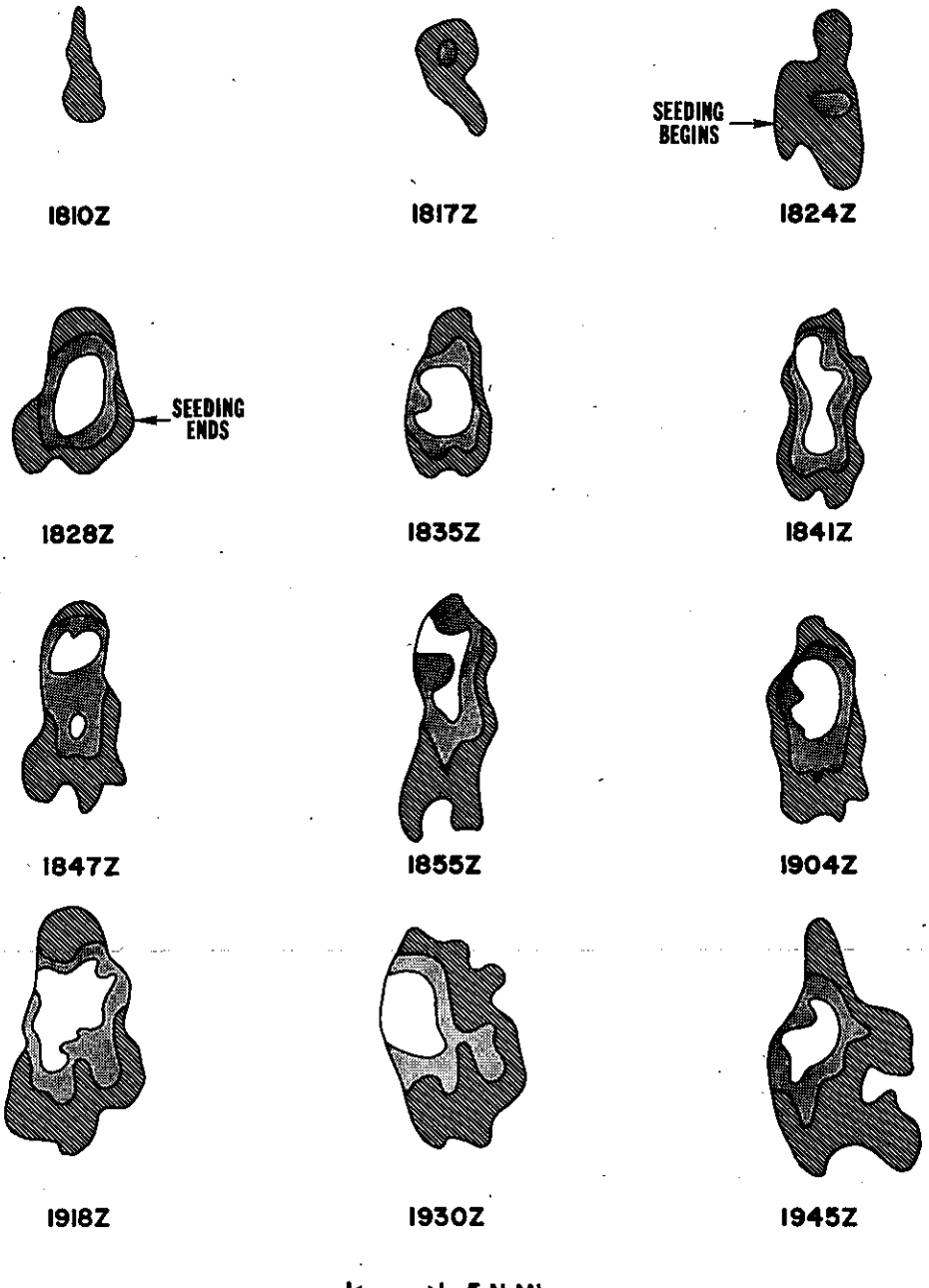

Figure 39. Contoured cloud base echoes showing (below) equivalence of contours to rainfall rate obtained from radar calibration. Area within each contour is measured and summed over time to give rain volume falling from cloud base.

trying to introduce in the field of motion models some of the insights that observations have enabled us to incorporate in the one-dimensional models. Recently a three-dimensional meso-scale model of the whole south Florida peninsula has been constructed, which investigates the effect of the heated boundary layer in controlling cumulus patterns.

At this point, we leave the discussion of cumulus clouds and models and turn to the role that these clouds play in the larger atmosphere. In particular, we will examine how cumulus clouds affect the important fuelling regions of the tropics, namely the trade winds and the equatorial trough zone.

4. EFFECTS OF CUMULUS CLOUDS ON TROPICAL AND BOUNDARY LAYER CIRCULATIONS

Let us take a closer look now at the trade-wind boundary layer and the important function that cumulus clouds play in determining its structure and in carrying out its transports.

Review figure 20 which shows the location of the trade winds; they blow equatorward and westward in both hemispheres. Let us focus our attention on the atmospheric boundary layer, particularly in the upstream and polar half of the trades. The vertical structure of the boundary layer is illustrated in figure 40. By boundary layer, I mean that layer where the wind departs significantly from geostrophic due to friction terms, that is height gradient of shearing stress, in the equations of motion and where the air is horizontally homogenous and fairly well mixed vertically due to turbulent and convective processes. So defined, the boundary layer includes both subcloud and cloud layers.

Figure 40 shows the vertical lapse rates of temperature and moisture in the trade-wind boundary layer. The lowest 600 m or so of the layer is well mixed. The temperature lapse rate is about 99 percent dry adiabatic. The mixing ratio is nearly constant with height (from bottom to top it decreases only about as much as its small fluctuations, or about 0.3 - 0.5 gm/kgm out of a mean value of 15 gm/kgm). This well mixed region has thus

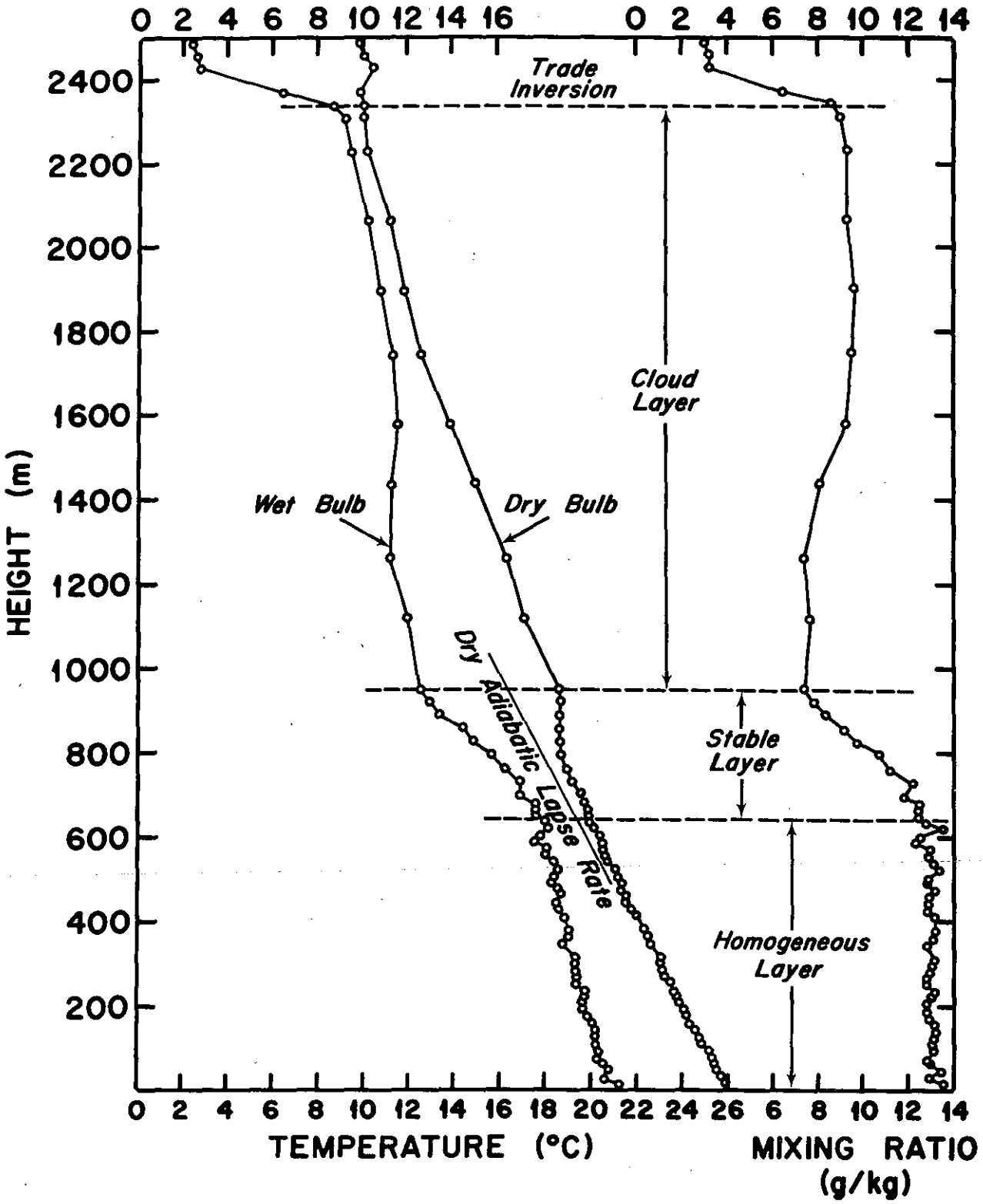

Figure 40. Structure of oceanic trade-wind boundary layer as determined with a typical high-resolution aircraft sounding. Note that the boundary layer includes the homogeneous layer, the stable layer and the cloud layer. Thus sounding was made in a clear region on a day when cloud base was at about 900 m.

been christened the "homogeneous layer." Its potential temperature also is almost, but not quite, constant with elevation. Weakly unstable in the lowest strata, the temperature lapse rate becomes barely less than adiabatic above 200 m elevation. Careful statistical studies of numerous profiles, like these shown in figure 40, show that under normal and strong trade-wind conditions the upper two-thirds of the subcloud layer are slightly statically stable in all but the upstream and poleward fringes of the trades. The trade winds are normally strong, with wind speeds averaging 6-8 m/sec. Hence the strong eddying motions below cloud are produced by wind shear in a statically near neutral, but slightly stable layer.

The effect of the stabilization upon the important scales of motion has been brought out by myriads of horizontal aircraft runs in the subcloud layer, with fast recording sensors of temperature, humidity and vertical air motions. While the moisture fluctuations and their correlations with updrafts are in phase throughout the subcloud layer, that is to say the upward-moving eddies are more moist than the descending eddies, the opposite is true of the temperature fluctuations. That means that in the upper 2/3 of the homogeneous layer, temperature fluctuations are out-of-phase with rising motions, so that the upward-moving air is colder than the downward-moving air and the surroundings. This out-of-phase relation applies to the shear-created eddies on the 50-300 m horizontal scale as well as the longer eddies. This suggests, but does not prove, that the sensible heat flux through most of the

sub-cloud layer is downward. Much more important mechanistically, however, it shows that the small turbulent eddies are commonly overshooting their level of zero buoyancy at least a thousand feet below cloud base, so that wind stirring is necessary to convey the water vapor the remaining distance upward to the condensation level. This is but one link in the now firm chain of evidence that the oceanic trade cumuli, unlike their continental relatives, do not have individual "roots" in buoyant cloud-scale thermals penetrating up into them from the sea surface. In fact, the aircraft records show that small-scale turbulence is no more developed on flights just below cloud bases than on those in the intervening clear spaces. This point is important in connection with cloud patterns and organization.

Looking above the homogeneous layer in figure 40, we see a slight stable layer with marked drying at just about the cloud base level. This stable layer is quite pronounced in the clear zones between the cloud groups, but it is much weaker or missing altogether in the cloudy zones. Above this we see the cloud layer, which has a temperature lapse rate about 1.5 times wet adiabatic, or conditionally unstable and commonly a very slight decrease of mixing ratio, usually about 2 gm/kgm per kilometer. The thickness of the cloud layer at a given location varies considerably from day to day, being deepened with a passage of the synoptic scale disturbances we discussed earlier. On the average, the cloud layer thickens downstream in the trades. It is only a few hundred meters in depth off the African and California coasts

and deepens westward and equatorward. By the time the trade-wind air has reached the longitude of Puerto Rico in the Atlantic, or Hawaii in the Pacific, the boundary layer averages 2-3 km in depth under undisturbed conditions. Topping the boundary layer is the famous trade wind inversion, which acts as a lid against the upward penetration of convection. The inversion is always a region of very rapid drying with height. Off Africa and California, the vertical temperature increase may be 5° C or more. The inversion weakens as it rises downstream, so that by the time the air reaches Puerto Rico, for example, we may only have an inversion of 1-2° C or just an isothermal layer. This material on the boundary layer so far is documented in references 16-18. Now let us turn our attention to the energetics, dynamics and mechanisms in the trade-wind boundary layer and to the role of this boundary layer in the large-scale circulation of the atmosphere.

Figure 41 shows a portion of the Pacific trade-wind system that has been studied in detail, particularly in references 41-43. Quantitative studies of other portions of the trades show that the relations deduced here are fairly general.

The heavy solid line denotes the air trajectory in the boundary layer. The air flow throughout the layer is nearly two-dimensional; that is, there is little or no wind turning with height. This makes it fairly non-formidable to construct analytical and numerical models, as I will outline later. While the winds do not rotate with height, the isobars do, in a counterclockwise

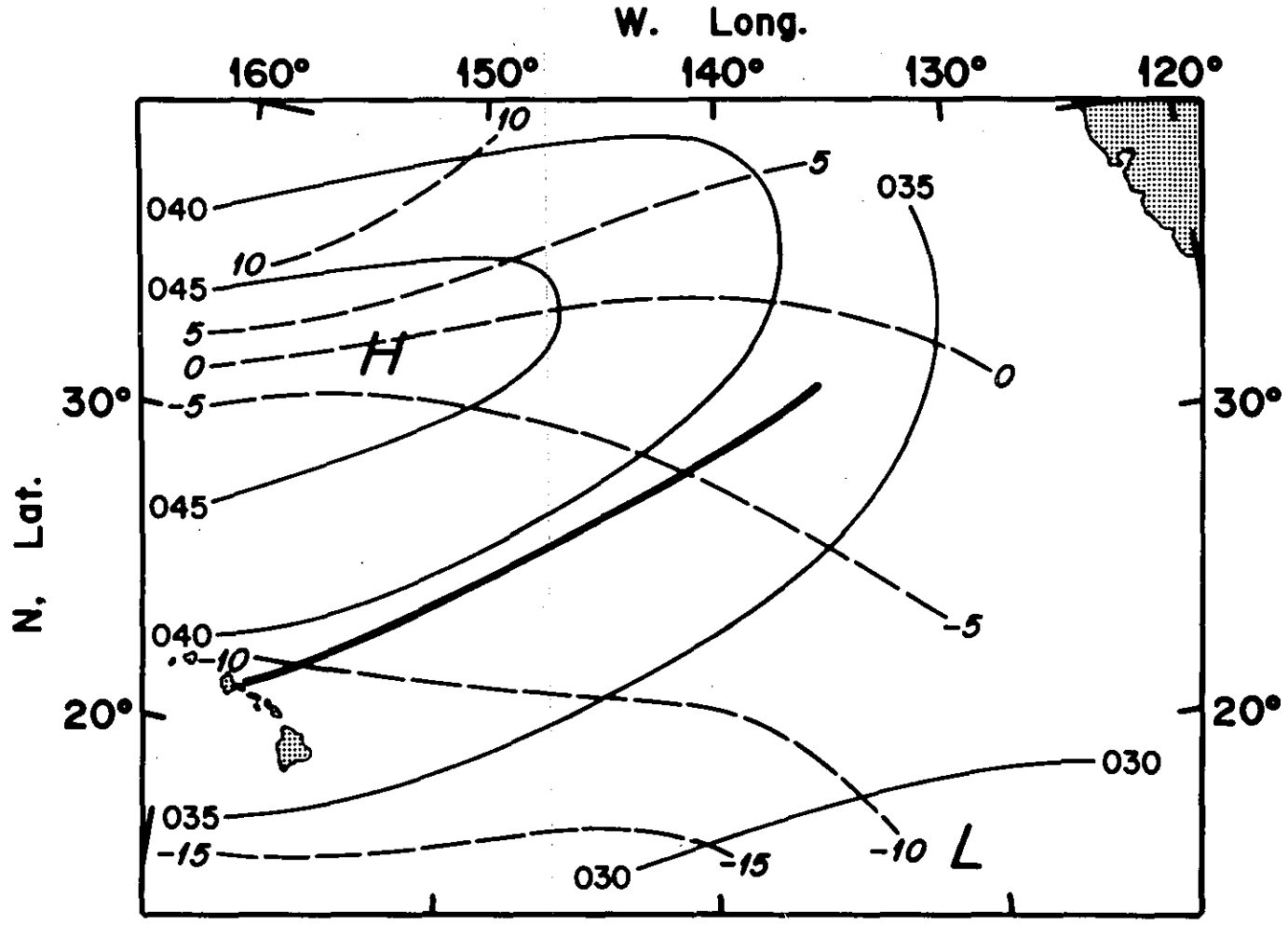

Figure 41.

Mean 700mb contours (10's ft, first digit omitted) July-October 1945, solid, and lines of equal gradient wind speed (m sec^{-1} positive values have component toward east), dashed. Solid line shows orientation of trade-wind trajectory in the Pacific Ocean, with the Hawaiian Islands at the downstream end.

sense. The dashed lines are parallel to surface isobars, while the light solid lines are the isobars at 3 km, the top of the boundary layer. Up here, we see that the flow is parallel to the isobars, or that it is very nearly geostrophic, meaning that friction forces have become very small. We can deduce that at the surface the friction forces are quite large, since the flow is strongly toward low pressure. We will see later that the cumulus clouds create the downstream pressure gradient that maintains the trade wind flow agains friction. There is a very interesting balance of forces in the lower boundary layer, when looked at in natural coordinates. The downstream balance is a close equality between pressure gradient force and the opposing force of friction, while the cross-stream balance is between the coriolis force (to the right) and the pressure gradient force (to left), or nearly geostrophic. A similar balance of forces prevails in some oceanic boundary layers, such as the Gulf Stream.

Now let us look at a vertical slice along this air trajectory. This vertical section is shown in figure 42. First note the division into layers that we saw before. We have the subcloud, the cloud and the inversion layer. The subcloud and cloud layers together are called the "moist layer." The moist layer deepens about 1000 ft in a distance of 500 miles downstream. Note that, paradoxically, the moist layer deepens in the face of mean subsidence. The lines with arrows are the streamlines. Subsidence in the trades is strong and averages 100 m a day descent or more. Note the most important feature of

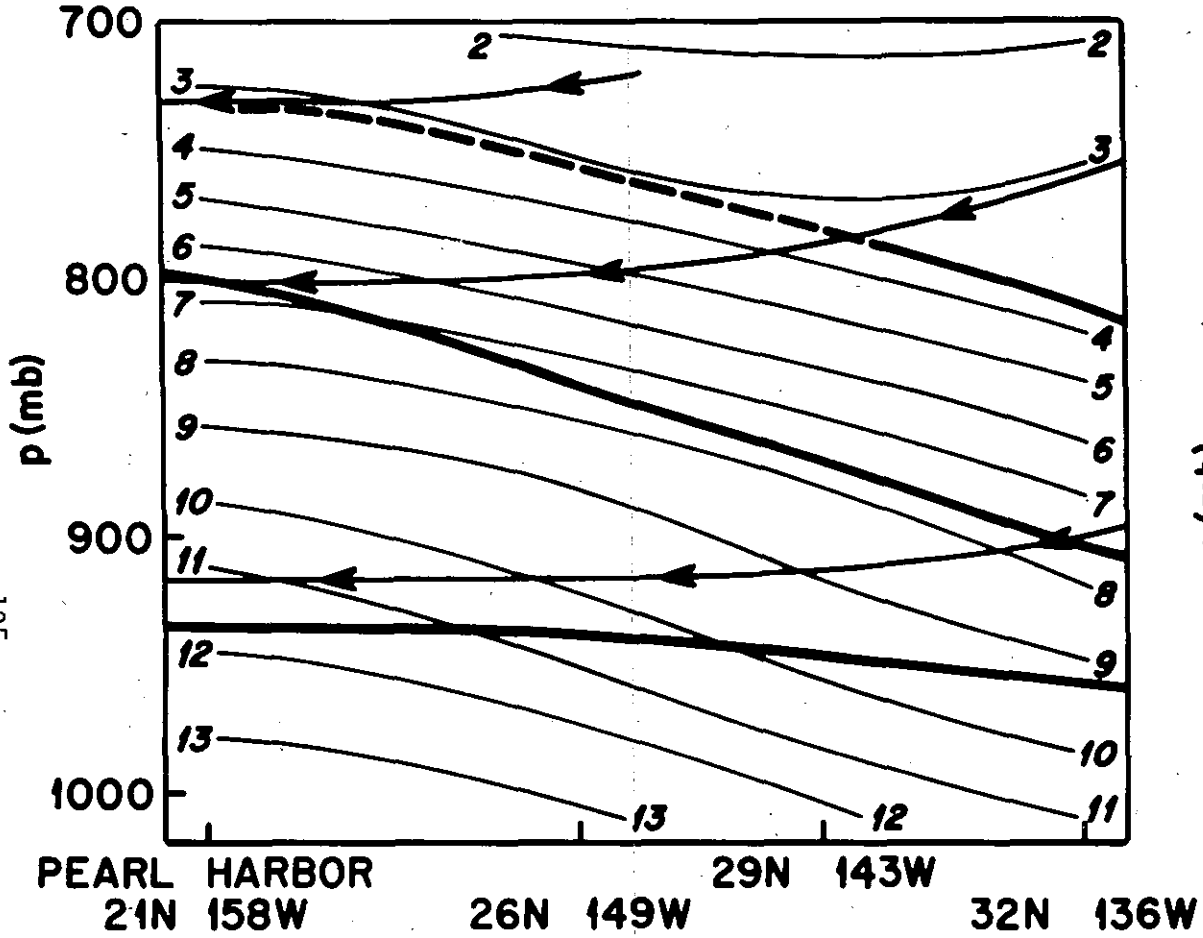

Vertical cross-sections of specific humidity (g/kg) in relation to sample air trajectories.

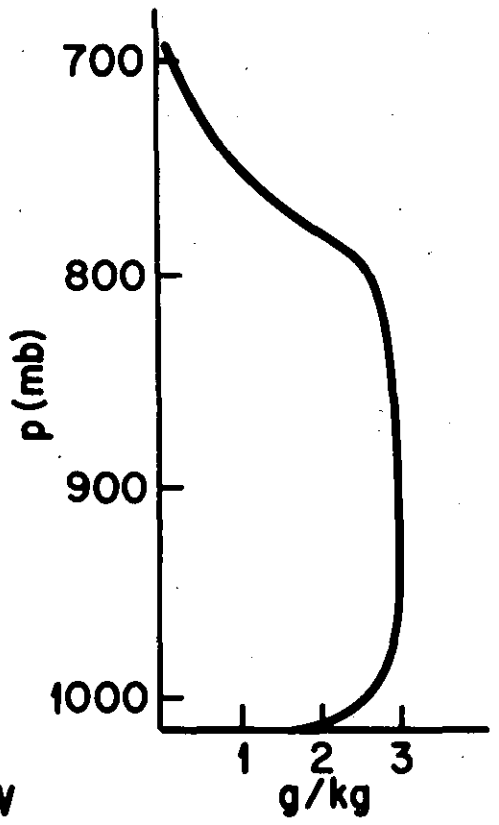

Vertical dist. of specific humidity difference (g/kg), Honolulu minus 32° N.

Figure 42.

this diagram, in addition to the thickening of the boundary layer downstream, is the moistening of the air along the trajectory. Note that the air trajectories move strongly toward increasing specific humidity. Actually the tradewinds export equatorward about 60 percent of the moisture they pick up by evaporation from the sea surface, while less than 40 percent is used up locally by precipitation. So we see that the trade-wind boundary layer accumulates moisture and exports it equatorward. This is its main function in the general circulation. What are the mechanisms by which it carries out this function? Here is where the trade cumulus cloud we discussed last time play a very important role.

Figure 43 shows a schematic picture of the mechanism at work. As we mentioned, in the subcloud layer the evaporated moisture is transported up to cloud base by turbulent eddies, 100-300 m in dimension, created by wind stirring. In the cloud layer, the clouds themselves do the vertical pumping of the moisture. Some few of the clouds poke their heads into the inversion and when their towers cut off and evaporate the inversion is moistened, weakened and raised. In a detailed study of this mechanism [40] I showed that the observed downstream deepening of the moist layer is achieved if only 1/10 of the cloud matter active in mid-layer is left above the inversion base in the process of tower dissipation.

Now let us inquire whether these weak and undramatic looking trade cumuli can pump upward the huge quantities of moisture that the budget

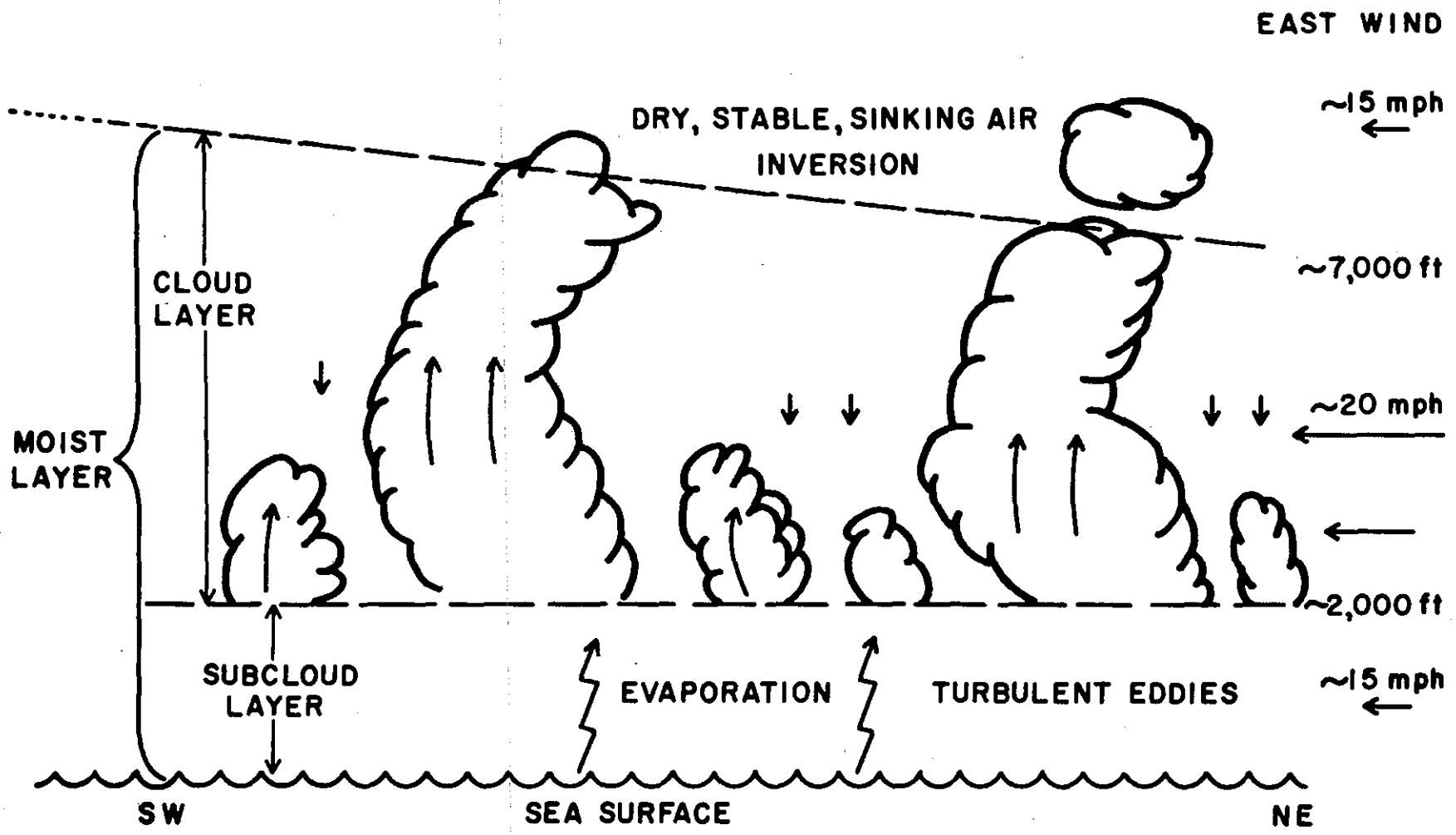

Figure 43. Schematic illustration of the processes at work along trade-wind trajectory of figures 41 and 42.

studies have shown us must be moved vertically up through the trade-wind belt from 10-20° N, which covers an area of 32×10^{16} cm^2. The evaporation is roughly 1.1×10^{15} cal/sec. Of this latent heat supply, about 84 percent or 1.5×10^{12} gm/sec of water vapor is being transported upward through the lower cloud layer. The computation shown in table 7 shows what the clouds must be like to accomplish this enormous transport. Equation (1) of table 7 is the equation for the transfer of water vapor across a given reference level, say at 1400 m or about 850 mb. F is the vertical water vapor flux in gm/sec, w is vertical velocity in cm/sec, ρ is air density in gm/cm^3, q is the specific humidity in grams of vapor per gram air and Δ is area in cm^2. The subscript a refers to the actively ascending cloud portions, c to stationary or descending cloud portions, and d to the more weakly descending clear air between clouds. The superscripts indicate that the in-cloud air is saturated. Since this is an order of magnitude calculation, the liquid water content (~10 percent of the vapor), the vertical component of the mean motion (100 m/day or 10^{-3} cm/sec) and the 0.5-2 percent density variations between cloud and clear air are neglected, so that we obtain (2) in table 7. In (2) ρ_m is the mean air density at the level, the bars denote mean values, q_s is the saturation specific humidity at the average air temperature and q is its clear air value. Equation (3) is the equation of continuity. We get (4) by substituting (3) into (2). All quantities for evaluation of w_d from (4) are known and written below the equation. w_d is 1.2 cm/sec, a value well supported in reference 40 by deductions from the

$$F = \Sigma_a w_a \rho_a q_a^* \Delta_a - \Sigma_c w_c \rho_c q_c^* \Delta_c - \Sigma_d w_d \rho_d q_d \Delta_d \quad (1)$$

$$\frac{F}{\rho_m} = (\bar{w}_a \Delta_a - \bar{w}_c \Delta_c) q_s - \bar{w}_d \Delta_d q \quad (2)$$

CONTINUITY:

$$\bar{w}_d \Delta_a - \bar{w}_c \Delta_c = \bar{w}_d \Delta_d \quad (3)$$

SUBSTITUTING (3) INTO (2) WE HAVE

$$\bar{w}_d = \frac{F}{\rho_m (q_s - q) \Delta_d} \quad (4)$$

$F = 1.5 \times 10^{12}$ gm/sec $\quad \rho_m = 1.1 \times 10^{-3} \quad q_s = 13.6$ gm/kgm

$q = 8.0$ gm/kgm $\quad$ MEAN CLOUDINESS = 35%

$\therefore \; w_d = 1.2$ cm/sec

FROM (3)

$$\bar{w}_a = \frac{(\bar{w}_c \Delta_c + \bar{w}_d \Delta_d)}{\Delta_a}$$

IF 94% OF CLOUDY MATTER DESCENDS AT $w_c = 10$ cm/sec AND 6% OF THE CLOUDY MATTER ACTIVELY RISES,

$$\bar{w}_a = 2 \text{ m/sec}$$

Table 7

Woods Hole measurements. Now we solve (3) for w_a. If 94 percent of the cloudy matter is inactive and descending at a rate of 10 cm/sec, so that only two percent of the area (six percent of the cloudy matter) is actively rising, w_a comes out as 2 m/sec, in conservative agreement with the Woods Hole cloud census. Thus, despite their appearance, the ordinary trade cumuli are easily adequate fuel pumps; they are raising energy more than 100 times as fast as the rate of dissipation by all air and sea motions combined. The details of the flux calculations, supported by examples from cloud observations, are presented in reference 38.

In addition to their role in moisture accumulation and pumping, the trade wind cumuli also perform a vital function by warming the trade-wind boundary layer. The warming is shown in figure 44. We see that the air trajectories move toward higher potential temperatures in the boundary layer but parallel to the isentropes above the boundary layer. I have presented a model of how the clouds warm the air in reference 40. Briefly, energy is added by precipitation release and buoyant ascent in the cloud groups and then converted to sensible heat as the air descends between cloud groups. Although the amount of sensible heat accumulation in the trade wind boundary layer is numerically small (1/4) compared to the latent heat accumulation, nonetheless it is vital to driving the trades against friction. In reference 42 I have constructed an analytic model of how the heating by the clouds maintains the trade winds. The basic physics of this model can be explained qualitatively by

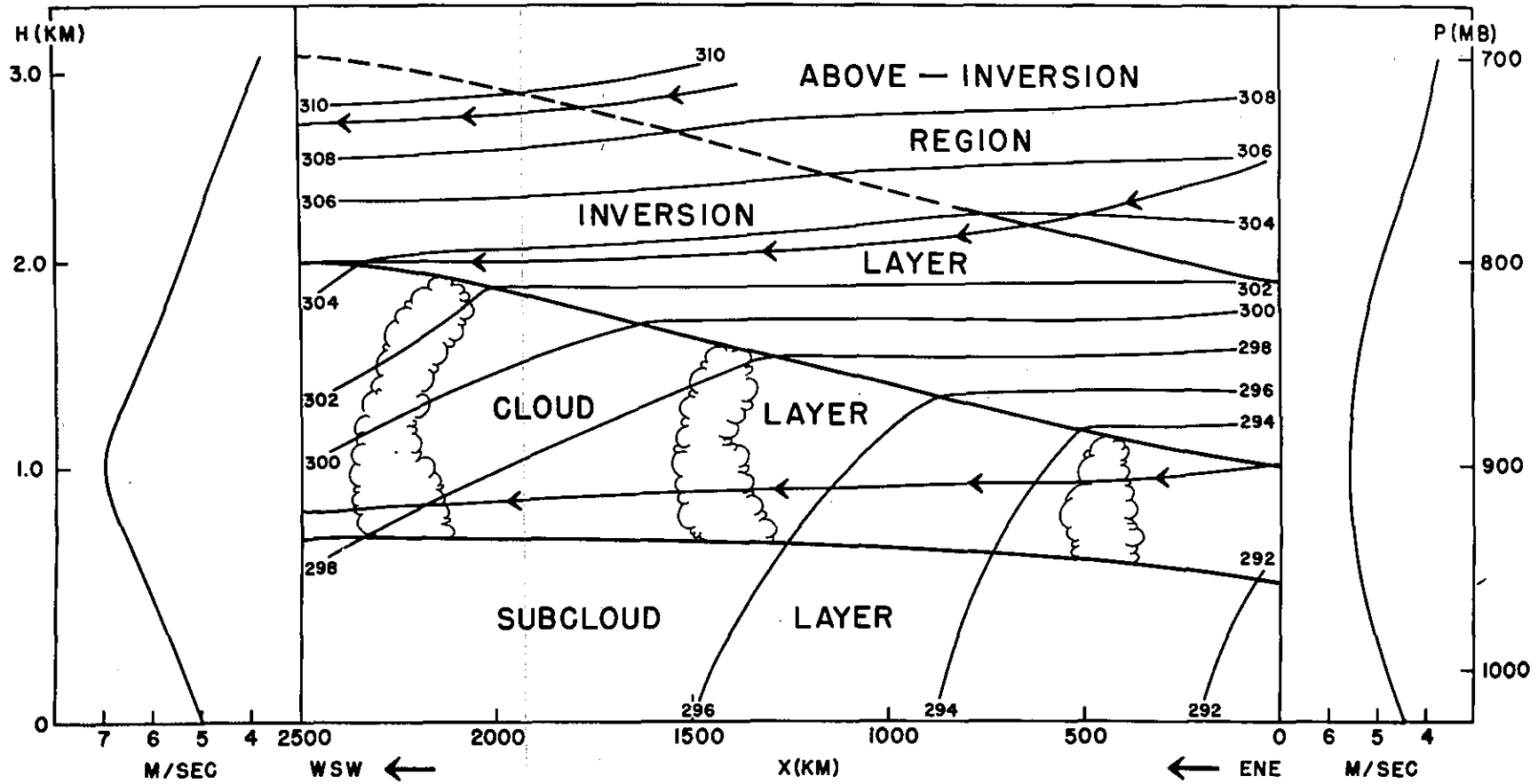

Figure 44. Vertical structure of the air along the trajectory of figures 41-43. Horizontal distance given in km downstream of entrance end. Vertical coordinate to right in mb, to left in km (approximate). The heavy lines separate the layers described in the test. The lines with arrows are the trajectories, while the lighter solid lines are potential temperature isopleths labelled in degrees absolute. Trade cumulus clouds are entered schematically. To the right is the profile of windspeed (along the section) at the upstream end and to the left is the windspeed profile at the downstream end. Windspeeds in m/sec.

referring to this illustration. The cloud heating maintains the wind flow by means of a downstream pressure gradient which amount to 5 mb in 2500 km at the surface. This pressure drop is explained by simple hydrostatistics when we point out that the 700 mb surface is level along the section. The warmer, less dense air at the downstream end leads to a lowered surface pressure. As we can see, the pressure gradient force directed downstream must be slightly stronger than the opposing force of friction because the trade wind actually increases downstream. These features are automatically predicted in the model when the heating function due to the clouds is introduced, via the thermodynamic equation, into the equations of motion.

Because the trade-wind increases downstream in a two-dimensional flow field, subsidence occurs as a consequence. Thus we get a stable interaction between scales of motions in the trades. If the clouds are more active and precipitate more, then the downstream pressure drop is larger, leading to a larger wind increase and enhanced subsidence, which acts to suppress the clouds. If, on the other hand, the clouds weaken and rain less, the pressure drop is less, with reduced wind acceleration and reduced subsidence, which lets the brake off convection and allows the clouds to rejuvenate again. This explains the pronounced trade-wind steadiness. Recently, a non-linear version of this model has been solved on the computer, with essentially the same results, which are presented by Arthur Pike [43].

Figure 45 shows what happens to the water vapor exported

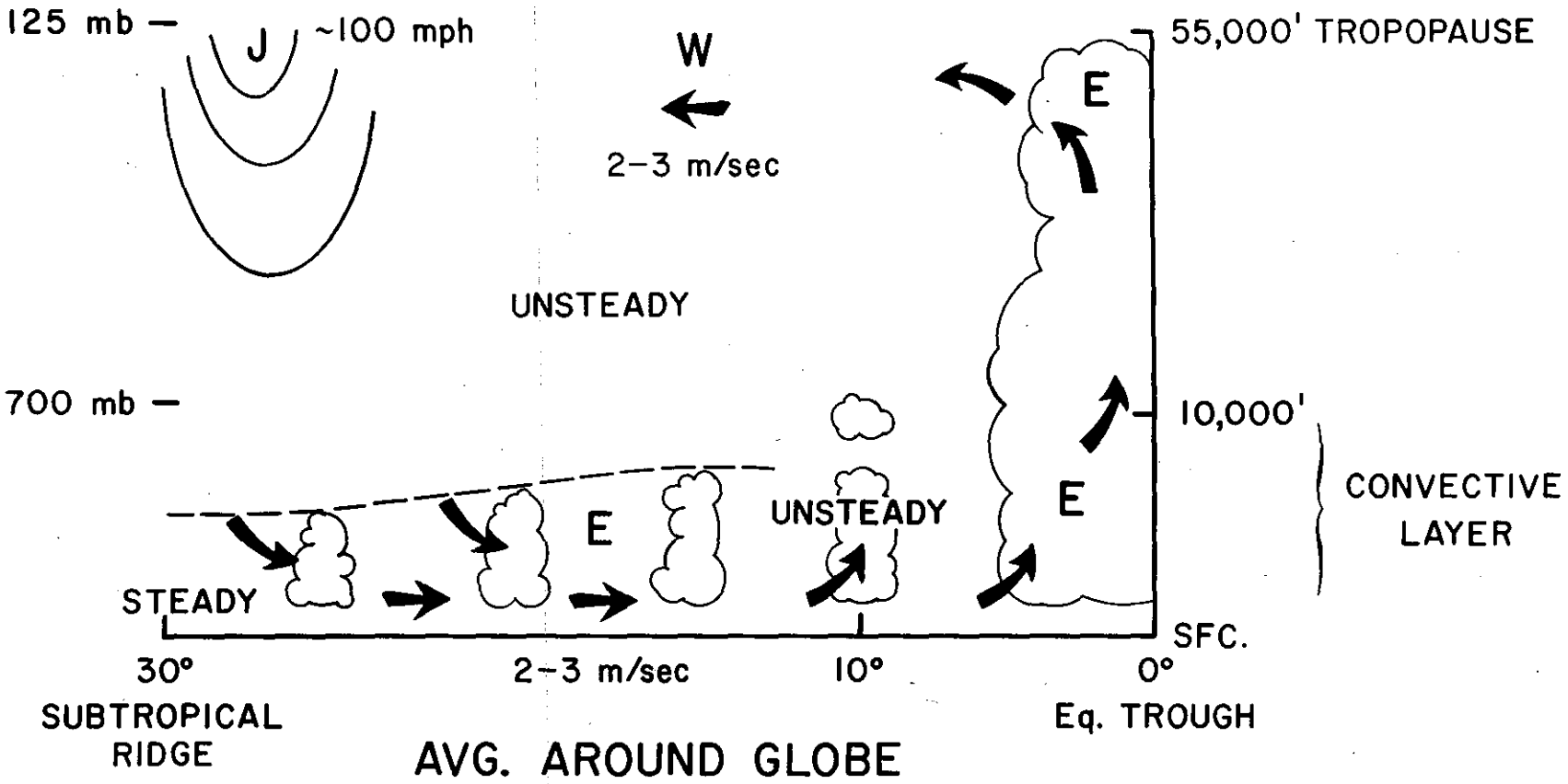

Figure 45. Schematic meridional cross-section through trade winds and equatorial trough Trade-wind inversion denoted by dashed line, subtropical jet stream core by J.

equatorward by the trades. It is condensed and precipitated by giant cloud systems in the equatorial trough zone. In discussing the global heat balance, we saw the enormous importance of this heat release. In a budget study of the equatorial trough zone [44] Riehl and I showed how these large clouds provide the "pressure head" that drives the ascending branch of the Hadley cell. The precipitation heating maintains a warm core in the equatorial trough, so that the air column there is lighter than the outlying air columns. This means that the surface pressure is lower, maintaining the inflow of low-level air into the trough. But the warm core, being less dense, also has a slower decrease of pressure with height than its surroundings, so that at upper levels, the equatorial zone has high pressure, thereby maintaining the poleward outflow aloft.

The cumulus clouds however have another vital, but more subtle, function in the dynamics of the equatorial firebox. This function was also revealed in the budget study and is illustrated in figure 46. In this case a joint atmosphere-ocean budget was made for total heat energy, $Q \equiv c_p T + Agz + Lq$, namely sensible heat plus potential energy plus latent heat. We assessed from measurements the latent and sensible heat influx from the sea and the radiation losses. We also computed from measurements the lateral low-level inflow and upper outflow across the poleward boundary. Note that there is no lateral heat flow at all across the trough line itself; this was demonstrated in another part of the study (recall that this is a seasonally migrating

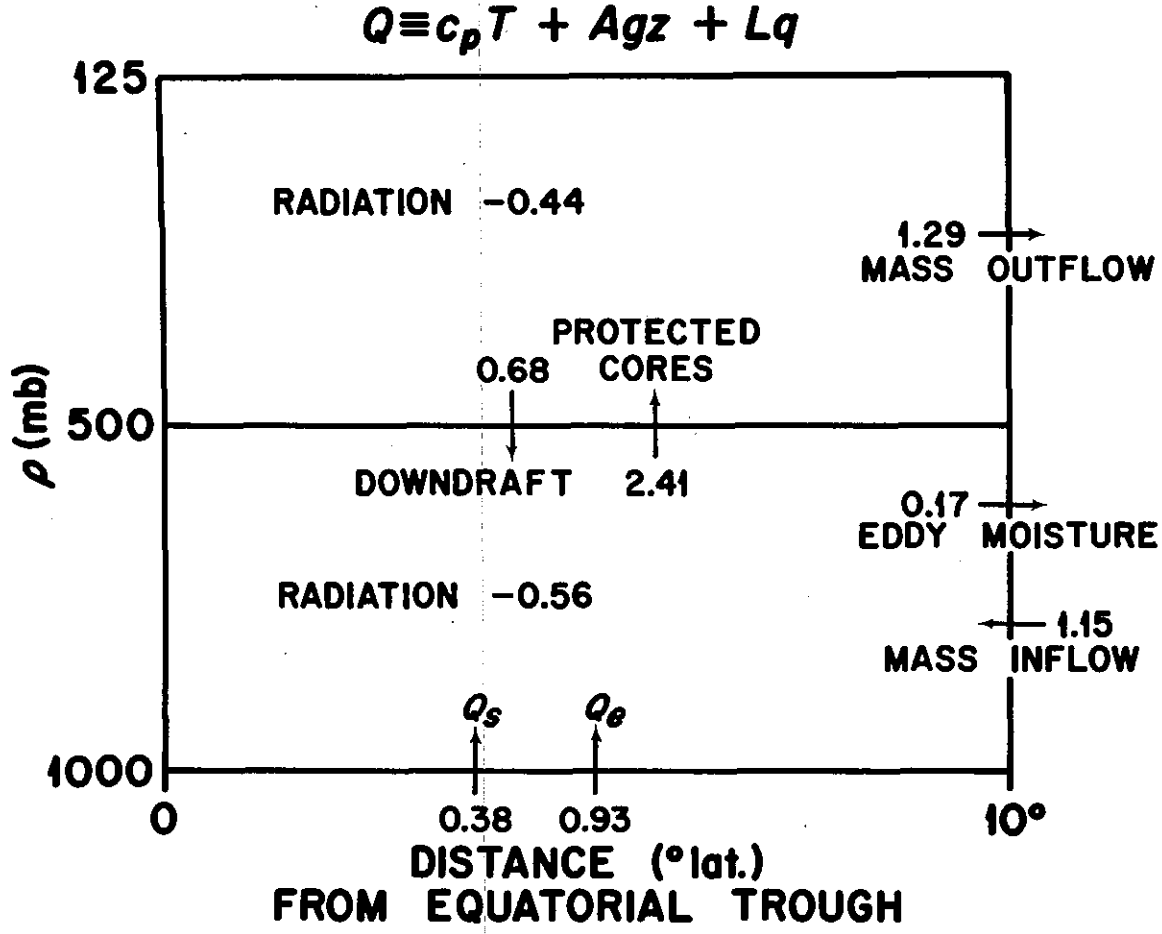

Figure 46.

Heat budget for winter side of equatorial trough zone. (After Riehl and Malkus, 1958, Fig. 18.)

Fluxes in 10^{15} cal/sec for 10°-latitude belt. Troposphere divided into two layers, 1000-500 mb and 500-125 mb. Vertical arrows through 500 mb surface denote fluxes required for joint heat energy and mass balance in each layer, hypothesized due to protected cumulonimbus cores partially compensated mass-wise by downdrafts.

boundary). In the lower layer, the mean circulation import (mass inflow) is 72 percent in Lq or latent heat and 28 percent in $c_p T$ or sensible heat. The 34 percent larger upper export, on the other hand, is 98 percent in the form of sensible heat plus potential energy. The clouds have, as we already said, effected the conversion. For the more subtle role of the cumuli, look at the vertical transport of energy. Note that we have concentrated all the upflux in what we call the "protected cores" of cumulonimbus clouds.

This is a revolutionary concept, called the "hot tower hypothesis." It means that the rising portion of the meridional or Hadley cell is concentrated in the restricted regions of the towering cloud bands within tropical disturbances and operates by means of selective buoyancy on the large-cumulus space and time scale. How did we deduce this? The information is provided in figure 47 which is a vertical profile of Q in the trough zone itself (dashed) and 20° poleward of it (solid). The clue to the deduction lies in the Q minimum at about 750 mb. This shows that a gradual slow mass circulation, as the Hadley cell was envisaged in the past, could only transport upward low energy air above this level and thus could not provide the heat energy to balance radiation losses and provide the poleward expert. The only way to balance the budget of all layers is to have all the air imported from the trade-winds ascend from cloud bases to the upper troposphere with virtually undilute properties of the subcloud layer. The only way that this can be done is for the low-level air to rise in buoyant cloud towers fat enough to be protected

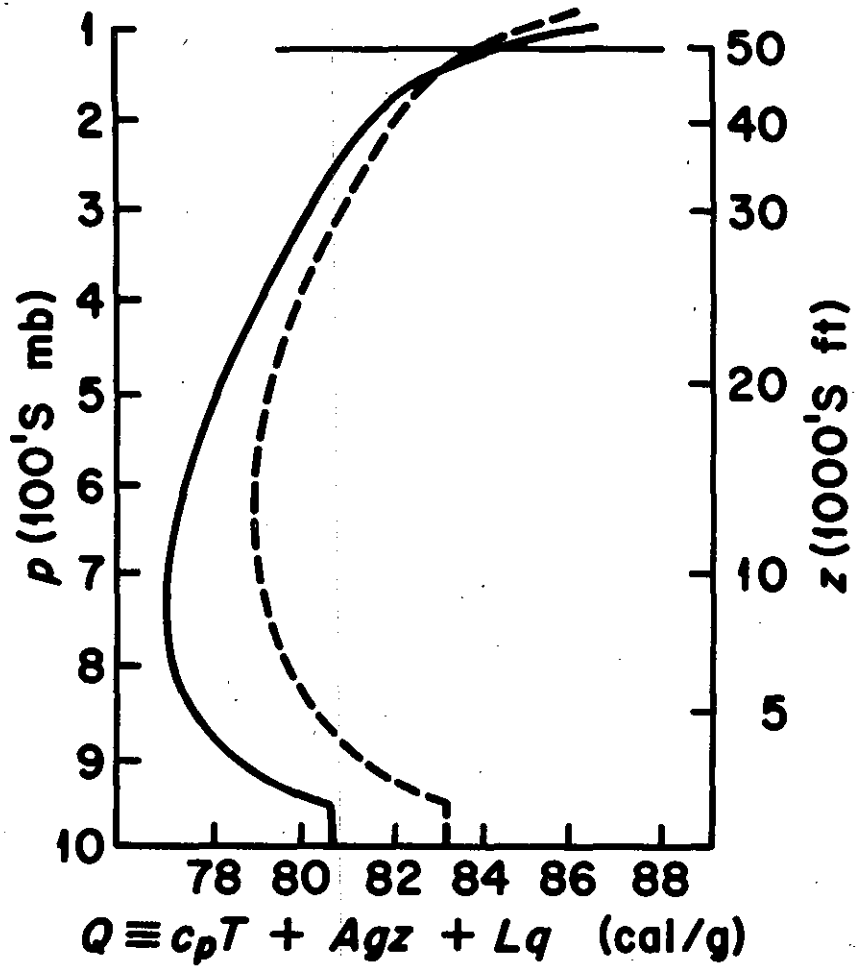

Figure 47.

Vertical profiles of $Q \equiv c_pT + Agz + Lq$, total heat energy. (After Riehl and Malkus, 1958, Fig. 15.)

Solid profile is for 20° latitude from trough. Dashed profile is for trough zone itself. Abscissa in cal/gm. Left ordinate in 100's of mb, right ordinate in 1000's of ft. Solid horizontal line denotes mean position of tropopause.

from entrainment. In fact, we found that somewhat more air must rise up in cumulonimbi than all that imported from the trades; hence the need for some recirculation in downdrafts is within the uncertainty of the budget calculations.

The undilute upward mass flux through the 500 mb surface required in figure 47 is about 18×10^{13} gm/sec. If the protected towers ascend with the conservative speed of 5 m/sec, they occupy an area of roughly 4×10^{14} cm^2 or 0.1 percent of the equatorial belt 10° latitude in width. An intriguing hierarchy of fractional area occupied by the various scales of phenomena is suggested in table 8.

From that area tabulation in the table we see that about 30 synoptic disturbances (wave length ~1350 km) are needed at a given time in the equatorial belt. With each active cloud having a diameter of 3-5 km, energy balance requires 50-150 rising towers per disturbance. The most striking result of this work is, in fact, that summing for the whole 10° belt only about 1500-5000 active giant clouds are needed to convert the water vapor fuel imported from the trades to maintain the warm core and heat budget of the trough and to provide for its high level poleward export. Each cloud tower pumps about 10^{12} cal/sec through the mid-troposphere and in its 30-60 minute lifetime releases a net amount of condensation energy greater than that of a hydrogen bomb ($\sim 2.4 \times 10^{14}$ cal).

We see here an outstanding example of the streakiness of

AREA OF EQUATORIAL ZONE = $A = 4 \times 10^{17} cm^2$

AREA OCCUPIED BY SYNOPTIC DISTURBANCES = $10^{-1}A = 4 \times 10^{16} cm^2$

AREA OCCUPIED BY ACTIVE RAIN = $10^{-2}A = 4 \times 10^{15} cm^2$

AREA OCCUPIED BY UNDILUTE TOWERS = $10^{-3}A = 4 \times 10^{14} cm^2$

Table 8

geophysical fluids. Tropical cumulus clouds are not randomly distributed, but are highly organized into systems and patterns. These patterns are discussed and illustrated in the final section.

5. CLOUD GROUPS AND PATTERNS

The patterning of atmospheric clouds is one of their most fascinating and least succesfully modelled features. Clouds are arranged into patterns on a hierarchy of space and time scales from the climatological, through the synoptic, down to mesoscale and smaller. Here we will begin on the large scale end and work down.

In order to examine synoptic scale cloud patterns, let us look at some pictures. By synoptic scale, I mean distance scales of roughly 1000 miles and persistence of several days. Synoptic scale cloud patterns are usually associated with recognizable weather systems on the standard charts; that is, each type of circulation perturbation has a characteristic cloud pattern.

Figure 48 is a world satellite mosaic for September 18, 1967. Its outstanding synoptic features are four tropical storms. In the eastern Pacific we see Tropical Storm Nanette (west) and Tropical Storm Monica (east). In the Atlantic, we have the remains of moderate Hurricane Doria and we see Hurricane Beulah in its most mature and intense phase about to strike the Gulf Coast of the U.S. Hurricane Beulah was one of the great hurricanes of the Gulf region and did over $200 million dollars worth of damage. In addition to the hurricanes, we see a tropical wave in the eastern Atlantic, which originated over Africa. We see a frontal system in both the northern and southern

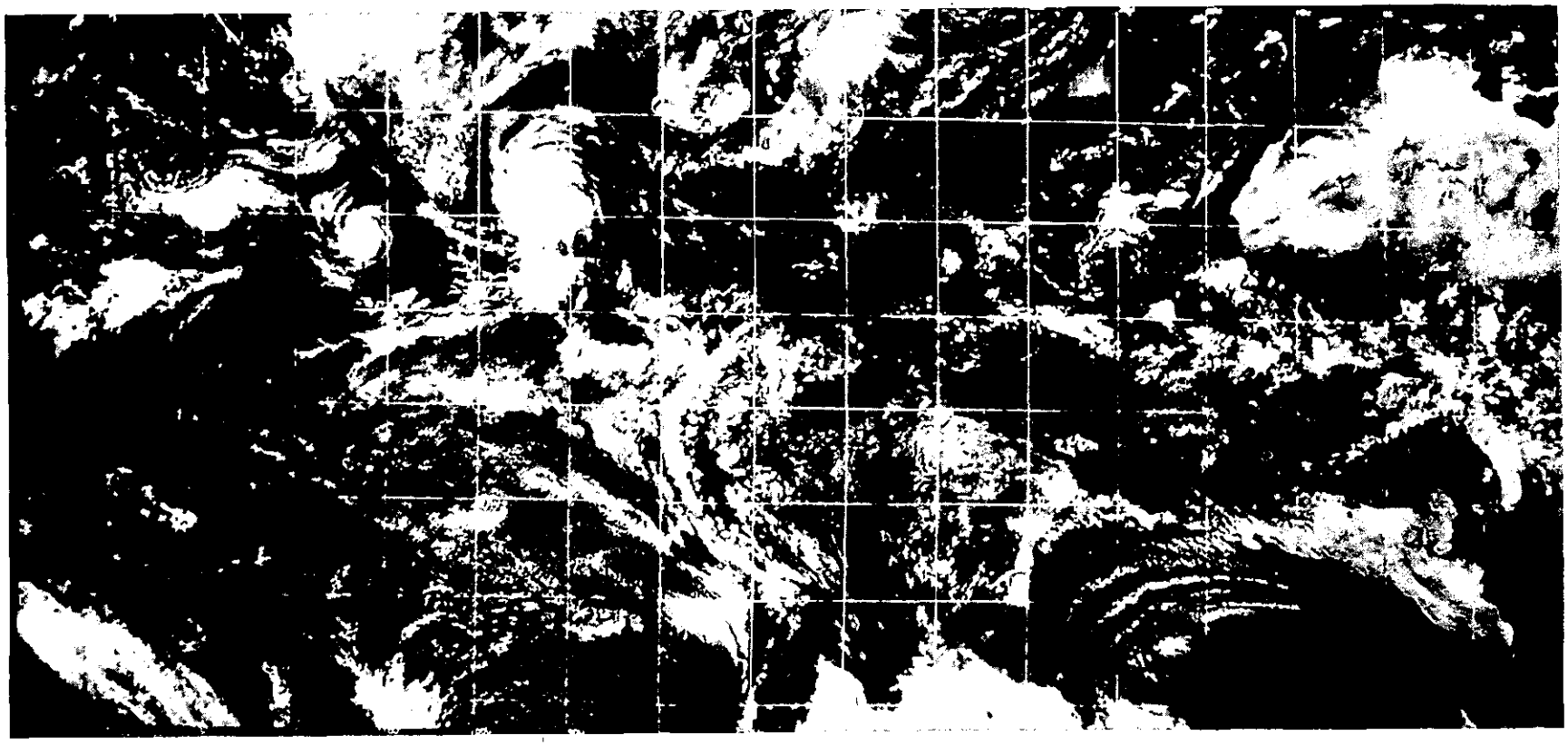

Figure 48. World satellite mosaic for September 18, 1967.

hemispheres. The one in the southern hemisphere shows several bands of clouds parallel to the front itself in the cold air. Bands are one of the most important cloud patterns that we shall discuss further. Other noteworthy cloud features on this picture are the eastern portion of the equatorial trough zone (the western portion has been carried away by the hurricanes) and a long array of large cumulus clouds piled up against the Andes Mountains by the sea breeze circulation on the west coast of South America.

Figure 49 shows the satellite-viewed cloud patterns of the record Atlantic hurricane of all times, namely Camille of August 1969. This storm killed 256 people and did 1.4 billion dollars damage. We can diagnose two of the main reasons for this storm's destructive intensity from the cloud patterns. The "hot" cumulonimbus towers are made visible in red in the picture by a photographic enhancement technique by Dr. Fujita. We see from their alignment that the low-level inflow into this storm was from the south, an unusual configuration which permitted exceptionally warm moist air to be incorporated into the storm as fuel. We see also that the cirrus outflow from the storm is to the east-northeast, into a strong jet stream which permitted a rapid exhaust of the heat generated by the storm engine. Satellite studies of hurricane cloud patterns have thus been a tremendous aid to both the hurricane forecaster and the hurricane researcher. The literature abounds with satellite studies of hurricane patterns; I have cited one example in reference 53. Considerable work has also been done on hurricane cloud patterns by

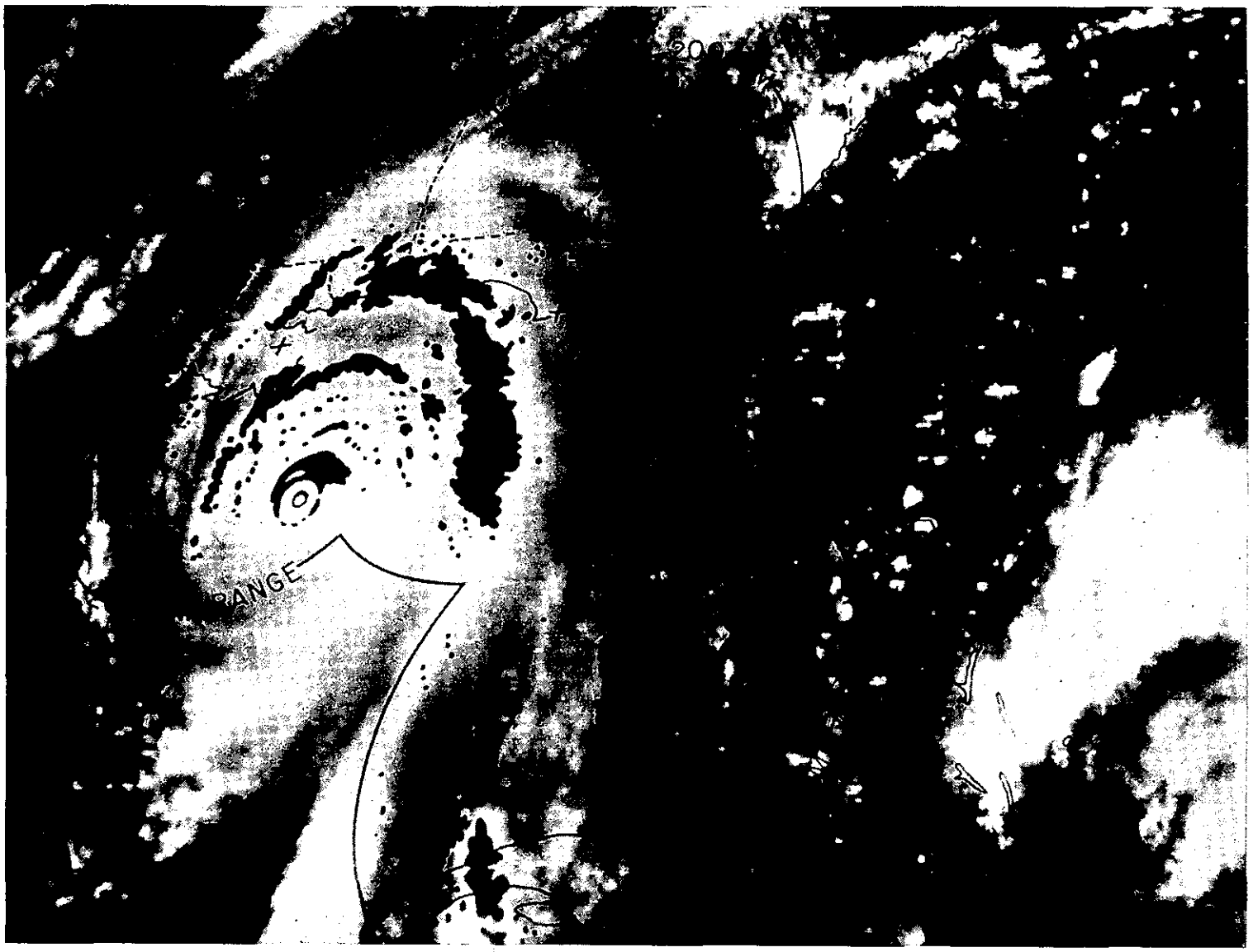

Figure 49. Satellite-viewed cloud patterns of hurricane Camille, August 1969.

aerial photogrammetry. The most complete of these, which shows how a single storm retains its "cloud fingerprint" over several days and stages of development is cited in reference 54. A final more intimate look at hurricane cloud patterns is obtained in figure 50, a photograph of Hurricane Gladys, 1968, made by the Apollo 8 astronauts. Here we are looking southeast from the Florida panhandle at the storm as it moves up the Florida west coast. Gladys was a minimum-intensity hurricane and had an incomplete eye wall and a poorly developed cirrus shield, which permits us to see the spiral bands of "hot towers". We can see that the main inflow is from the east and northeast, accounting in large part for the weakness of the storm.

Less spectacular than the hurricane, but 50 times more common and thus more important for boundary-layer dynamics, are the tropical wave disturbances we described earlier. These systems also have their characteristic cloud fingerprints, as illustrated in figure 51. Note that there is a strong suggestion of cloud bands deformed into a wave shape and that the location of the cirrus canopy indicates that convection is most developed eastward of the wave axis. Figure 52 shows the eight day history of a wave disturbance moving off Africa and across the Atlantic, which weakens as it enters the Caribbean, a not uncommon life history.

We will now leave synoptic scale cloud formations and progress down to the mesoscale and look at some special cloud patterns which develop in the atmospheric boundary layer. These are polygonal and banded patterns

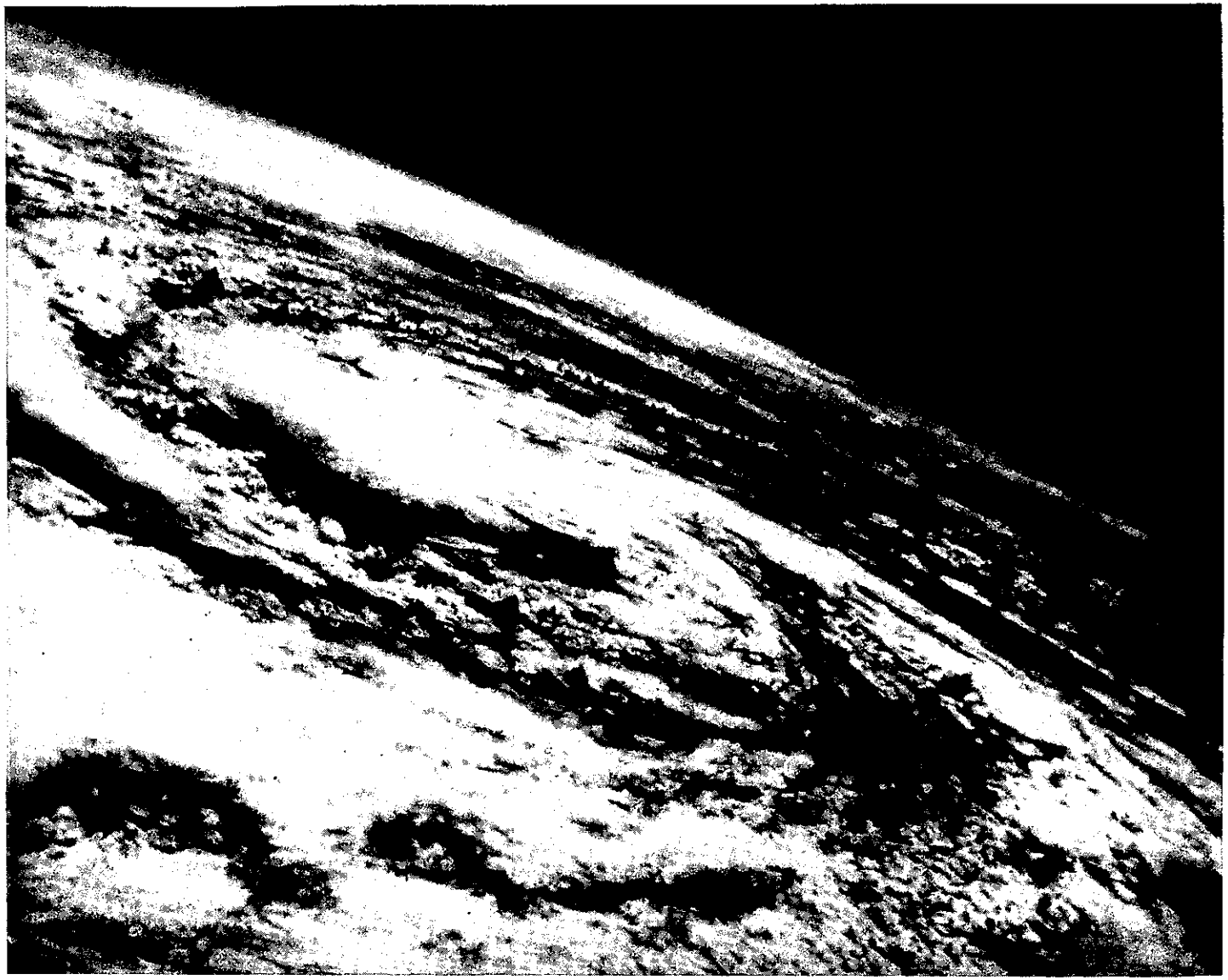

Figure 50. Photograph of hurricane Gladys, 1968, made by Apollo 8 astronauts.

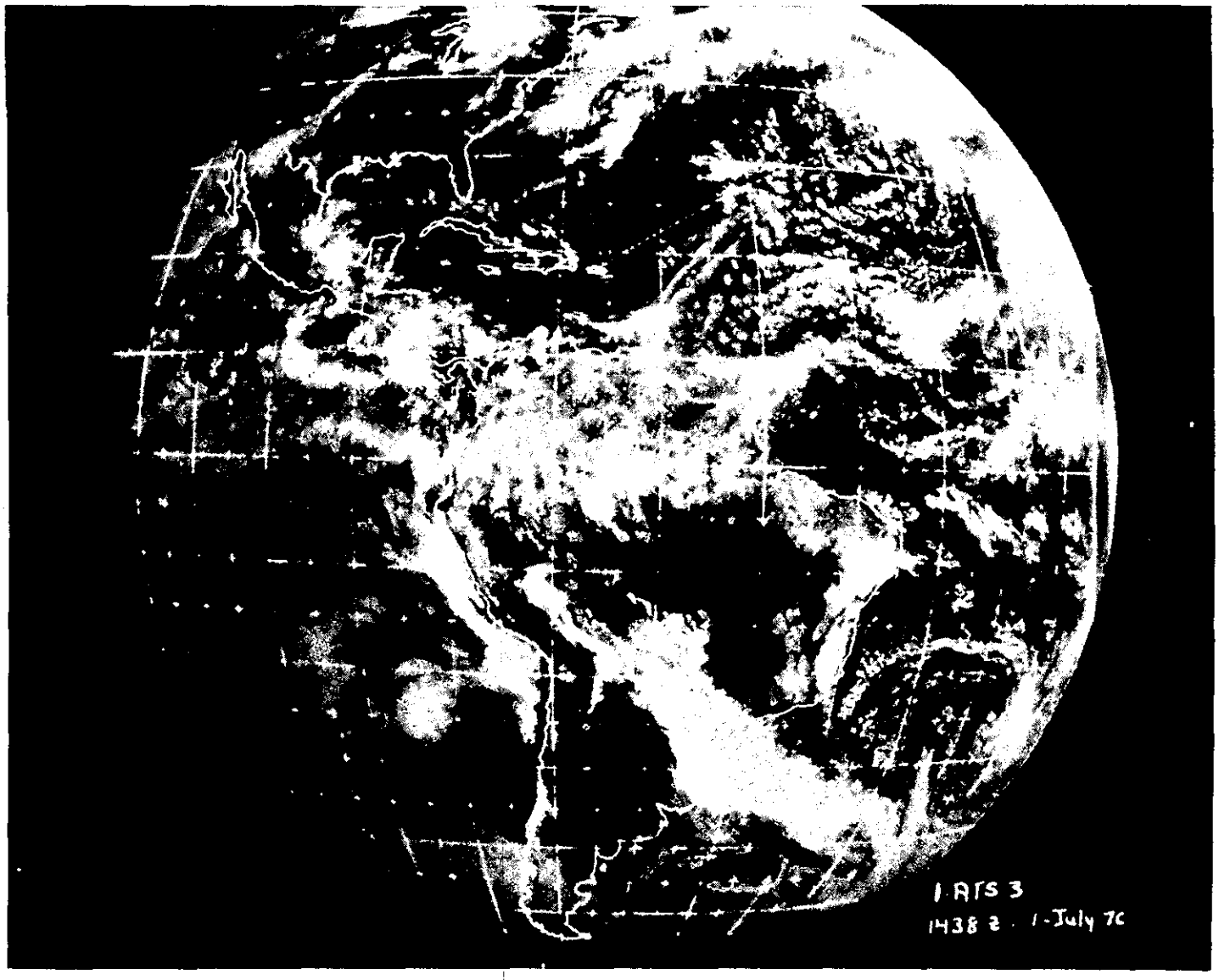

Figure 51. Satellite photograph illustrating typical tropical wave in the Atlantic.

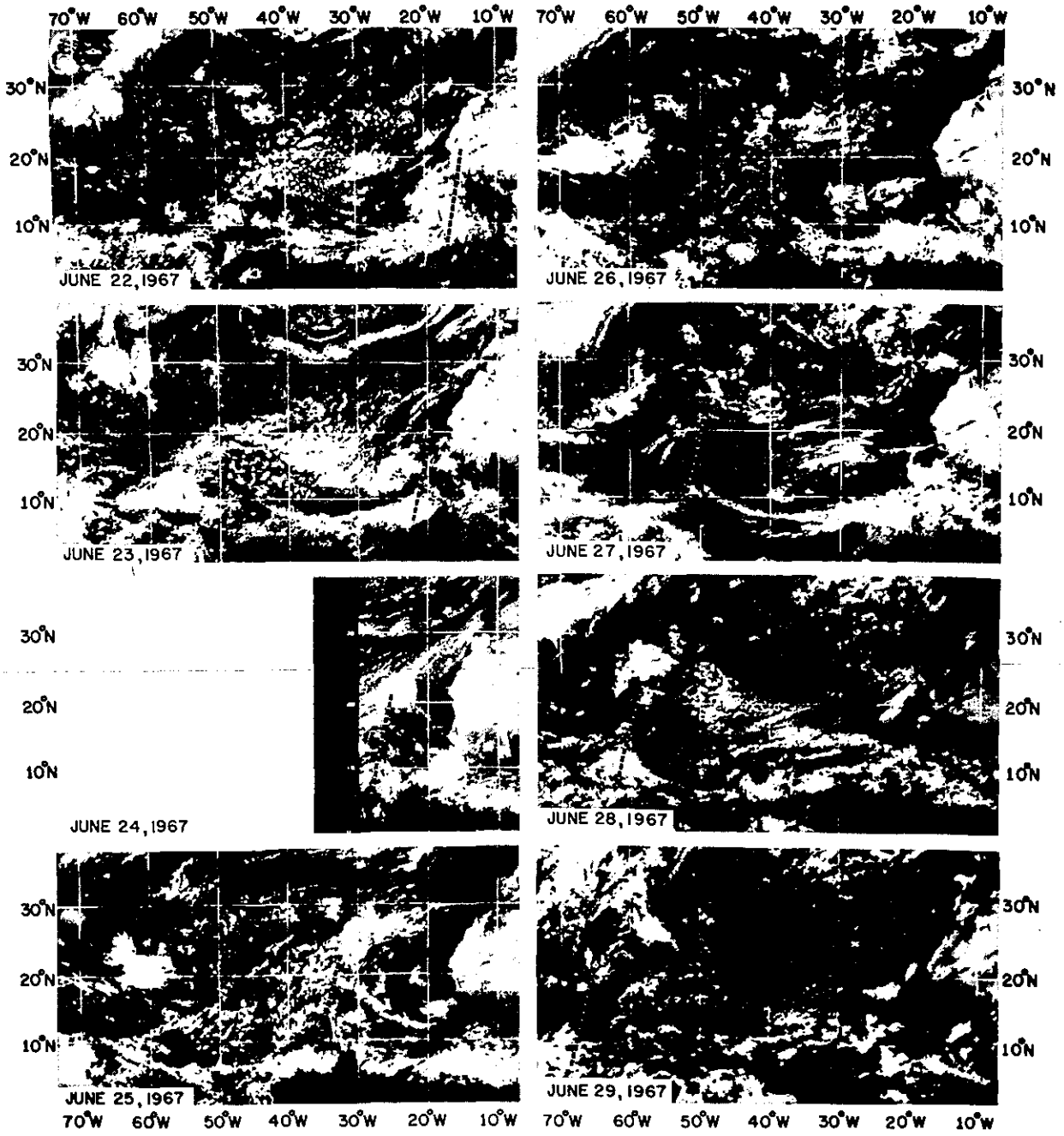

Figure 52. Eight-day satellite history of a tropical wave moving off Africa, June 22-29, 1967.

which are observed when the boundary layer is limited in vertical extent and strongly heated from below. These cellular cloud formations are particularly interesting because they have an apparent analogue in very carefully performed laboratory experiments and, moreover, the laboratory experiments have an accompanying theory which is rigorous and predicts both the criteria for the onset of the convection and the properties of the convection cells such as size and motions. A beautiful discussion of both theory and experiments is given in reference 28 and is only very briefly reviewed here in table 9. Probably everyone has seen the hexagonal Bénard cells which are produced in very shallow liquids, such as a layer of silver paint, when it is heated from below. The theory predicts, and experiments verify, that this mode of convection sets in when a certain non-dimensional number called the Rayleigh number esceeds a specified critical value. In the expression for Ra, α is the coefficient of thermal expansion, h is the layer depth, κ is the thermal conductivity and ν is the viscosity of the fluid. It must be emphasized that these are molecular coefficients and both the theory and laboratory experiments deal strictly with fluids in laminar motion. Below the critical Rayleigh number, the fluid accomplishes its heat transfer by molecular conduction alone. As the Rayleigh number is increased, usually by increasing Δ T which is the temperature difference across h, molecular transfer is not adequate, and the fluid begins to move - in cellular patterns. As the Rayleigh number is increased still higher, further transitions in convection regime occur to unsteady cells

Table 9

PATTERNED CONVECTION IN LABORATORY FLUIDS

ONSET CRITERION

$$R_a \equiv \frac{g \alpha \Delta T h^3}{\kappa \nu} > Ra_c$$

FOR A COMPRESSIBLE GAS

$$R_a \equiv \frac{g (\Gamma - \gamma) h^4}{T (\kappa \nu)} > Ra_c$$

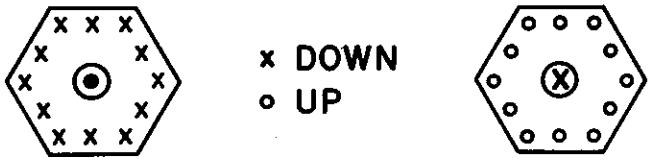

LIQUID GAS

RATIO $\frac{\text{DIAMETER}}{\text{DEPTH}} \sim 3\text{-}2:1$

and more complicated patterns with higher "modes" of motion. Several of these higher transitions have been studied both theoretically and in the laboratory as discussed in reference 55, but there is as yet no theory of fully turbulent convection, nor, to my knowledge, have simple polygonal cells been observed in a fully turbulent laboratory fluid. It is indeed a fascinating paradox that simple polygonal cells are very often observed in the fully turbulent atmosphere. Many meteorologists have attempted to carry over the Rayleigh theory to the atmosphere by analogy, using eddy conductivity and viscosity in the equations in place of the molecular coefficients. This is a controversial exercise because the eddy coefficients are bound to be determined by the convection itself and to vary between the ascending and descending portions of the cells. In general, one can justify putting in almost any coefficients necessary to get out the answer desired. And one certainly cannot take predetermined values of the eddy coefficients to predict the dimensions of the cells, although it may possibly be meaningful to take the observed dimensions of the cells to infer what the mean eddy transfer coefficients must have been.

The next interesting paradox posed by the atmospheric cells relates to the locations of the upward and downward motions. In a laboratory liquid, the ascent is in the center and descent is found at the cell walls, while in gases the reverse is the case. In the atmosphere, we find both types of cells. In a detailed discussion of this subject [51] Hubert proposes that the direction of circulation in mesoscale cells is determined by the vertical

variation of eddy viscosity. This is in analogy with the laboratory experiments and the theory behind them. In a gas, the molecular viscosity increases with temperature and hence decreases upward in the convecting fluid, while in a liquid the viscosity decreases with temperature, and hence with height, when the fluid is heated from below. The height gradient of viscosity has been shown to control whether the ascent is at the cell center or at the edges.

The diameter to depth ratio is predicted and checked by measurements in the laboratory cells; the cell widths vary between about two to three times the layer depth. Another interesting paradox will appear when we examine the width to depth ratio in the atmosphere.

Figure 53 shows, in a laboratory case, that when a weak translational motion is superposed on the convecting fluid, the cells begin to stretch out into rolls lined up parallel to the direction of the shear between the fluid and its boundaries, or along the direction of the flow itself. Here the region is about 40 cm across, so that the cell width is about 4 cm. The layer depth is 20 mm, so that the width-to-depth ratio is about two to one.

Figure 54 shows schematically the two kinds of cell patterns observed by satellite, illustrating Hubert's hypothesis about the height gradient of viscosity.

Figure 55 shows a satellite photograph of "open" cells. Numerous such cases have been carefully documented in references 48 and 51 and the documentation brings to light further paradoxes. Firstly, the horizontal

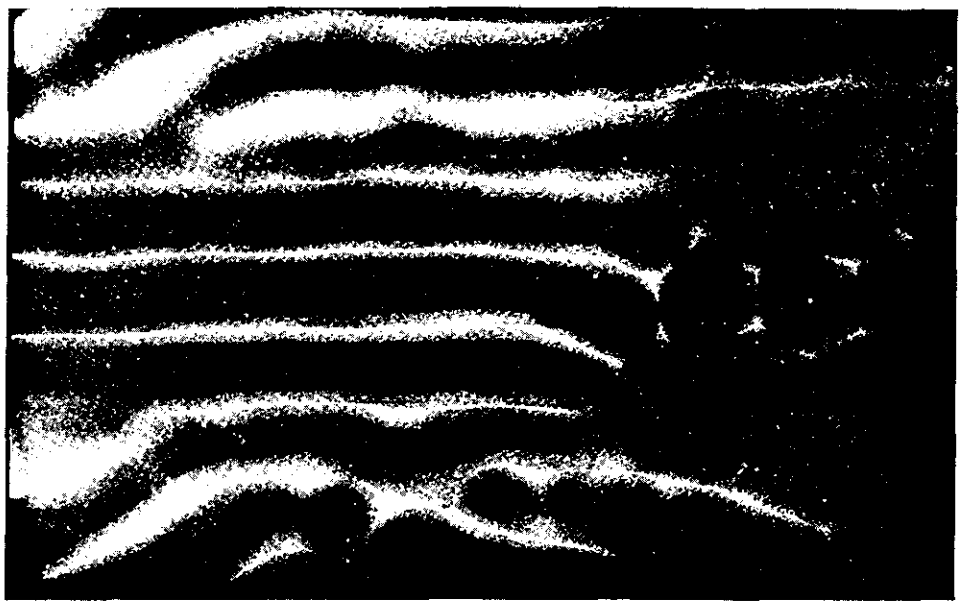

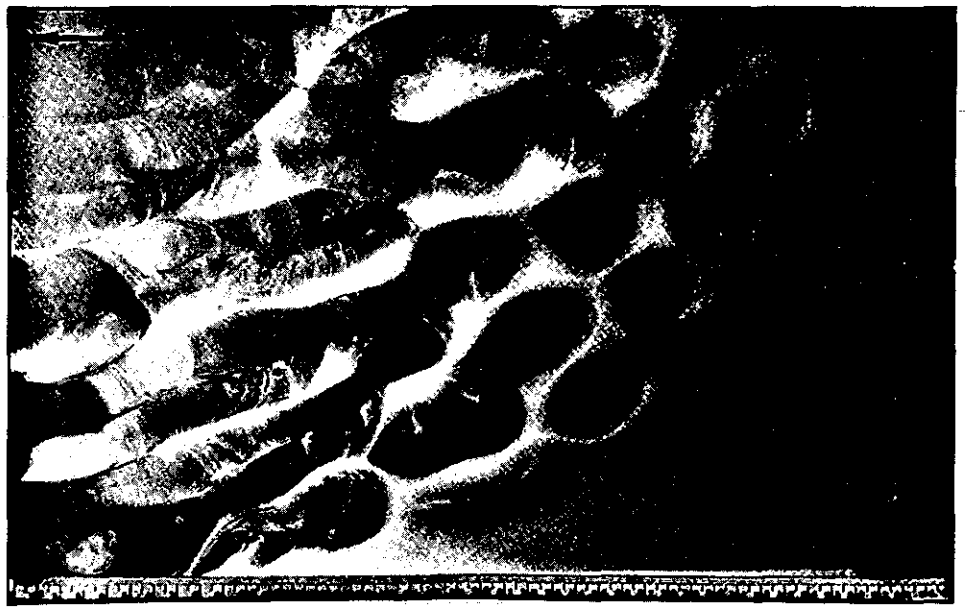

Figure 53. Experimental transformation of polyzonal cells into longitudinal bands, by the setting in motion of a layer of air heated from below. Depth of layer 20 mn. (After Avsec.)

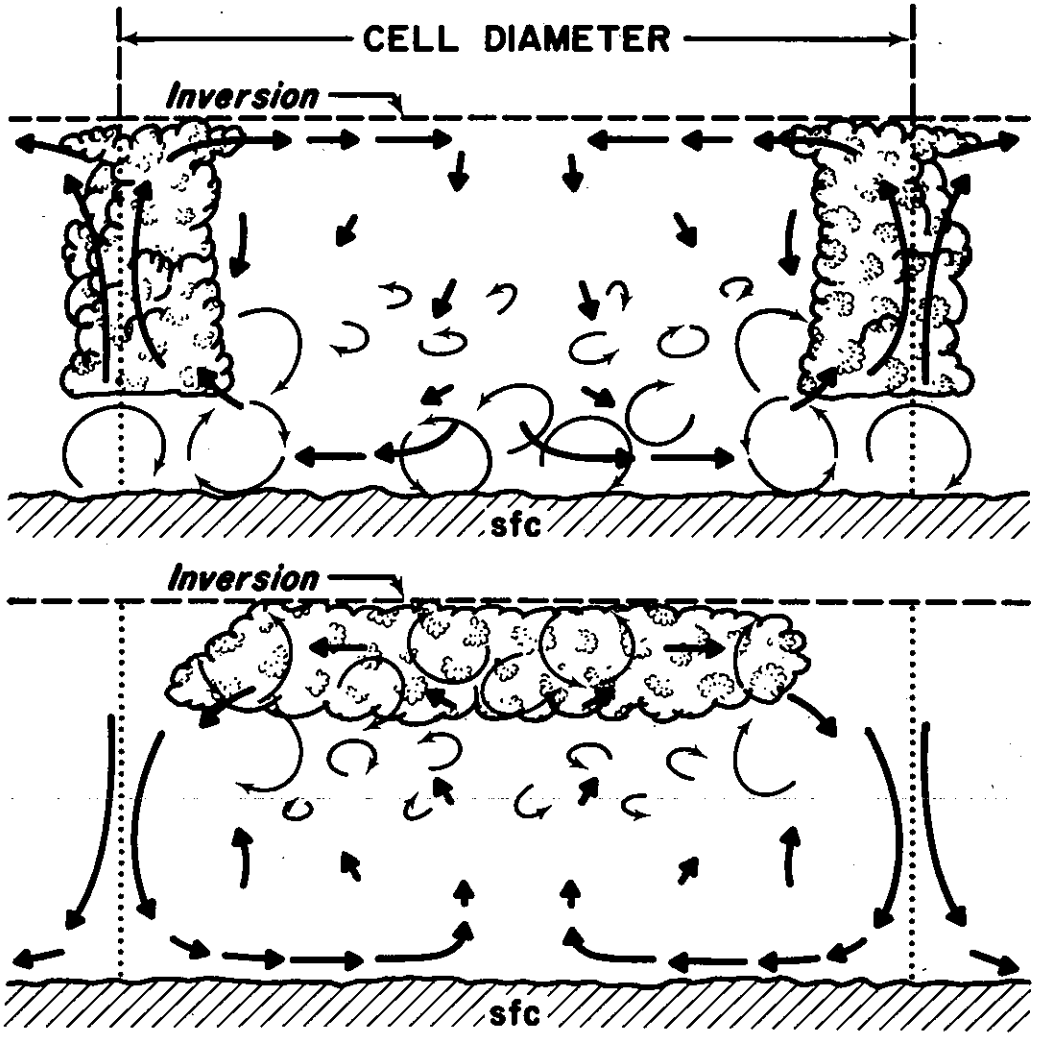

Figure 54.

Cross section of open and closed cells. Mesoscale cellular circulation in heavy arrows, turbulent motion in light arrows. Large diameter eddies-strong mixing, small eddies-weak mixing. (After Hubert.)

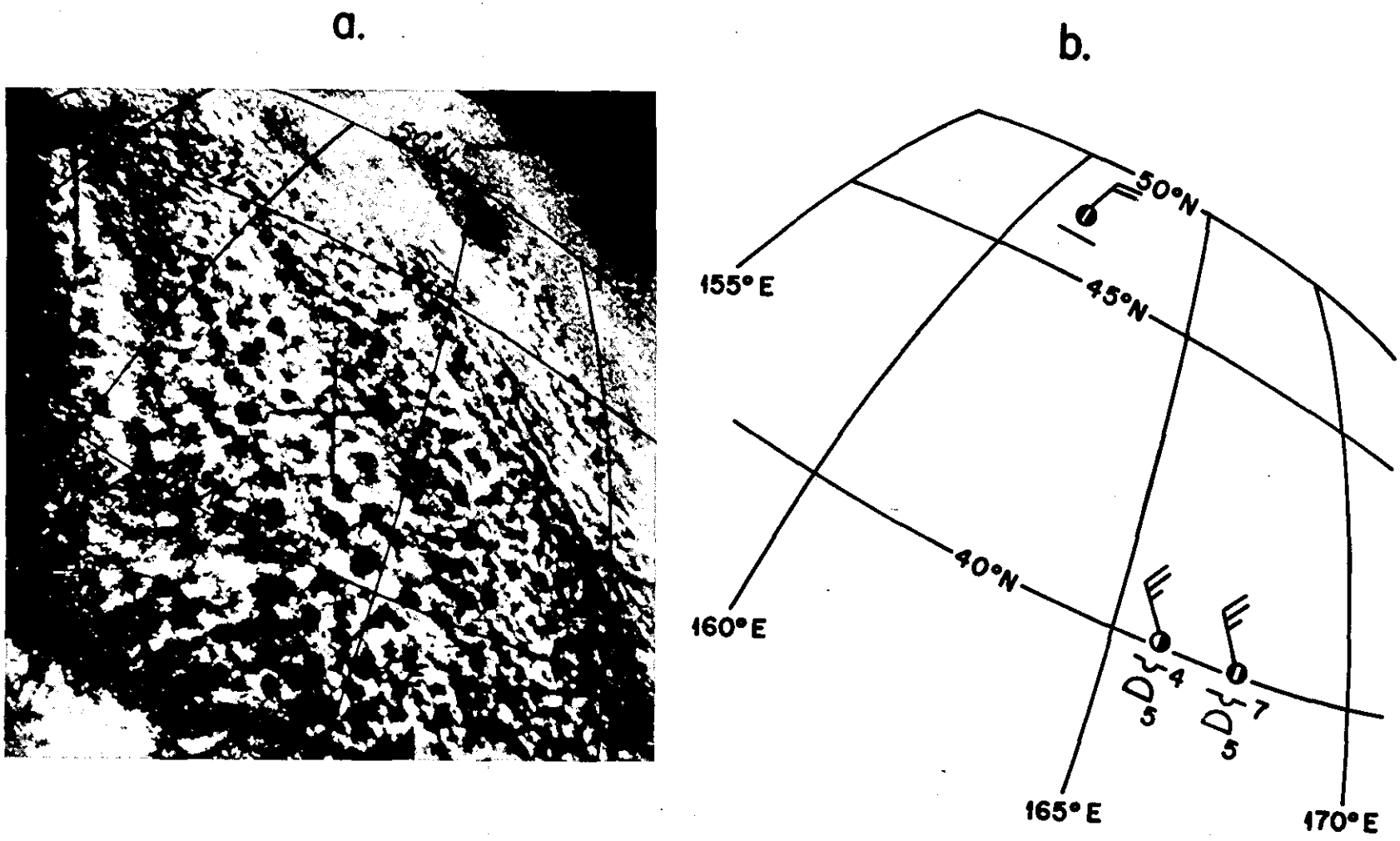

Figure 55. Satellite photograph of open cells. Tiros VII, 11 January 1964.

cell size here ranges from 18 km to 58 km, with a median size of 35 km. The depth of the convecting layer is about 2 km, so the width to depth ratio averages nearly 18. Of all satellite open cell cases studied, the median width to depth ratio was 30. Then we have the problem of the quite strong wind speed where the fluid is translating rapidly over the heated lower boundary. Why are the cells not drawn out into rolls? It is true we see some pronounced banding along the wind direction, but this is of a larger scale than the individual cells which are distinctly recognized. A possibility is that the convecting layer consists of just the cloud layer and that the convective motions do not extend down to the sea surface. This would be important but difficult to find out.

Figure 56 shows a case of "closed" cells in stratus and stratocumulus off the California coast. The center-to-center distances range from 37 km to 110 km, with median 72 km. The depth of the convective layer is not known but could not have exceeded to 2 km.

Let us now progress still farther down the size scale and take a look at cloud patterns too small to be resolved on the satellite pictures but which show up very beautifully on the photographs taken by the manned spaceflights. Figure 57 is a photograph from Gemini 5 at about 2 pm local time on August 23, 1965 looking at the north coast of Cuba. It shows open hexagonal cells 5 to 10 km across. Estimating a convective layer depth of 2-3 km, we find here that the laboratory ratio of diameter to depth is well repro-

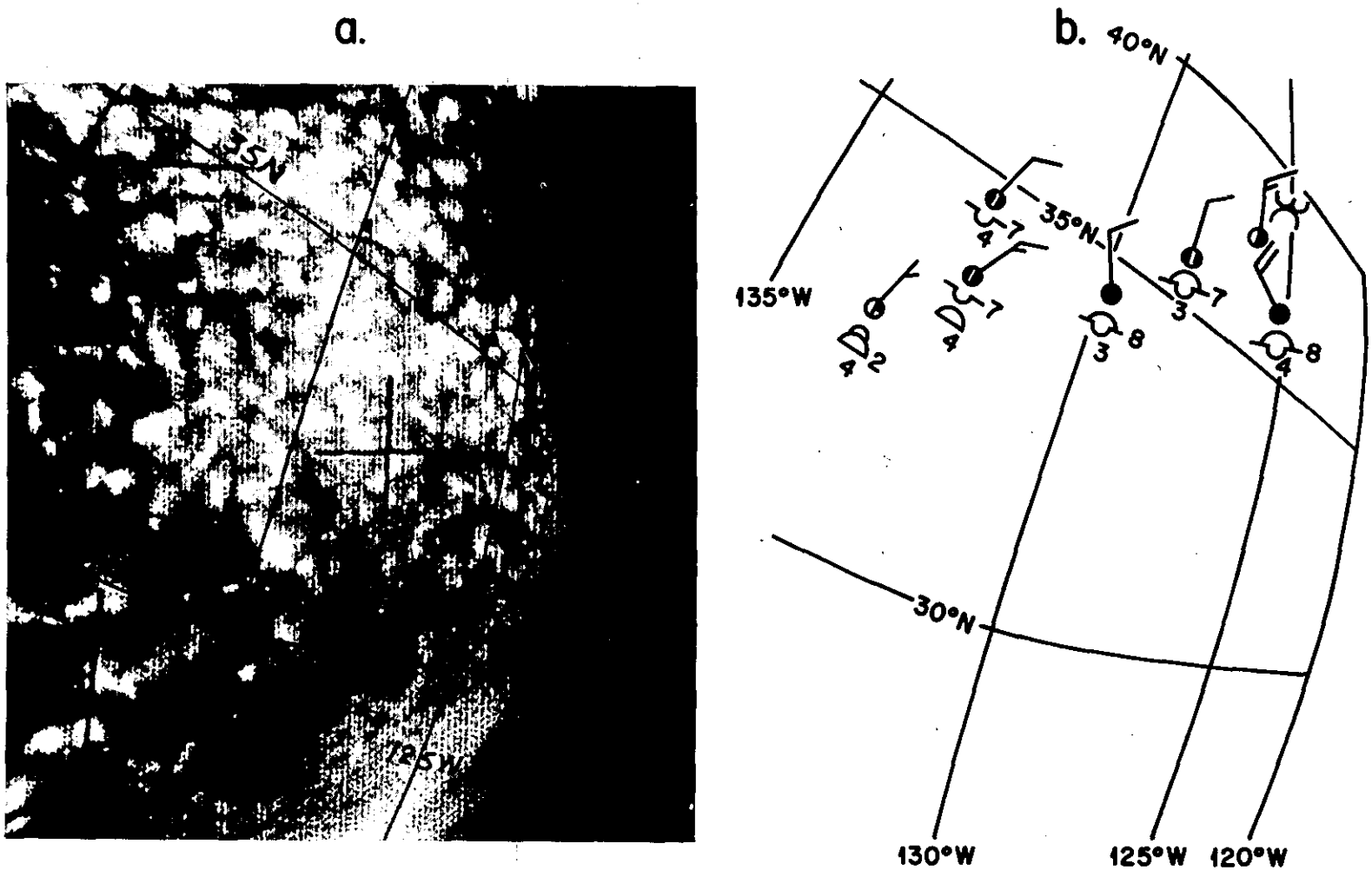

T-VI 4179D 2030GMT 1 JULY 63

Figure 56. Satellite photograph of closed cells. Tiros VI, 1 July 1963.

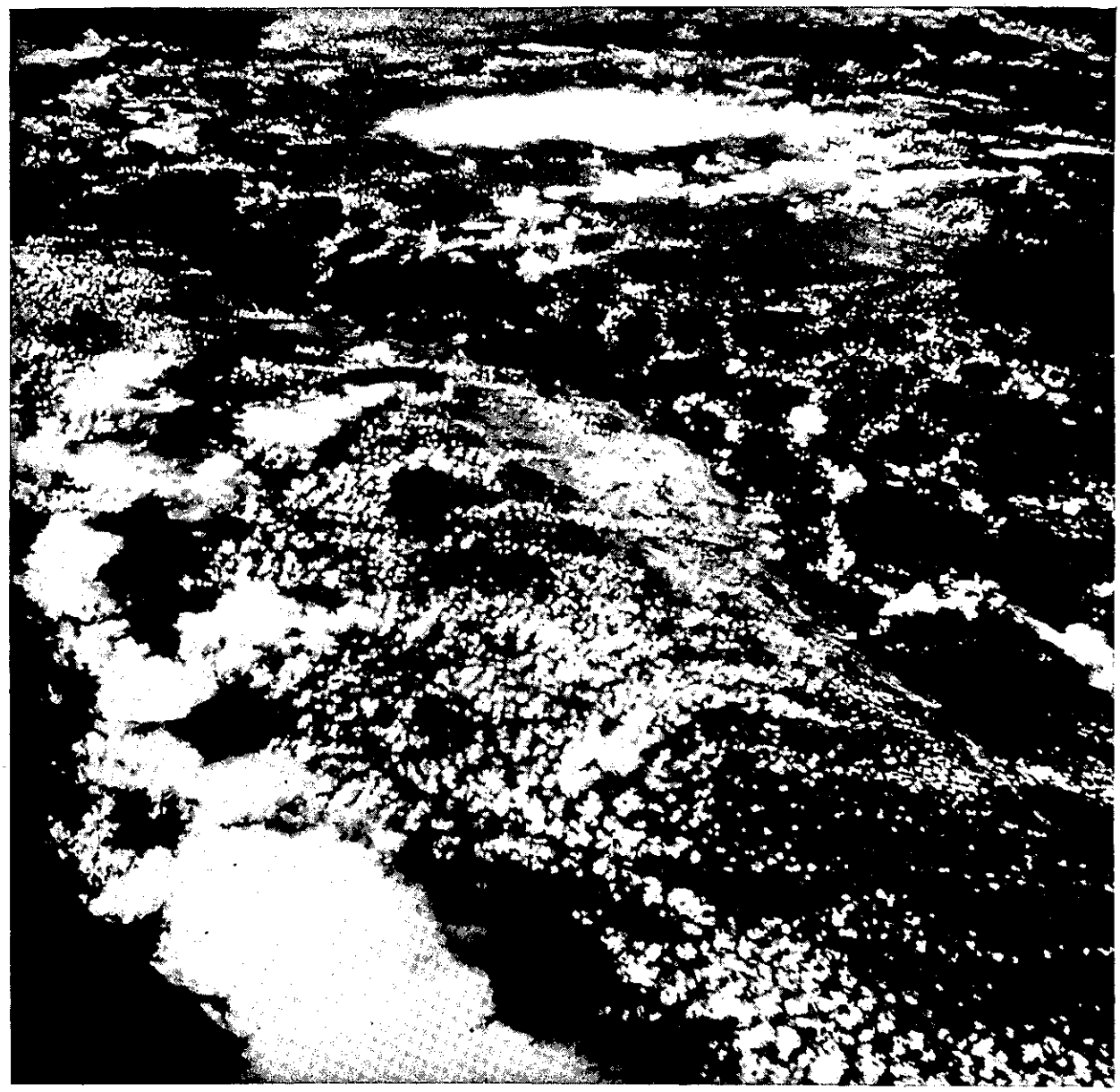

Figure 57. Gemini 5 photograph of hexagonal cloud patterns near Cuba. 23 August 1965.

duced in the atmosphere.

Figure 58 shows closed cells southwest of the Canary Islands photographed from Gemini 6 at 1042 GMT on December 16, 1965. The narrow gaps of descent between cells are too small to be resolved by satellite photography.

The next four pictures (figs. 59-61) show patterns photographed on a single traverse of the tropical Atlantic just east of Barbados. They were taken by the Apollo 10 astronauts in May, 1969 and each picture covers a width of about 200 km.

In figure 62 we have a fairly common and particularly interesting and informative cloud formation. At first it looks just like two rows or bands of clouds about 75 km or roughly 40 miles apart. On a closer look, we see that the actual cloud rows are about at right angles to the bands and that these are 10 km or less apart. The bands are created because of alternate enhancement and suppression of the rows. From aircraft mapping of oceanic clouds we have learned that these patterns arise when the wind and the shear are at right angles to each other. In this picture, the small clouds rows are lined up with the low-level wind, that is, with the shear between the boundary layer and the lower boundary surface, while the bands are oriented with the shear within or across the top of the cloud layer. We presently have no theory or explanation of why this is so.

Let us pursue this fascinating topic of cloud organization by

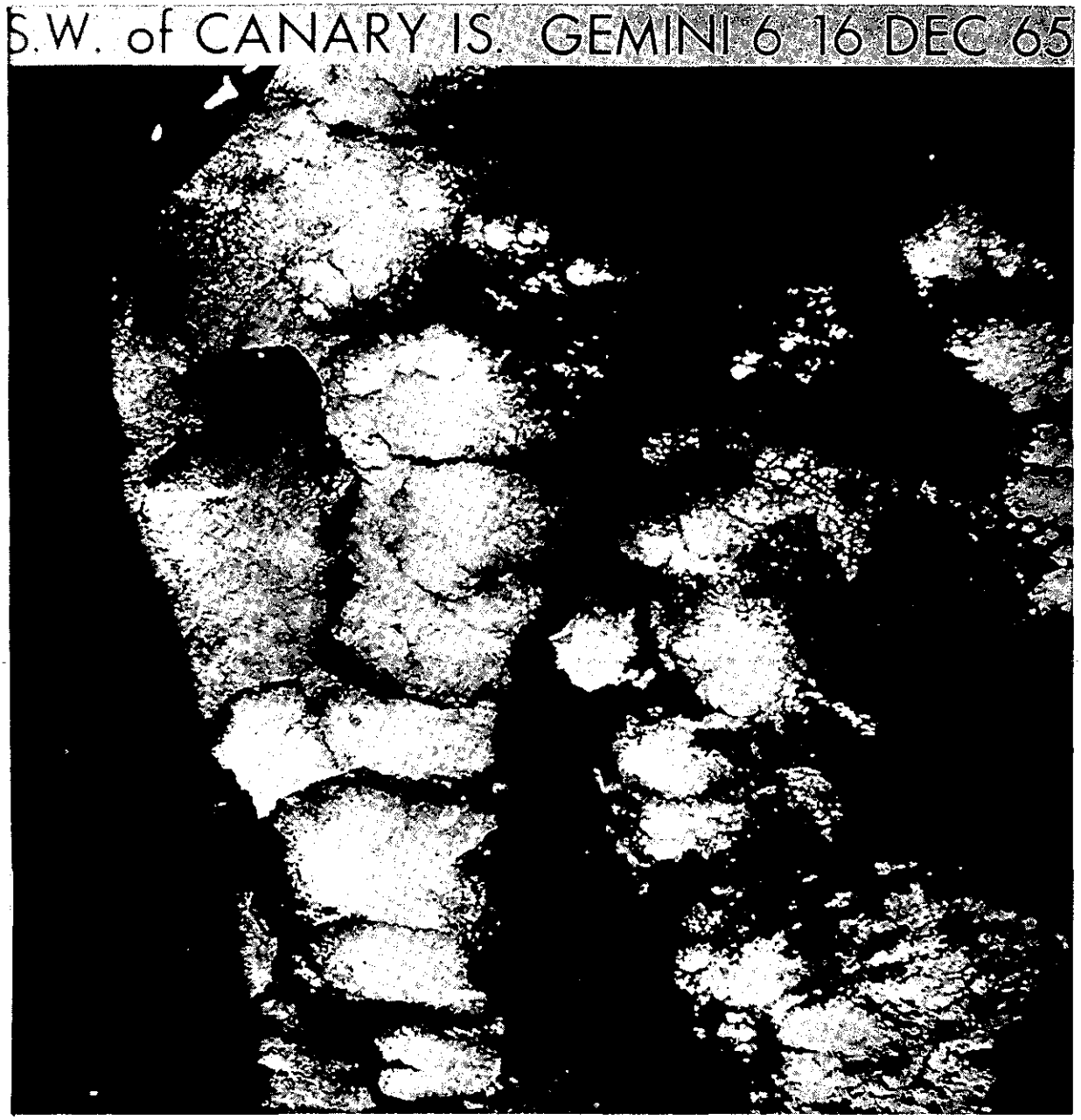

Figure 58. Closed cells southwest of the Canary Islands. Photographed by Gemini 6 at 1042 GMT, December 16, 1965. (After Hubert.)

Figure 59. Apollo 10 picture east of Barbados, May 1969. Open cells, about 20 km across lined up in rows roughly parallel to the wind.

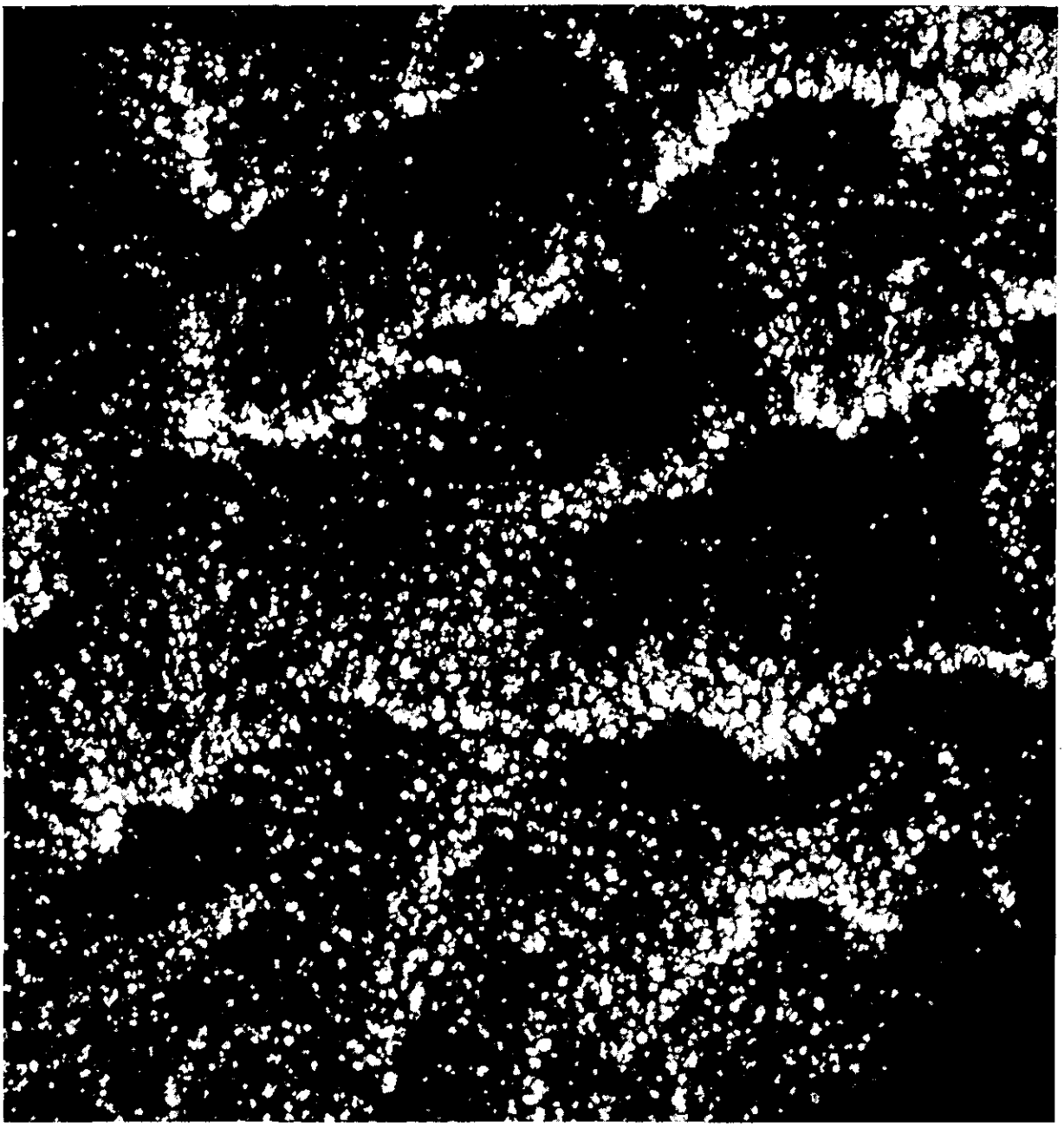

Figure 60. Apollo 10 picture east of Barbados, May 1969. Scale about 200 km.

Figure 61. Apollo 10 picture east of Barbados, May 1969. Scale about 200 km.

Figure 62. Apollo 10 picture east of Barbados, May 1969. Scale about 200 km. Bands creasted because of alternate suppression and enhancement of rows (see text).

coming down out of space and looking more closely at cloud patterns by aircraft. We have done many years of work on mapping cloud patterns by aerial photogrammetry. This work is presented in reference 45. I will just summarize the highlights here. Let us first take a look at some typical cloud configuration as seen from an aircraft, (figs. 63-66).

The flight tracks along which cloud maps were made are shown in figure 67. Three such complete circuits of the tropical Pacific Ocean were made in the summer of 1957. They were made on military aircraft flying at 11,000 ft. Time lapse movies were made at exactly one frame per second and cloud maps were constructed using a photogrammetric technique described in references 45 and 46. Local wind, radiosonde and synoptic information were used to interpret the cloud maps wherever these data were available.

Let us look at rows of small cumulus clouds. The simplest situations are like those shown in the photograph and on the map in figure 68 where there is only one orientation of clouds and these rows are parallel to the low level wind. We call this the "parallel mode" of organization. Our study shows that it prevails when the wind and shear are in the same plane; we hypothesize that the rows come into being following the scheme shown in figure 69.

A more complex pattern of cloud rows is shown in figure 70. It is unlikely that one could deduce the correct wind direction from this

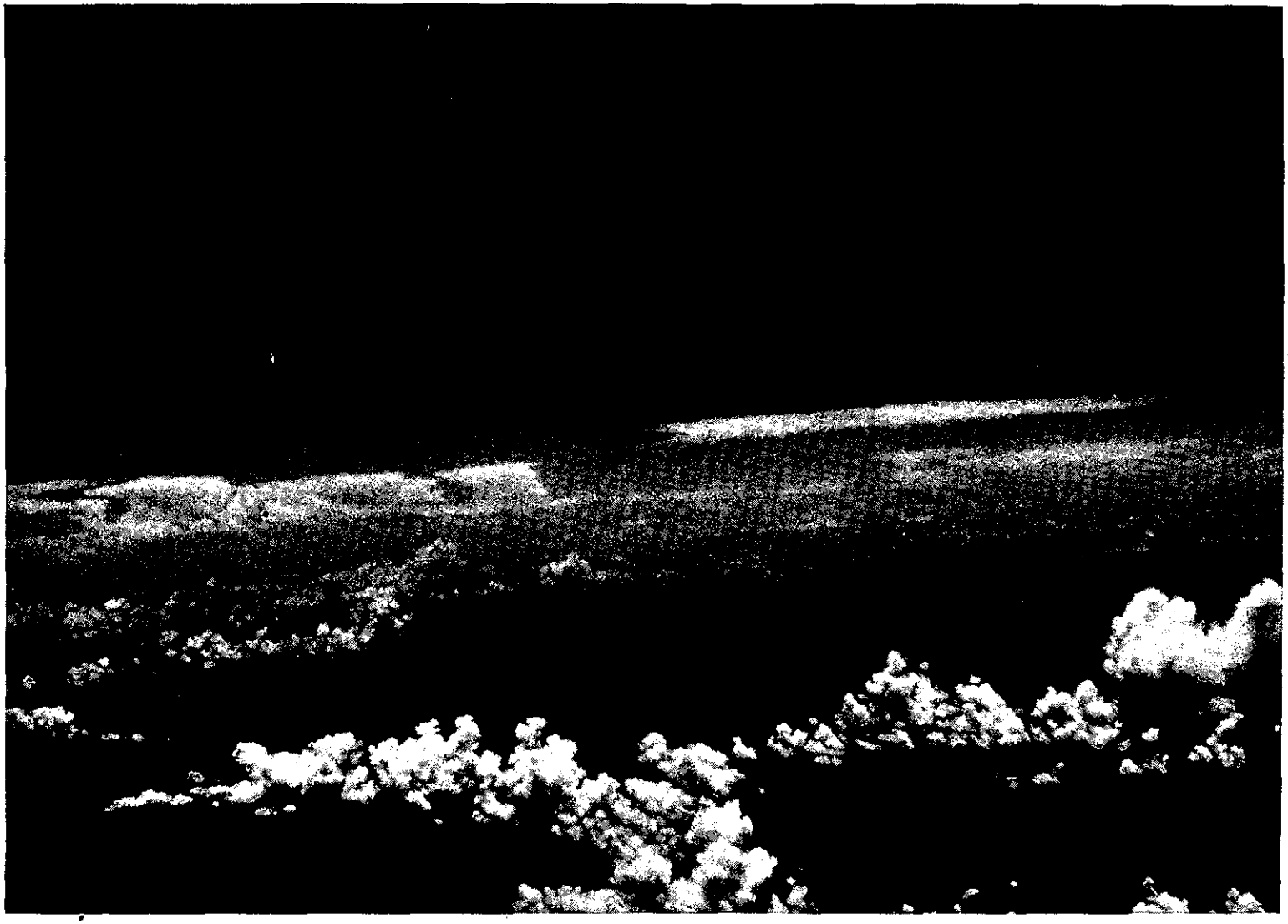

Figure 63. Aerial photograph of edges of open cells.

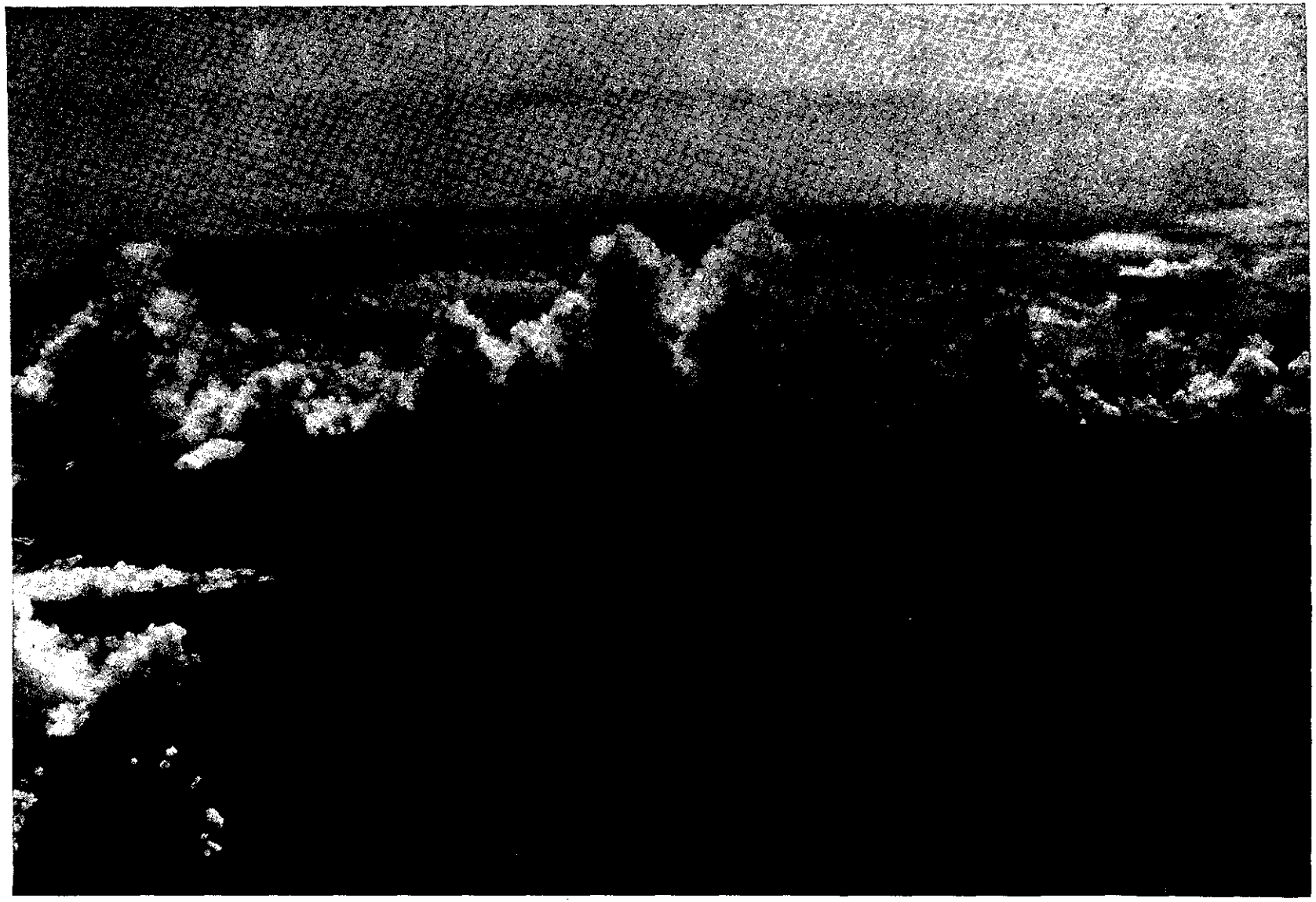

Figure 64. Aerial photograph of clear zone about 30 miles across surrounded by half ring of clouds.

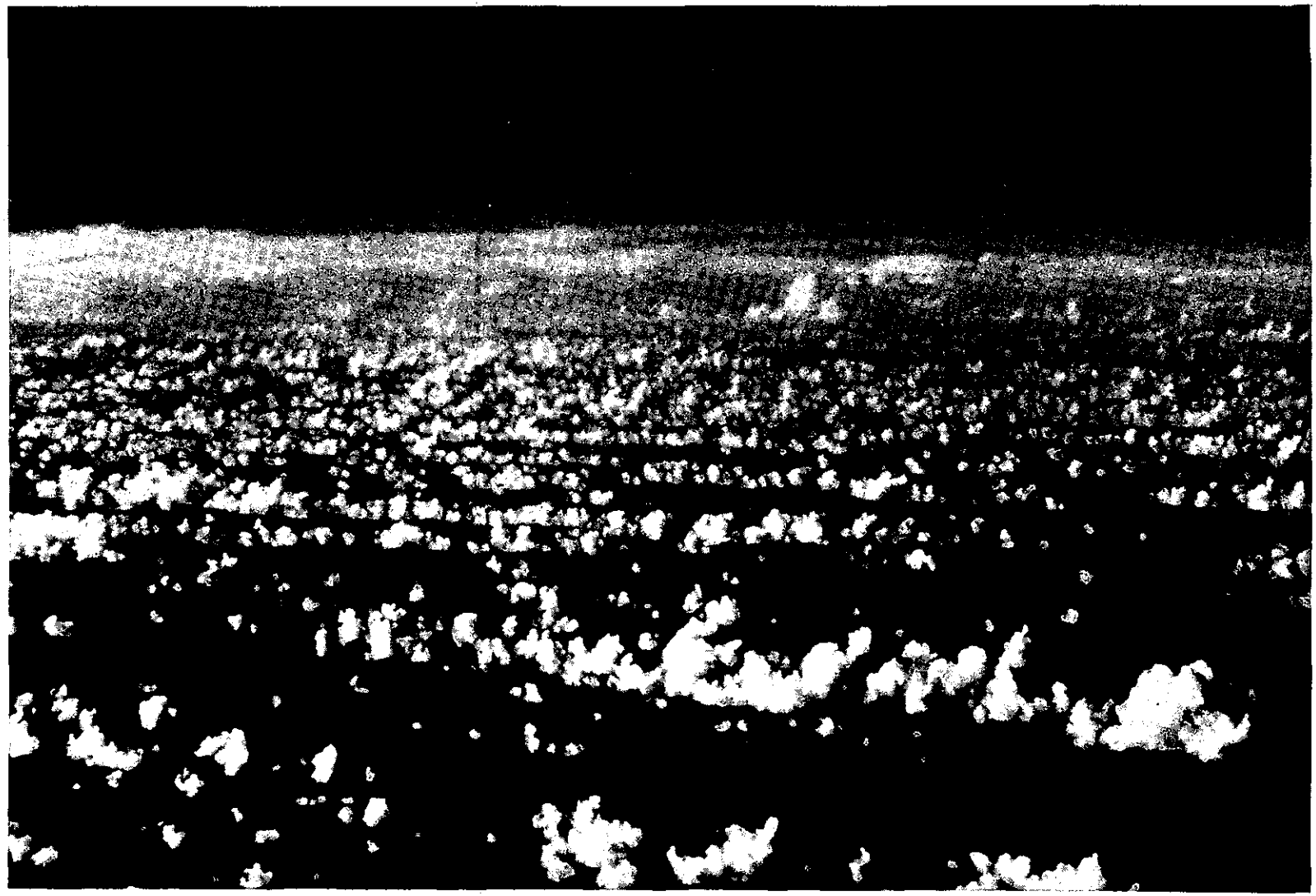

Figure 65. A typical aerial picture of simple cloud rows.

Figure 66. A typical aerial picture of "hot towers" in the equatorial trough zone.

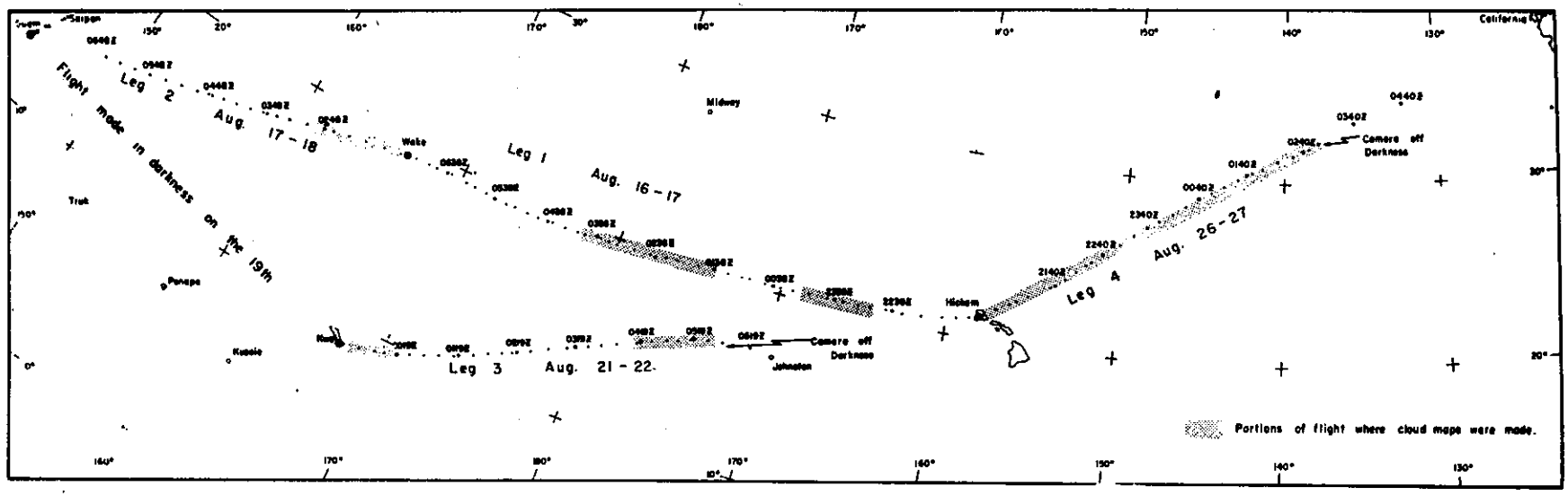

Figure 67. Flight tracks along which aerial cloud mapping was undertaken in 1957.

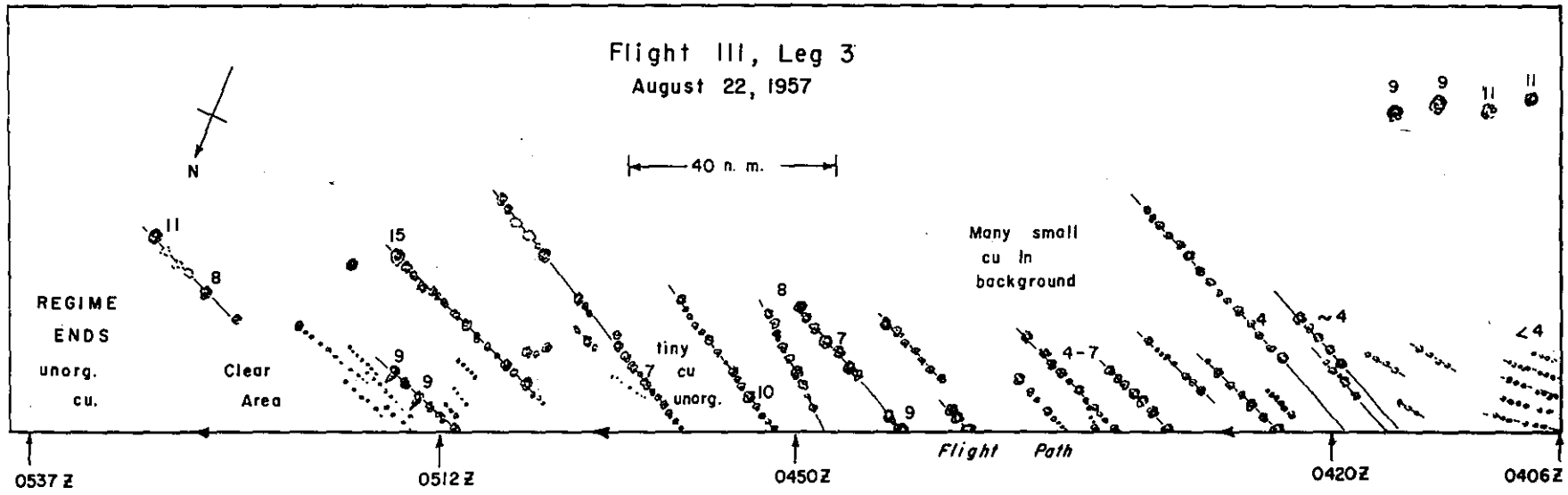

Figure 68. Map of simple cloud rows, made from aerial photographs.

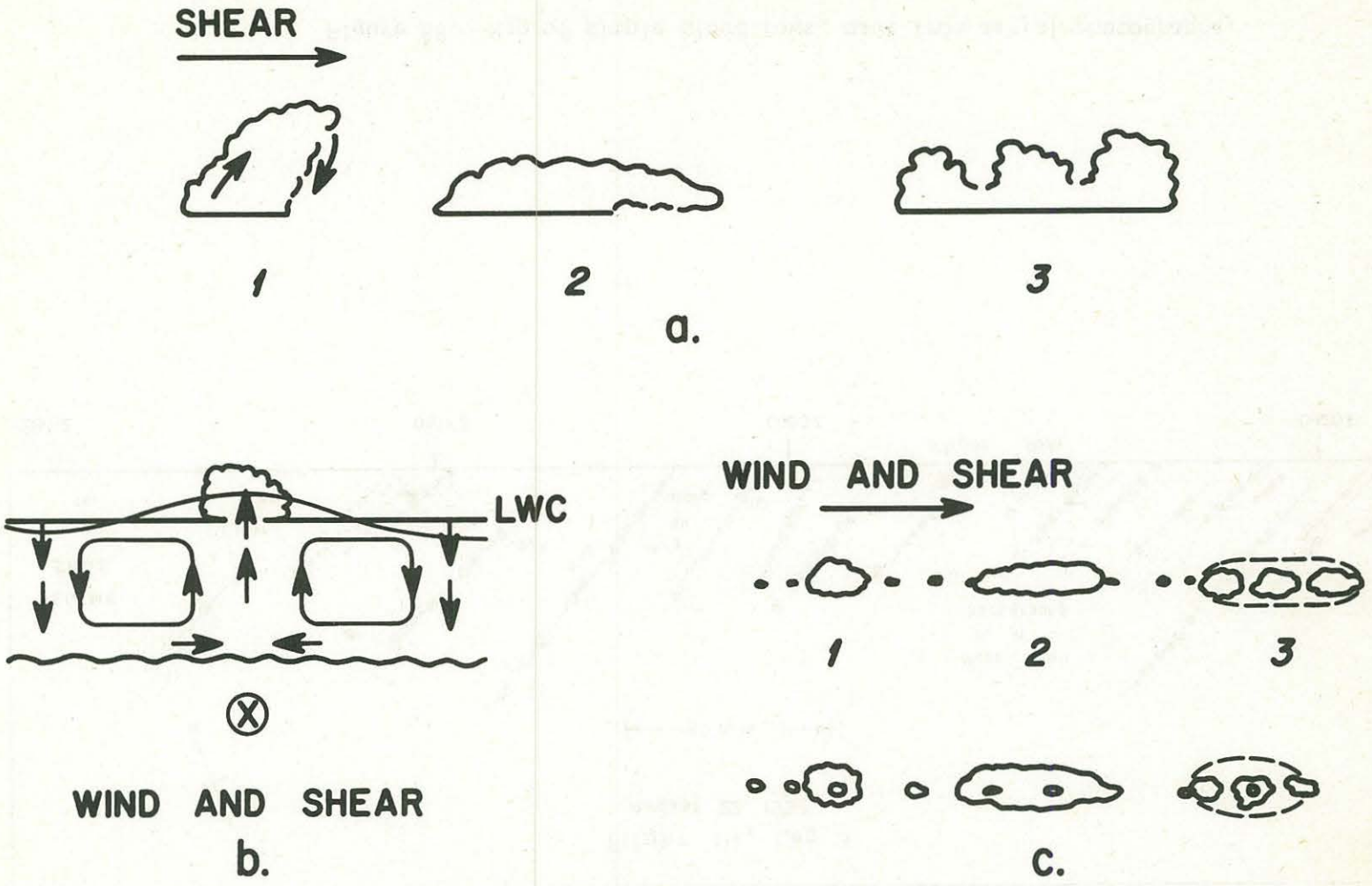

CUMULUS ROW FORMATION
WHEN WIND AND SHEAR IN SAME PLANE

Figure 69. Schematic illustration of hypothesis explaining simple cloud rows.

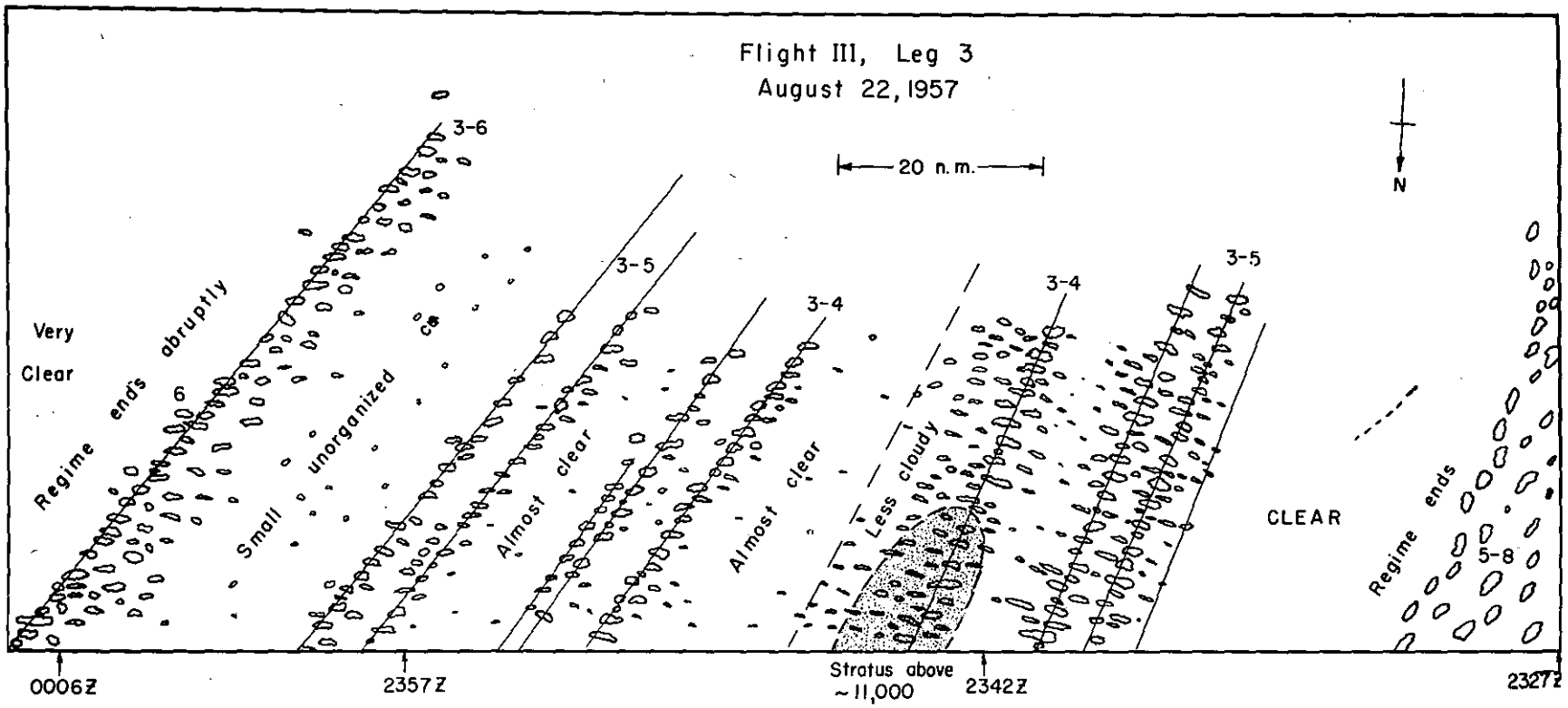

Figure 70. Map of cross-wind mode of cloud patterning, made from aerial photographs.

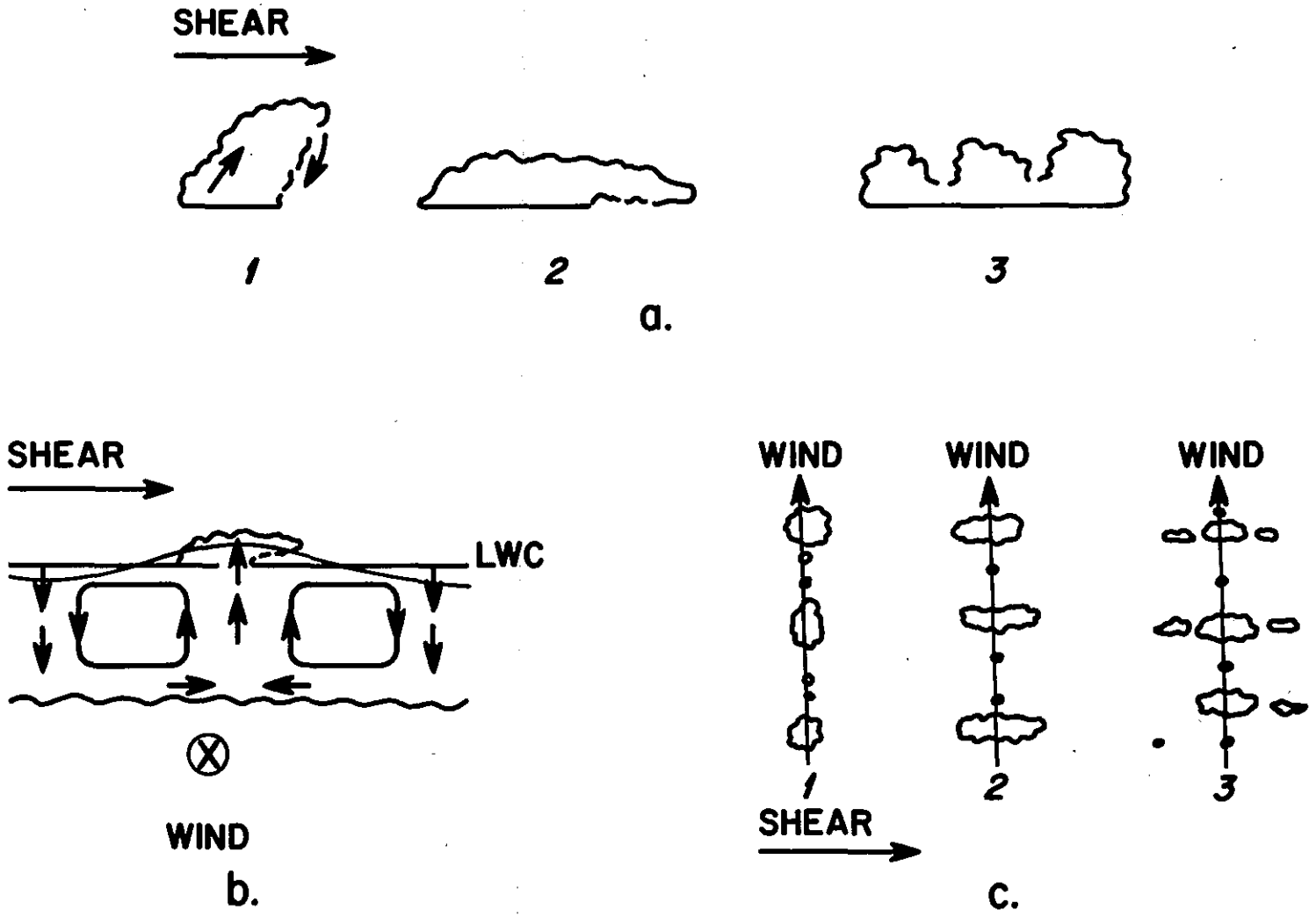

CUMULUS ROW FORMATION
WHEN WIND AND SHEAR AT RIGHT ANGLES

Figure 71. Schematic illustration of hypothesis explaining cross-wind mode.

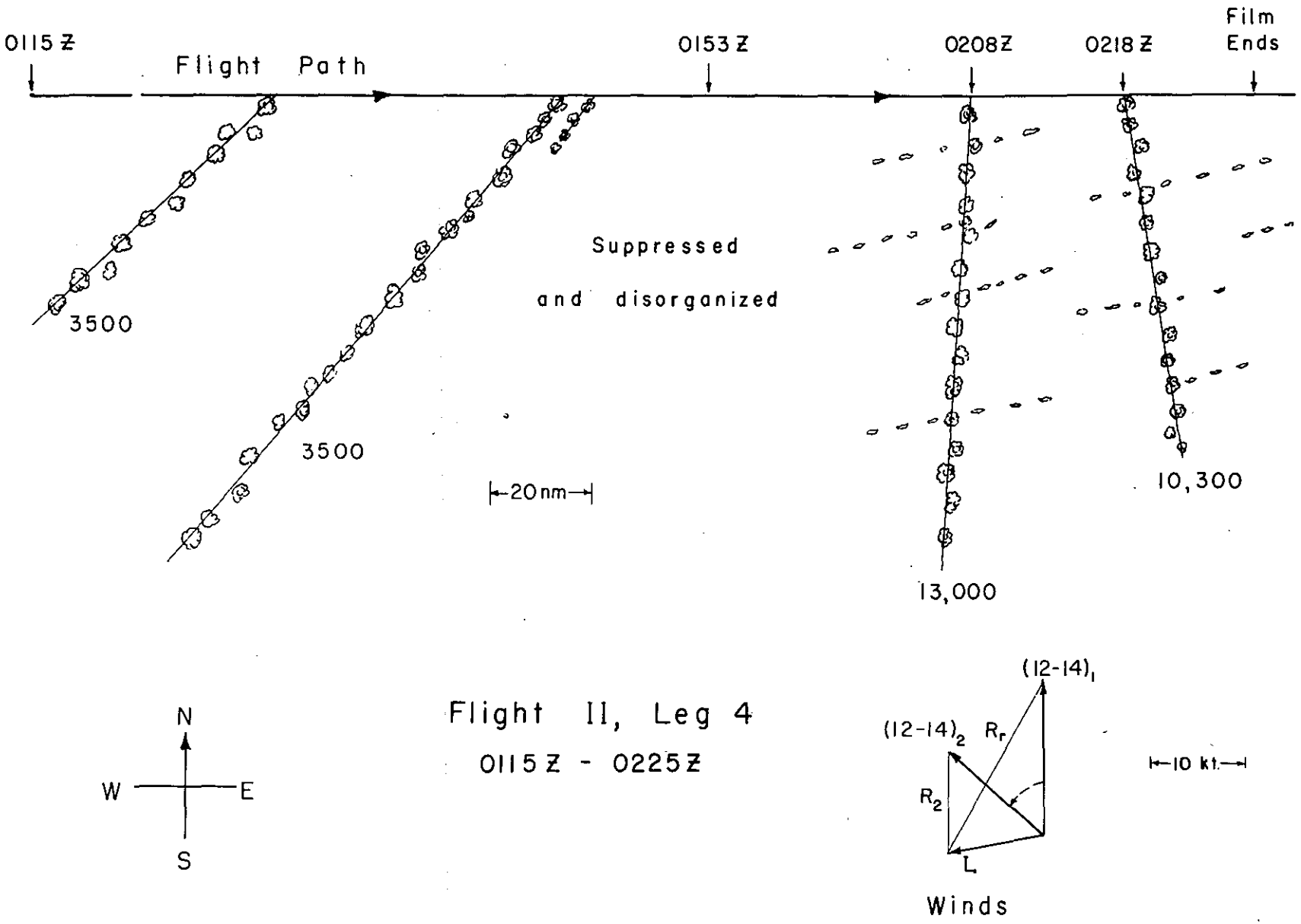

Figure 72. Map of cross-wind mode of cloud patterning (alone), made from aerial photos.

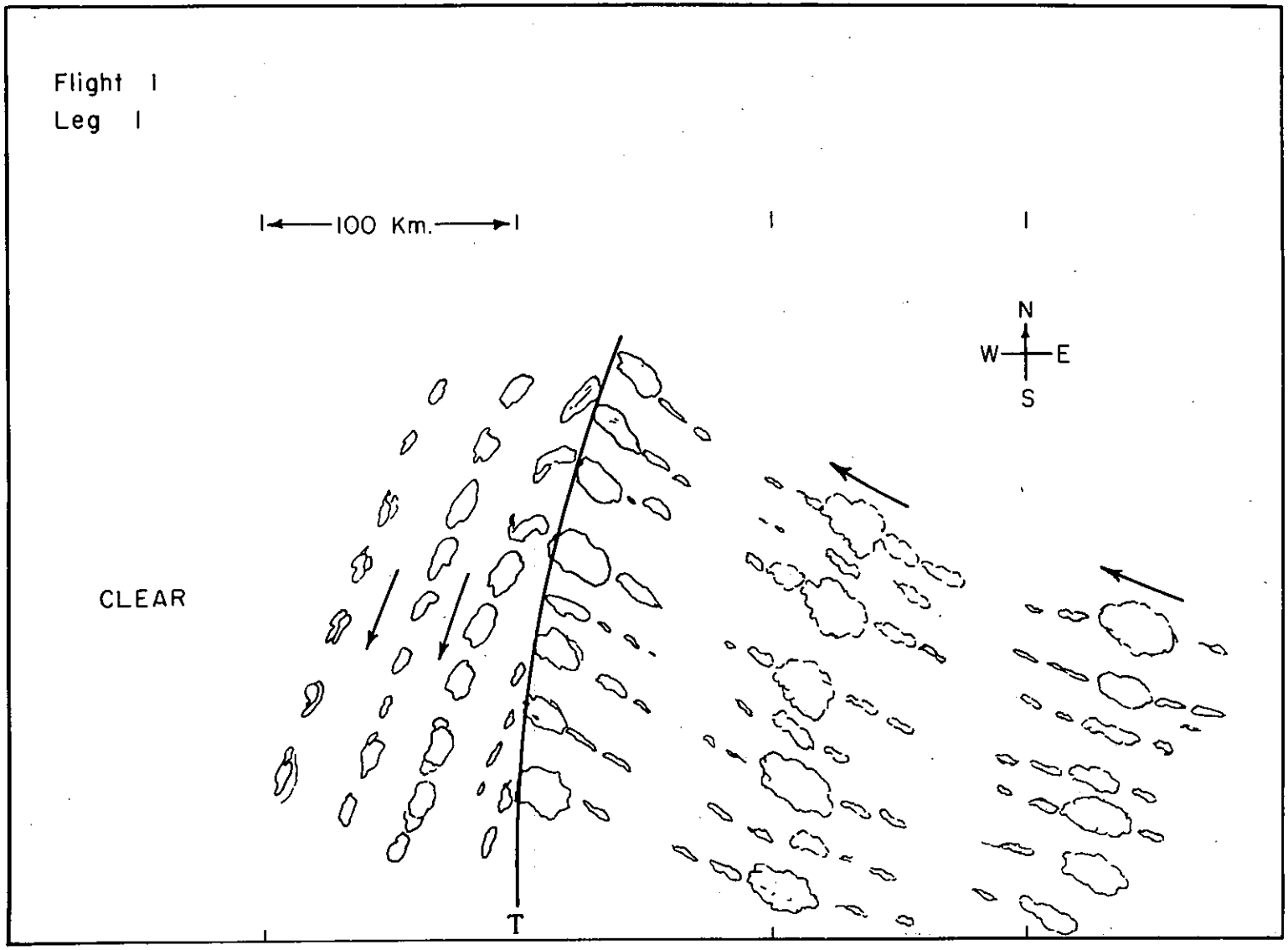

Figure 73. Schematic cloud map for westward-travelling tropical wave in Marshall Islands area.

superposed cross-wind organization parallel to the shear. At first the rows are about 4 km apart, but they gradually widen by suppression of all but every fourth row, to a spacing of about 16 km. West of the wave trough we found three, and only three, rows of clouds up to about 12,000 oriented with the shear and not the wind.

Another fascinating cloud configuration is shown in figure 74. It may have been the convective area of a very weak easterly wave trough that was barely detectable on the synoptic charts. Its striking feature is four, and only four, rows of cumulonimbus towers lined up at a high angle to the low-level wind. The cumulonimbus tops were at about 35,000 ft. The rows are about 40 n mi apart, which was the distance that was almost always characteristic of the cross-wind mode. Now we note two other cloud orientations on this map. The first is the lines of very small cumuli, which exhibit the parallel mode and are lined up with the low-level wind. Then the cumulonimbus anvils are all extended in still another direction. Their orientation happens to be parallel to the shear vector between the low-level wind and that at the very high levels, namely 30-40,000 ft.

What we have learned about cloud orientation is summarized in figure 75. In each of these cases, the small cumuli are exhibiting the parallel mode, although we should recall that there are cases of small cumuli exhibiting the cross-wind mode. The cumulonimbus towers are lining up in the cross-wind mode, i.e., along the shear vector between the low level wind

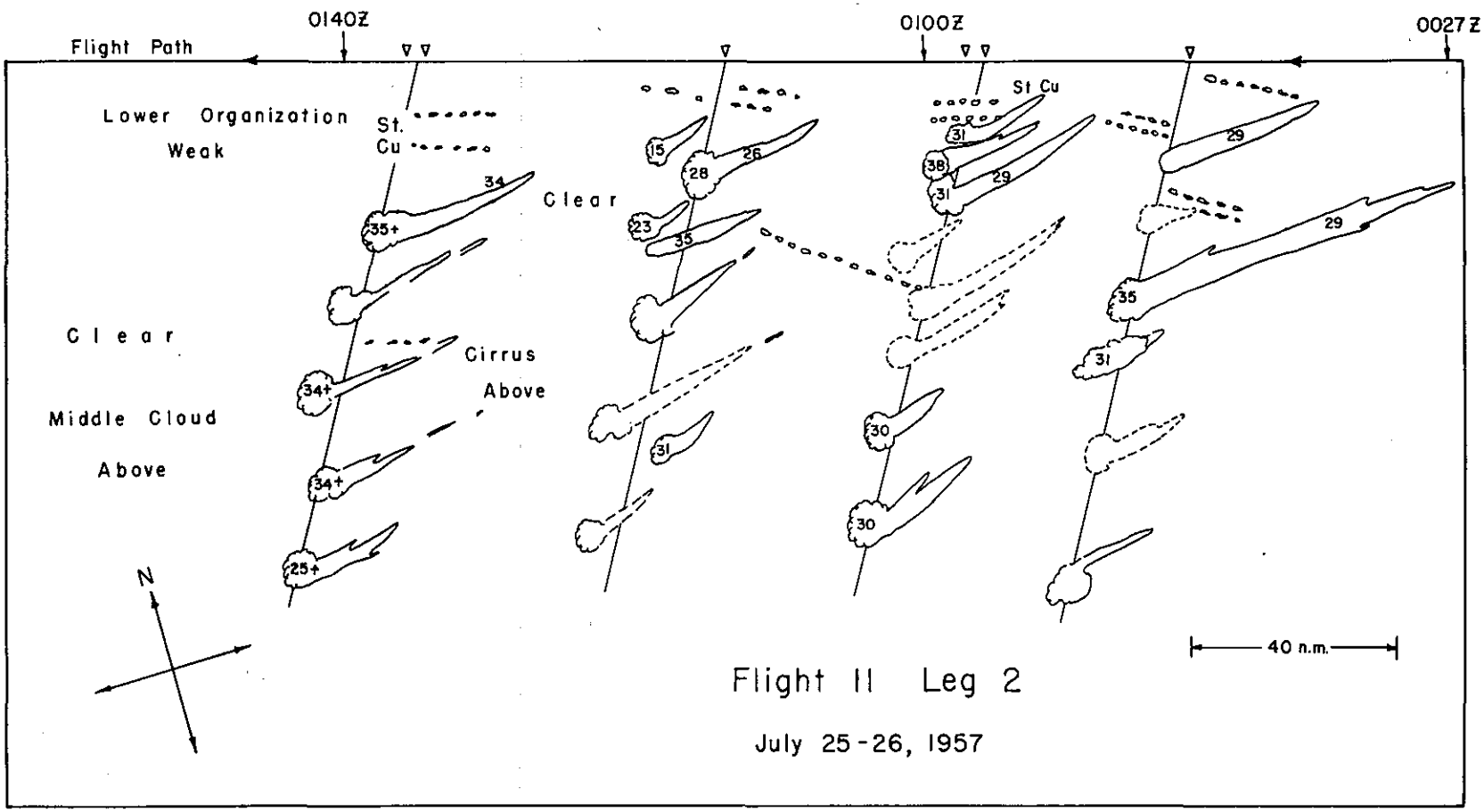

Figure 74. Map of an interesting meso-scale cloud pattern constructed from aerial photographs.

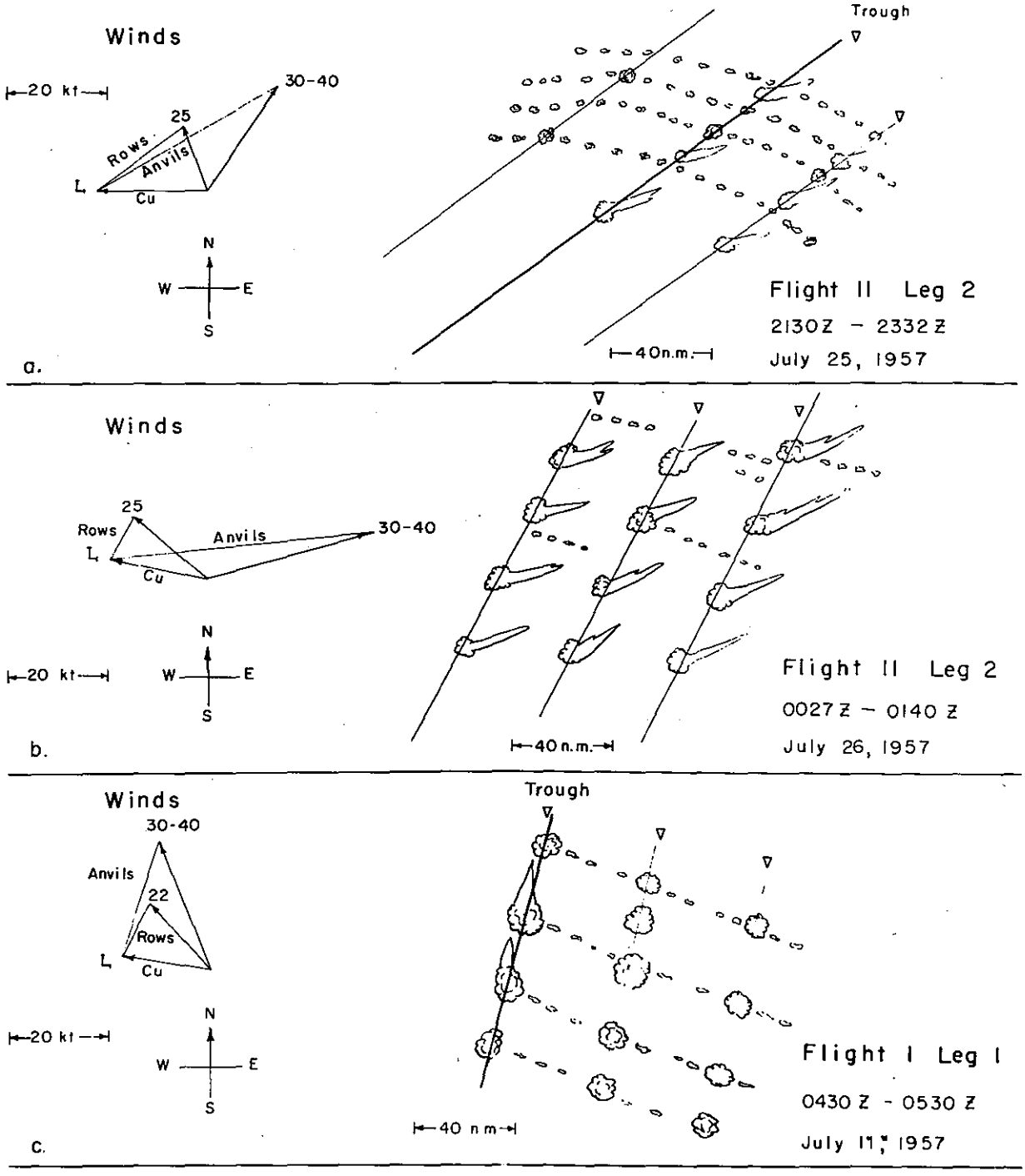

Figure 75. Schematic summary of factors controlling cloud patterning.

and the wind in the mid-troposphere, namely at 20-25,000 ft. The anvils are exhibiting still a third orientation, being lined up along the shear vector between the low-level wind and the wind at anvil level, namely 30-40,000 ft.

We have learned what kinds of organization modes cumulus clouds exhibit, and how these modes are related to the shear in the flow field. We have not learned what determines the onset or the relative intensities of these modes. Nor have we learned how to predict the scales of the rows or cells when they are present. The very few theoretical models that have been put forward to do this have mainly failed when their predictions are compared with observations.

No discussion of cloud patterns would be complete without showing the patterns that are induced by heated flat land masses that are surrounded by water.

Let us first look at the patterns induced by a large land mass, namely the Florida peninsula which is about 140 miles wide and 380 miles long. This picture (fig. 76) was taken in the late forenoon of a sunny summer day by the Gemini 5 astronauts, looking southward along the east coast of the peninsula. We note that the typical clear ring offshore associated with the subsidence compensating for the ascent over the heated land mass. Isolated thunderstorms near the horizon tower in the vicinity of Cuba. Curvature in the cloud lines is evident near Cape Kennedy where development is reaching cumulonimbus stage. The lines across central Florida show the transition in

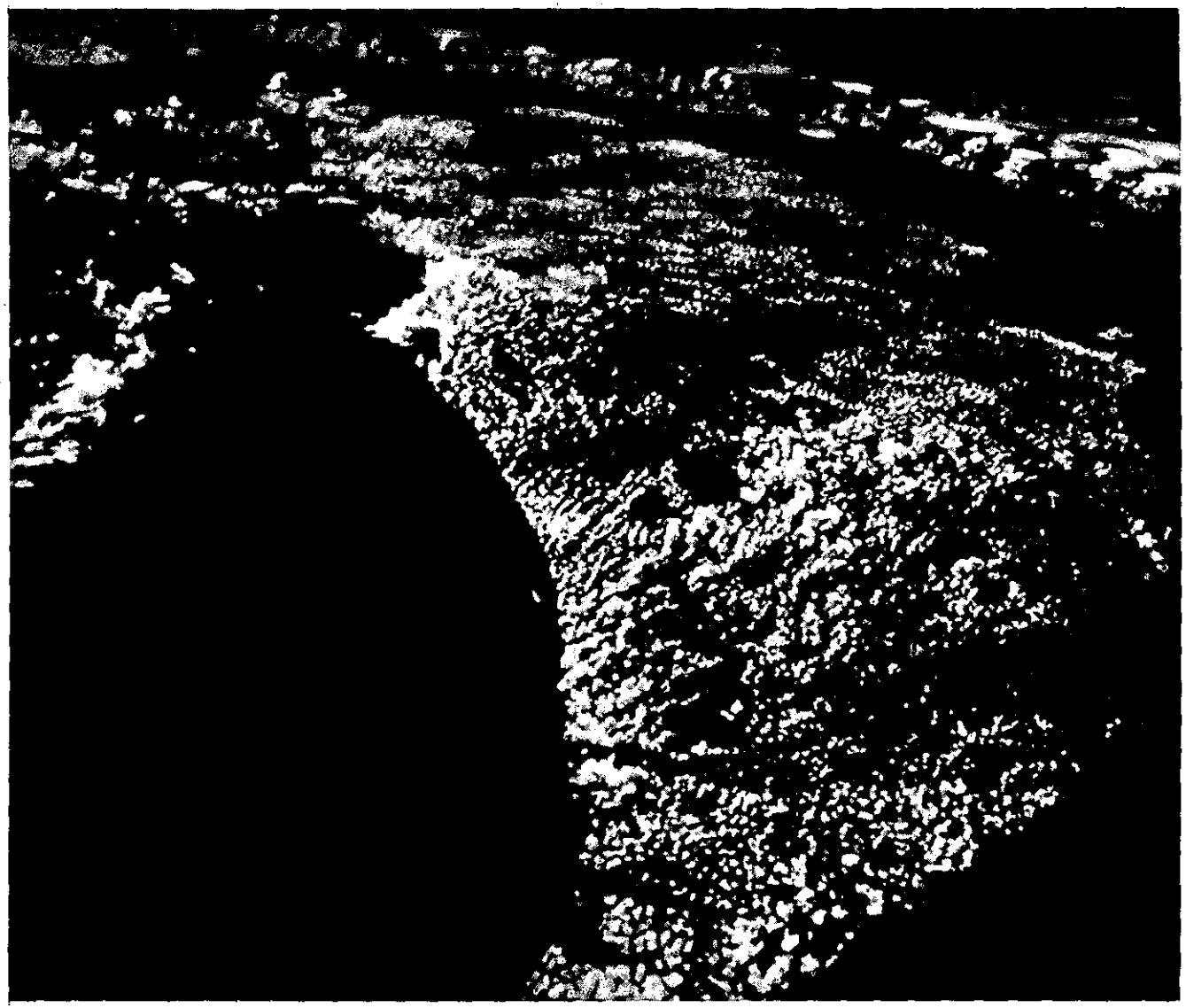

Figure 76. Cloud patterns over and near Florida peninsula. Photograph by Gemini 5 astronauts.

the wind flow from easterly on the Atlantic to southeasterly on the Gulf Coast. The complex flow pattern is typical for a large peninsula where sea breezes along both coast lines can influence major mesoscale circulations. The following picture (fig. 77) shows the peninsula the next day at 2:26 in the afternoon, local time, looking north. We see more advanced convective development, particularly over the Keys and in a long line beginning at Jacksonville in the northeast and reaching down to Cape Sable in the southwestern portion of the peninsula. Descriptive cloud population studies have been made over this peninsula and attemps to theorize and model them numerically are now making encouraging progress at EML.

Finally we go from a large heated land mass to a small heated land mass and look at some typical cloud patterns induced by the fairly flat tropical island of Barbados. Barbados is a triangle 15 by 20 miles in dimension. The cloud maps were constructed schematically from photographs and visual observations made on a series of light plane flights. The first picture (fig. 78) shows starting conditions for the island pattern in the case of a strong trade wind. Normally, during the night and up to as late as about 8 o'clock in the morning, the island has no noticeable effect on cloud patterns. These begin to organize around 9-10 am with the concomitant development of the clear ring offshore. Figure 79 shows the fully developed island pattern shortly after midday, with the very long "main street" characteristic of about half the fair days studied. The shear is from the north so that the wide street reminds us of the Pacific oceanic cases where the shear and the wind were at

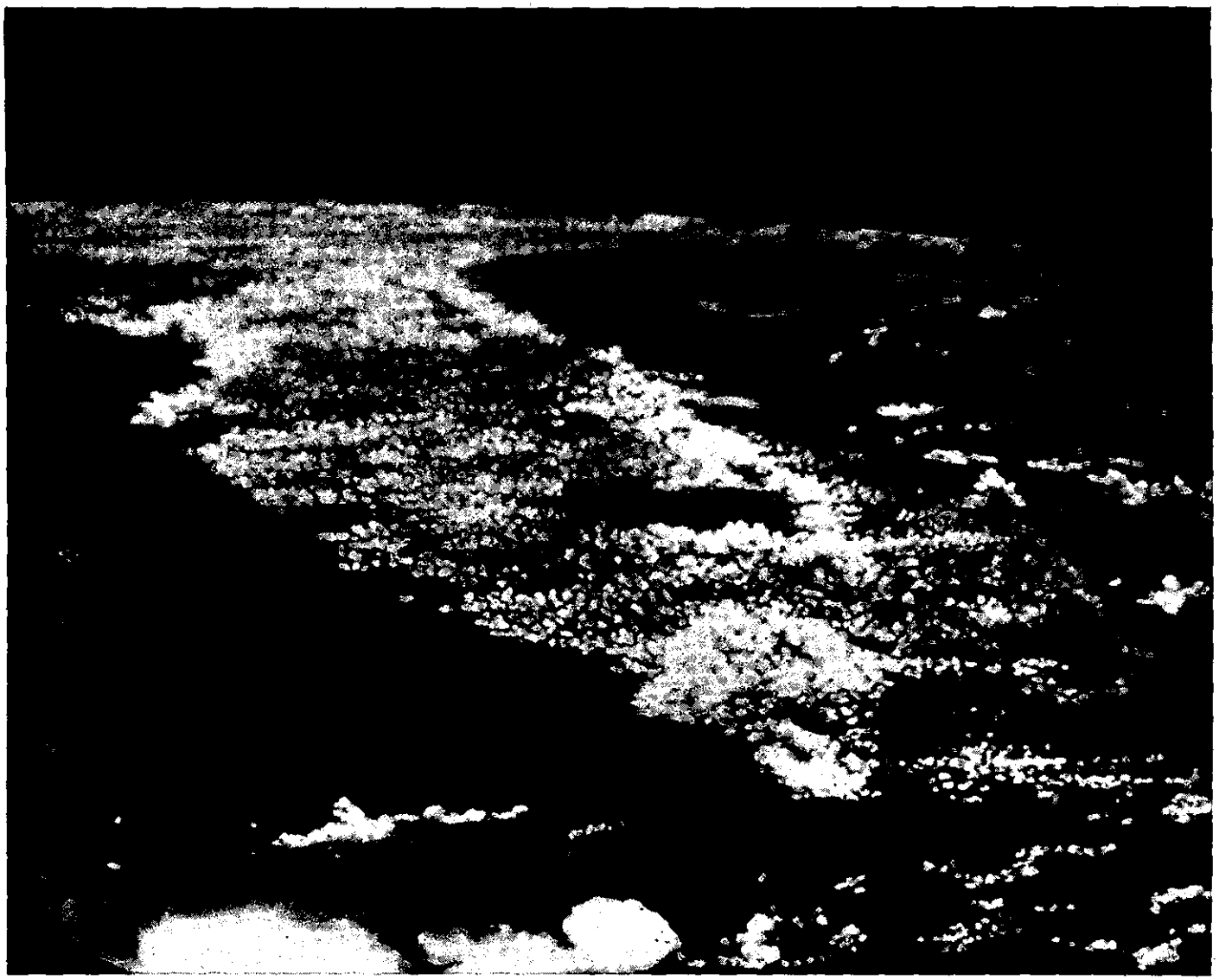

Figure 77. Another photograph of cloud patterns over and near Florida peninsula by Gemini 5 astronauts, day following photograph in figure 76.

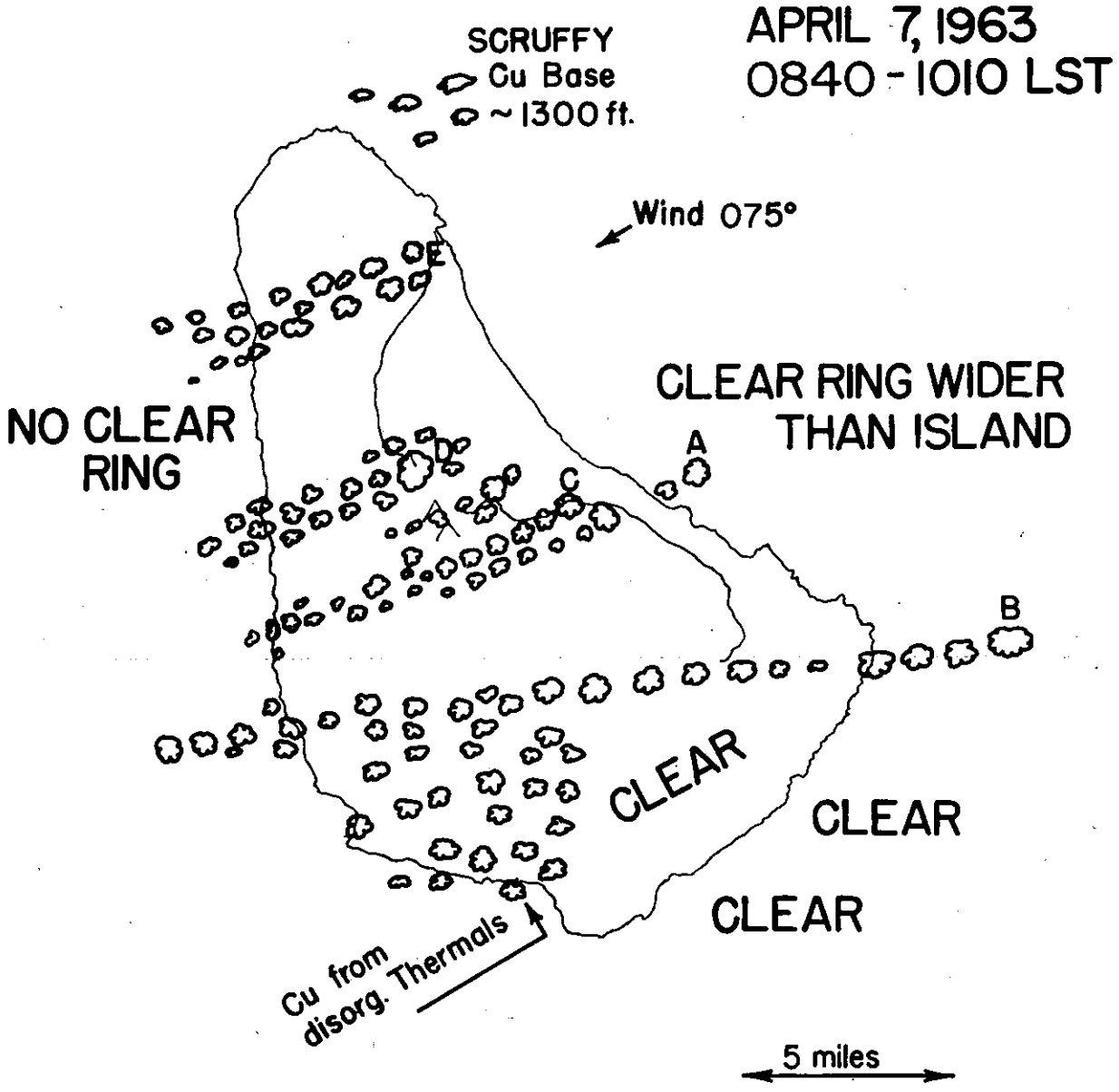

Figure 78. Schematic map of cloud patterns over Barbados on typical fair day in dry season. Beginning of island effect in the morning.

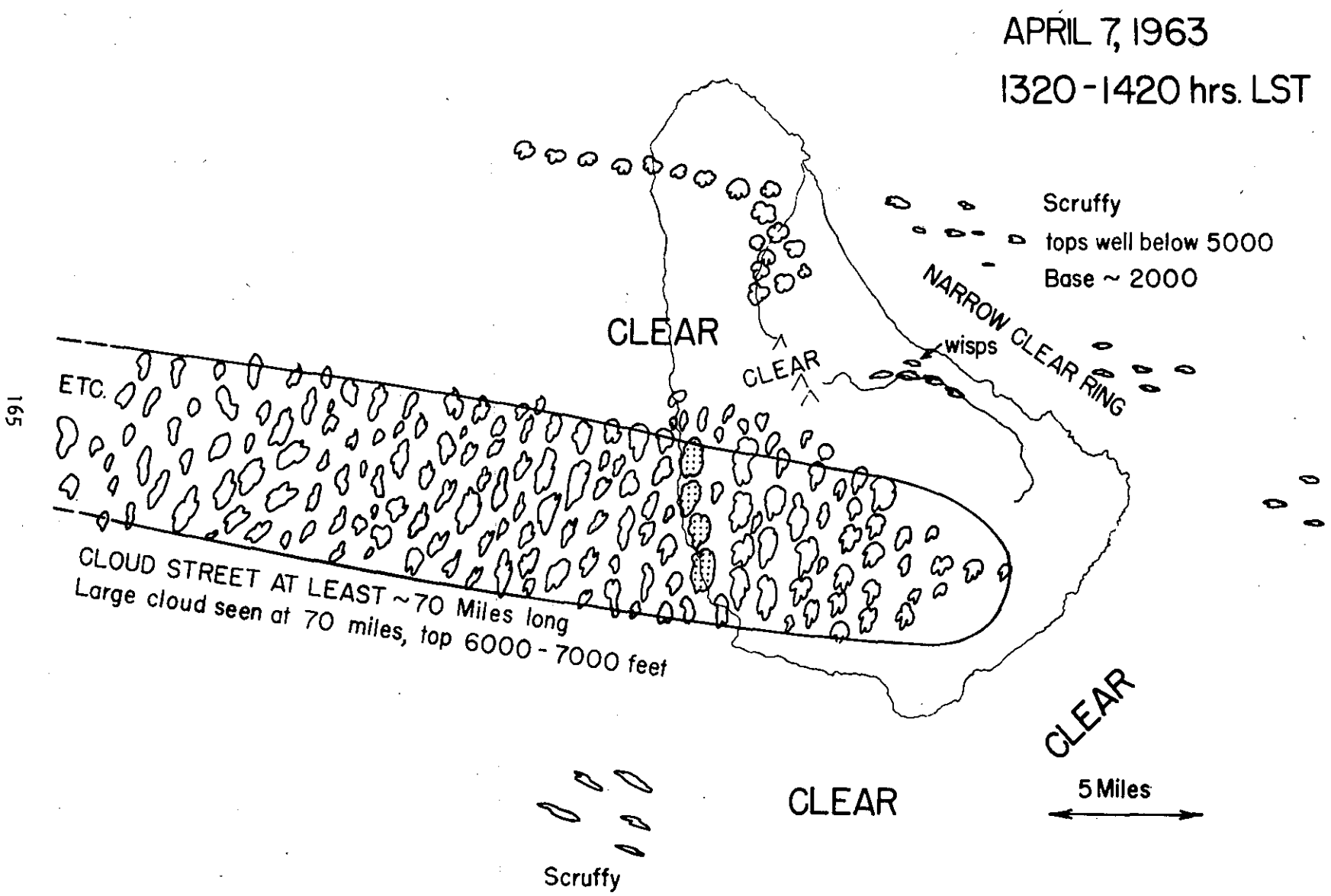

Figure 79. Schematic map of cloud patterns over Barbados on typical fair day in dry season. Midday pattern.

right angles. The last flight on this day was made between 5 and 6 pm, at which time the island and surrounding waters were completely clear of cloud.

In figure 80 we see the rather late starting conditions typical of a weak trade-wind day. The winds are veered around to southeast, as is the cloud street which is truncated and has a strange branch in it. It remained truncated all day, which may have been due to the light wind. Figure 81 shows the ending or near sunset conditions for the same day. What happens now is typical of the ending conditions for many cloud streets from many islands. The whole street reaches its greatest vertical development as sunset approaches, particularly in the clouds just at the lee shore, which often precipitate. Over the island itself, however, the clouds die out as the ground temperature lowers. Just after sunset, the whole cloud street detaches itself from the lee shore and moves off downwind, often still precipitating. There are many papers in the literature on the heated island and its cloud patterns; some are included in the references. Reference 56 documents observationally the cloud patterns over a mountainous island. Theoretical studies of the airflow over a heated island are cited in references 57-59. Since these are linear and two-dimensional, they will only have partial relevance to the Barbados cloud patterns shown, where the cloud street is crucially dependent on the effect of the third dimension.

It is appropriate to conclude the discussion of cloud studies with the subject of cloud groups and patterns which is a fascinating and wide

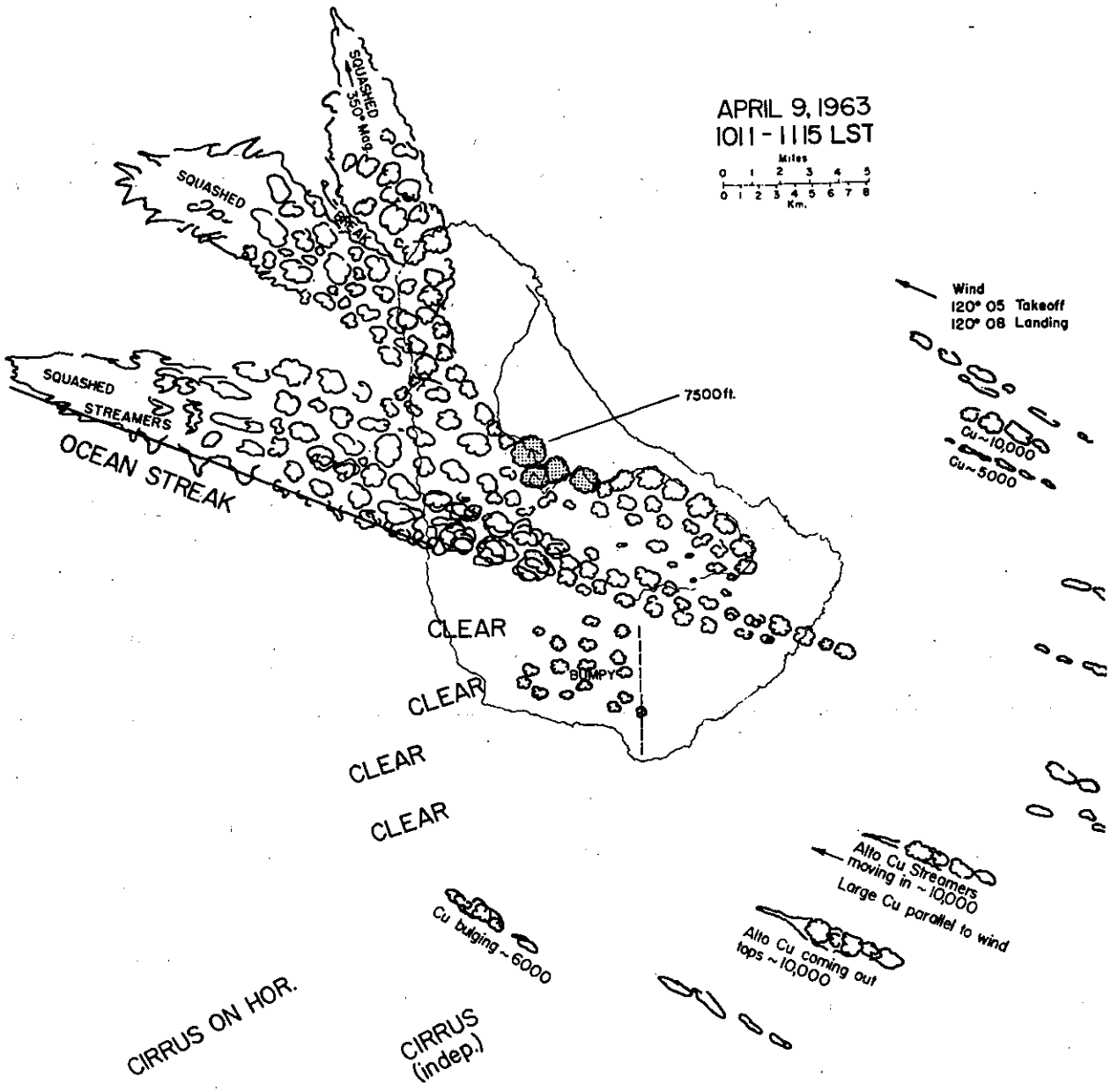

Figure 80. Schematic map of cloud patterns over Barbados on typical weak trade-wind day. Note late start of island effect.

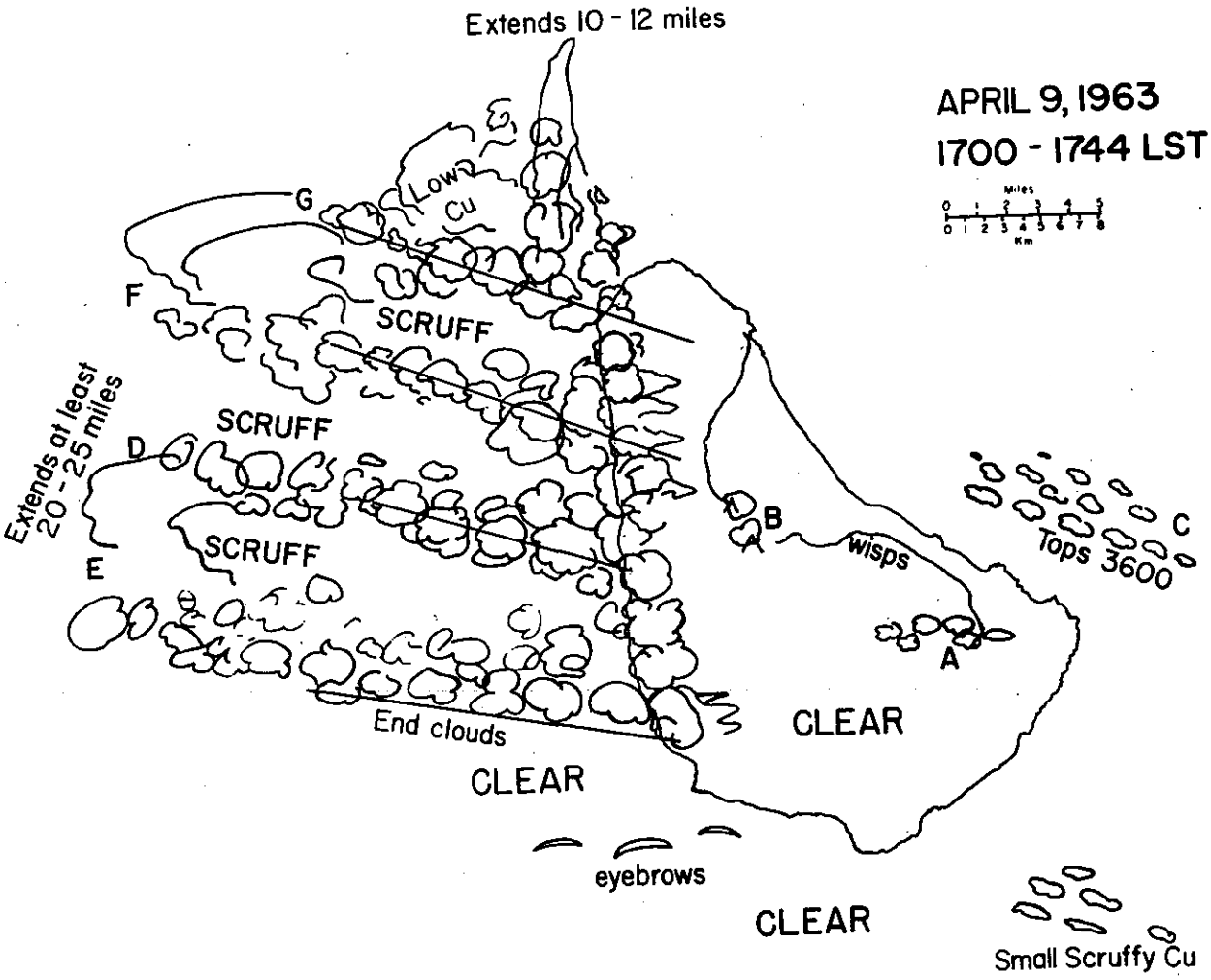

Figure 81. Schematic map of cloud patterns over Barbados on same day as figure 80, near sunset conditions.

open frontier. As one can see from the material presented herein, some quantitative description has been done, but predictive theories and numerical models on cloud groupings are just beginning. Since it is not single clouds, but many, that have joined or banded themselves together to form severe storms or influence large-scale flows, the interaction of clouds is one of the most important problems in meteorology.

6. ACKNOWLEDGMENTS

This review is dedicated to the author's colleagues in tropical meteorology and to their students, in particular to Michael Garstang, William Gray and Edward Zipser.

I continue to be grateful to my long-time colleague, Professor Herbert Riehl, who inspired and participated in virtually all contributions to tropical meteorology since the mid-1940's including my own.

The nature of this presentation precluded explicit referencing of the work of numerous researchers, whose valuable studies are nonetheless fully recognized and appreciated.

The completion of this work was instigated by Mr. Robert Powell of EML, whose fine work in preparing the figures is much appreciated.

6. REFERENCES

General references on global heat budgets:

1. Malkus, J.S. (1962), Large-scale interactions. Chap. 4, The Sea: Ideas and Observations on Progress in the Study of the Seas. Interscience Publishers, New York and London, pp. 88-294.

2. Palmén, E. and C.W. Newton (1969), Atmospheric circulation systems. Academic Press, New York and London, 1-64.

3. Budyko, M.I. (1956), The heat balance of the earth's surface. Gidrometeorologicheskoe izdatel'stro, Leningrad, 255 pp. (Translated by Nina A. Stepanova; translation distributed by the U.S. Weather Bureau, Washington, D.C., 1958.)

4. Budyko, M.I., N.A. Epinova, L.I. Zubenok and L.A. Strokina (1962), The heat balance of the earth's surface. Ak. nauk. U.S.S.R., Izv. Bureau, Washington, D.C., 1958.)

5. Sellers, W.D. (1965), Physical climatology, The University of Chicago Press, Chicago and London. Especially Chap. 8.

Satellite papers bearing on energy budget computations:

6. Rasool, S.I. and C. Prabhakara (1966), Heat budget of the southern hemisphere, Problems of Atmospheric Circulation, Spartan Books, New York. 76-92.

7. Fritz, S., P. Krishna Rao and M. Weinstein (1964), Satellite measurements of reflected solar energy and the energy received at the ground, J. Atmos. Sci. 21, 141-151.

8. Hanson, K.J., T.H. Vander Haar and V.E. Suomi (1967), Reflection of sunlight to space and absorption by the earth and atmosphere over the United States during spring 1962, Mon. Wea. Rev. 95, 354-362.

9. Winston, J.W. (1969), Global distribution of cloudiness and radiation as measured from weather satellites, Chap. 6, Climate of the free atmosphere, World Survey of Climatology, v. 4, Elsevier Publishing Co., Amsterdam.

10. Arking, A. (1964), Latitudinal distribution of cloud cover from TIROS III photographs, Science 143, 569-572.

Classical or important works on heat budget components;

11. Jacobs, W.C. (1949), The energy acquired by the atmosphere over the oceans through condensation and through heating from the sea surface, J. Met. 6, 266-272.

12. Jacobs, W.C. (1951), Large-scale aspects of energy transformations over the oceans, Compendium of Meteorology, Amer. Met. Soc., 1050-1070.

13. London, J. (1957), A study of the atmospheric heat balance, N.Y. U., Dept. Met. Oceanog. Final Rep., Project 131, Contract No. AF19(122)-165, 99 pp.

14. Houghton, H. (1954), On the annual heat balance of the northern hemisphere, J. Met. 11, 1-9.

15. Lumb, F.E. (1964), The influence of cloud on hourly amounts of total solar radiation at the sea surface, Quart. J. Roy. Met. Soc. 90, 43-56.

16. Colón, J. (1960), On the heat balance of the troposphere and water body of the Caribbean Sea. National Hurricane Research Project, Report No. 41., U.S. Dept. of Commerce, Washington, D.C., 65 pp.

17. Starr, V.P., J.P. Peixoto and A.R. Crisi (1965), Hemispheric water balance for the IGY, Tellus 17, 463-472.

References on heat transports by ocean currents:

18. Bryan, Kirk (1962), Measurements of meridional heat transport by ocean current, J. Geophys. Res. 67, 3403-3414.

19. Emig, M. (1967), Heat transport by ocean currents, J. Geophys. Res.72, 2519-2529.

20. Albrecht, F. (1960), Jahreskarten des Wärme- und Wasserhaushaltes der Ozeane, Ber. deut. Wetterdienstes 66, Bd. 9, 19 pp.

References on Synoptic-Scale Variation in Sea-Air Exchange

21. Malkus, J.S. and H. Riehl (1960), On the dynamics and energy transformations in steady state hurricanes, Tellus 12, 1-20.

22. Simpson, J. (1969), On some aspects of sea-air interaction in middle latitudes, Deep Sea Research, Supplement to Vol. 16, 233-261.

Also see pages 217-231 in Malkus, 1962.

Entrainment theory and observations; effects of wind shear:

23. Stommel, H. (1947), Entrainment of air into a cumulus cloud, J. Meteor. 4, 91-94.

24. Malkus, J.S. (1954), Some results of a trade cumulus cloud investigation, J. Meteor. 11, 220-237.

25. Malkus, J.S. (1949), Effects of wind shear on some aspects of convection, Trans. Amer. Geophys. Un. 30, 19-25.

26. Malkus, J.S. (1952), The slopes of cumulus clouds in relation to external wind shear, Quart. J. Roy. Met. Soc. 78, 530-542.

Laboratory experiments on convection elements:

27. Scorer, R.S. and C. Ronne (1956), Experiments with convection bubbles, Weather 11, 151-154.

28. Woodward, E.B. (1959), The motion in and around isolated thermals, Quart. J. Roy. Met. Soc. 85, 144-151.

29. Saunders, P.M. (1962), Penetrative convection in stably stratified fluids, Tellus 14, 177-194.

30. Turner, J.S. (1962), The 'starting plume' in neutral surroundings, J. Fluid Mech. 13, 356-368.

Numerical cumulus models:

31. Malkus, J.S. and G. Witt (1959), The evolution of a convective element: A numerical calculation, The Atmosphere and the Sea in Motion, Rockefeller Institution Press, New York, 425-439.

32. Malkus, J.S., R.H. Simpson, D.A. Andrews and M.A. Eaton (1965), Experimental cumulus dynamics, Reviews of Geophysics 3, 387-431.

33. Murray, F.W. and C.E. Anderson (1965), Numerical simulation of the evolution of cumulus towers, Douglas report SM-49230, Douglas Missile and Space Systems Division, Santa Monica, Calif.; 97 pp.

34. Murray F.W. (1970), Numerical models of a tropical cumulus cloud with bilateral and axial symmetry, Mon. Wea. Rev. 98, 14-28.

35. Lilly D.K. (1962), On the numerical simulation of buoyant convection, Tellus 14, 148-172.

36. Simpson J. and V. Wiggert (1969), Models of precipitating cumulus towers, Mon. Wea. Rev. 97, 471-489.

37. Shafrir, U., S. Kaniel and B. Shkoller (1970), Three-dimensional, time-dependent numerical experiments with dry and moist, shallow and deep convection models, unpublished manuscript on file at Goddard Inst. for Space Studies, New York, 61 pp.

Structure of the trade-wind boundary layer:

38. Malkus, J.S. (1962), Large-scale interactions, Chap. 4. The Sea: Ideas and Observations on Progress in the Study of the Seas, Interscience Publishers, New York and London, 88-294.

39. Bunker, A.F., B. Haurwitz, J.S. Malkus and H. Stommel (1949), Vertical distribution of temperature and humidity over the Caribbean Sea, Papers Phys. Oceanog. Meteor., Mass. Inst. of Tech. and Woods Hole Oceanog. Inst. 11, 82 pp.

40. Malkus, J.S. (1958), On the structure of the trade-wind moist layer, Papers Phys. Oceanog. Meteor., Mass. Inst. of Tech. and Woods Hole Oceanog. Inst. 13, 47 pp.

Energetics and dynamics of Pacific trade-winds:

41. Riehl, H., T.C. Yeh, J.S. Malkus and N.E. LaSeur (1951), The northeast trade of the Pacific Ocean, Quart. J. Roy. Meteor. Soc. 77, 598-626.

42. Malkus, J.S. (1956), On the maintenance of the trade winds, Tellus 8, 335-350.

43. Pike, A.C. (1968), A numerical study of tropical atmospheric circulations, Report of Contract No. F19628-68-C-0144, Inst. of Atmospheric Science, Univ. of Miami. 125 pp.

Energetics and mechanisms of the equatorial trough zone:

44. Riehl, H. and J.S. Malkus, (1958), On the heat balance in the equatorial trough zone, Geophysica (Helsinki), 6(3-4), 503-538.

See also Malkus, 1962, pp. 164-177 and Pike, 1968.

Cloud groups and patterns:

45. Malkus, J.S. and H. Riehl (1964), Cloud structure and distributions over the tropical Pacific Ocean, University of California Press, Berkely and Los Angeles, 229 pp.

46. Bunker, A.F. and M. Chaffee (1969), Tropical Indian Ocean Clouds, International Indian Ocean Expedition, Meteor. Mono. No. 4, East-West Center Press, Honolulu, 193 pp.

47. Malkus, J.S. and H. Riehl (1964), Cloud structure and distributions over the tropical Pacific Ocean, Tellus 16, 275-287.

48. Krueger, A.F. and S. Fritz (1961), Cellular cloud patterns revealed by Tiros i, Tellus 13, 1-7.

49. Kuettner, J. (1959), The band structure of the atmosphere, Tellus 11, 267-294.

50. Avsec, D. (1939), Thermoconvective eddies in air, Application to Meteorology, Scientific and Tech. Pub. of Air Ministry Works of Inst. of Fluid Mech. of Fac. of Sci., Paris, No. 155. Published (in French) at Ed. Blondel la Rougery, 7, Rue St. Lazare, Paris.

51. Hubert, L.F. (1966), Mesoscale cellular convection, Meteorological Satellite Laboratory, Report No. 37, ESSA, U.S. Dept. Com., Washington, D.C., 68 pp. (Has an excellent bibliography).

52. Simpson, R.H., N. Frank, D. Shideler and H.M. Johnson (1968), Atlantic tropical disturbances, 1967. Mon. Wea. Rev. 96, 251-259.

53. Baum, Robert A. (1970), The Eastern Pacific hurricane season of 1969, Mon. Wea. Rev. 98, 280-292.

54. Malkus, J.S., C. Ronne and M. Chaffee (1961), Cloud patterns in hurricane Daisy, 1958, Tellus 13, 8-30.

55. Malkus, W.V.R. (1954), Discrete transitions in turbulent convection, Proc. Roy. Soc., A, 225, 185-195.

56. Malkus, J.S. (1955), The effects of a large island upon the trade-wind air stream, Quart. J. Roy. Met. Soc. 81, 538-550.

57. Malkus, J.S. and M.E. Stern (1953), The flow of a stable atmosphere over a heated island, Part II, J. Meteor. 10, 30-41.

58. Stern, M.E. and J.S. Malkus (1953), The flow of a stable atmosphere over a heated island, PartII, J. Meteor. 10, 105-120.

59. Smith, R.C. (1955), Theory of air flow over a heated land mass, Quart. J. Roy. Met. Soc. 81, 382-395.

☆ U.S. GOVERNMENT PRINTING OFFICE: 1974-784-572/1236 REGION NO. 8